Mechanistic basis of gating in potassium two-pore domain ion channels

By

Robert Alexander Rietmeijer

A dissertation submitted in partial satisfaction of the

requirements for the degree of

Doctor of Philosophy

in

Biophysics

in the

Graduate Division

of the

University of California, Berkeley

Committee members:

Professor Stephen Brohawn, Chair
Professor Ehud Isacoff
Professor Diana Bautista
Professor Eunyong Park

Spring 2021

Mechanistic basis of gating in potassium two-pore domain ion channels

By

Robert Alexander Rietmeijer

Abstract

Mechanistic basis of gating in potassium two-pore domain ion channels

By Robert Alexander Rietmeijer

Doctor of Philosophy in Biophysics

University of California, Berkeley

Potassium two-pore domain (K2P) family ion channels are increasingly appreciated as important electrogenic sensors that are used by diverse cell types including neurons, cardiomyocytes, and epithelial cells. The activity of these channels can be activated up to one-hundred fold by diverse physical and chemical stimuli including pH, intracellular calcium, temperature, phospholipids and fatty acids, volatile anesthetics, and membrane tension. In addition to this “stimulus gated” activity, channels in this family also have a basal “leak gated” activity that drives the cellular resting membrane close to the potassium ion reversal potential in the absence of their respective stimuli. While the structural basis of closed states and certain “stimulus gated” open states have been previously determined, the structural basis of a “leak gated” open state in K2P channels is unknown. Here, we show the physical basis for basal “leak gated” activity of the mechanosensitive K2P family ion channel TRAAK, and propose a gating model that includes both “leak gated” and “stimulus gated” openings. Next, we identify the structural basis of intracellular and extracellular alkaline pH “stimulus gated” activation in the acid-sensitive K2P family ion channel TASK2. We observe structural similarities between the “leak gated” structure of TRAAK and other K2P channel structures, including TASK2. This observation supports a general mechanism for “leak gated” activity in K2P family ion channels.

Dedication

To my parents, Franciscus and Fleur.
Thank you for your encouragement and support, always.
“*Weten door meten*”

Acknowledgements

While I get to put my name on it, many people contributed to this work directly, indirectly, scientifically, and emotionally. Thanks to my parents for their unwavering sacrifices to allow me to reach this point. I wish my studies could have been closer to home.

My scientific journey may not have led me to a Biophysics PhD at Berkeley if my undergraduate research advisor, Professor Dmitri Ermolenko, hadn't given me a chance in his lab. I'll always be grateful to him for believing in me, and for the excellent advice to pursue a PhD in California.

I've been lucky to find wonderful colleagues and mentors at Berkeley. A special to thanks to my classmate, previous housemate, and friend Raoul Martin for the suggestion to do a lab rotation in Steve Brohawn's lab – that ended up being the most consequential advice I've received at Berkeley. I could not have found a better lab to do a PhD in. Steve provided a constant stream of feedback and support through several ongoing projects that I pursued on the way to the two stories described here. It's been a privilege to work with and learn from such an indomitable scientific mind. I hope to find more people like Steve, wherever I go.

Data from X-ray crystallography and cryo electron microscopy are foundational to the stories in this work. These methods are really hard, and I benefitted tremendously from the assistance and advice of Dr. George Meigs at the ALS, Dr. Igor Kourinov at the APS, and Dr. Jonathan Remis at the Berkeley cryo electron microscopy facility, CalCryo. Structural biology is a team sport.

As the first graduate student in the lab, I've watched the lab grow and helped cultivate it as best I could. It's becoming an ever better place. Ben, Baobin, and David epitomize what it means to be a postdoc to me: supportive, technically savvy, and interested in their and other people's science at all hours of the day. They don't have an "off" button, and it's amazing. Ben and Baobin: it was wonderful working on papers with each of you, we make a great team. Thanks also to my fellow graduate students in the lab, Chris, Toby, Michelle, Kim, and Kyle: it's been a blast working many extremely late nights purifying protein with each of you. I'm excited to see what paths each of you will choose after graduation.

As I wrap up my PhD I also want to thank Ian Tayler, who is now in his second year in the Molecular, Cellular, and Developmental Biology PhD program at UC Santa Cruz. Thank you for teaching me how to be a good undergraduate mentor. I'm glad I could pay it forward by giving you the same advice Dmitri gave me: California is a beautiful place to pursue a PhD!

Lastly, I want to thank my biggest and most immediate support system, my fiancé Anna. I don't know what could possibly be sexy about a man who comes home 5 hours late because he ran into trouble purifying a measly milligram of protein. I'm lucky to be marrying you.

Tables of Contents

2.1 Introduction

2.2 Results

2.3 Materials and Methods

2.4 Tables

Chapter 1 K2P channel physiology and gating models: sensors and gates

This chapter provides background on the role of K2P channels in the human body and the current biophysical understanding of how these channels gate open and closed in response to stimuli.

1.1 Molecular physiology of K2P family ion channels

Potassium ion channels in the K2P (Potassium two-pore domain) family sense diverse physical and chemical stimuli. These stimuli include pH, intracellular calcium, temperature, phospholipids and fatty acids, volatile anesthetics, and membrane tension [1,2]. Each of the 15 members of the K2P channel family is sensitive to more than one stimulus, such that K2P channels contribute polymodal sensitivities to the cells in which they are expressed. The 15 K2P channels are further taxonomized into 6 subfamilies by amino acid sequence homology, which mirrors their most distinguishing sensitivities (Fig. 1).

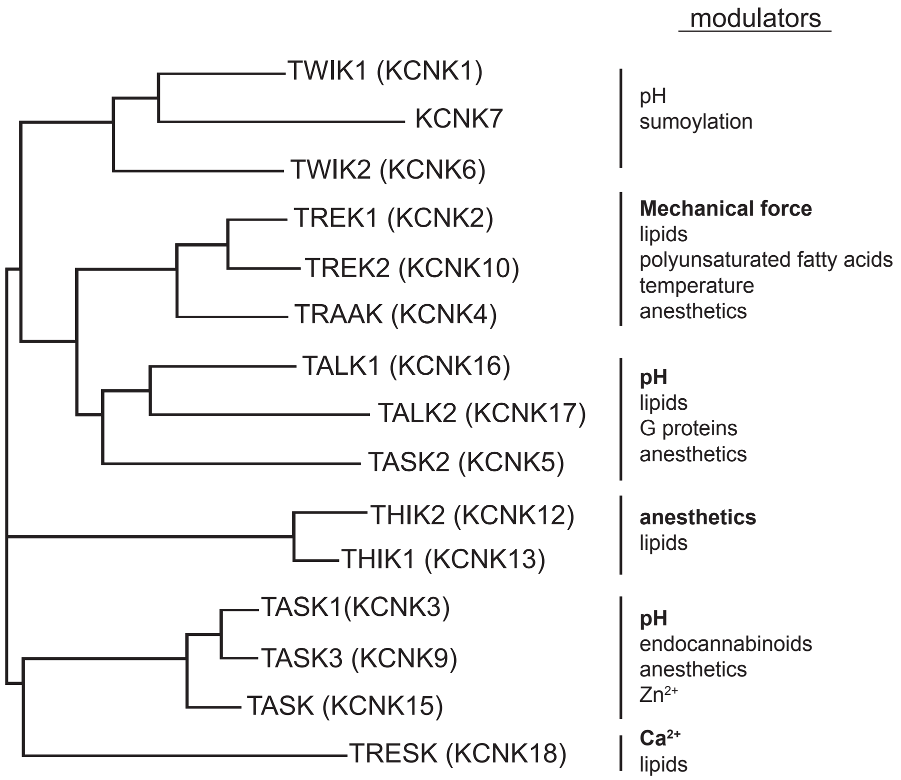

Figure 1 K2P family ion channel phylogenetic tree.
The tree was calculated from an amino acid sequence alignment of the pore domain of the fifteen human K2P sequences as in *ref 24*. Major branches of the tree group the channels into six subfamilies. These subfamilies mirror the primary sensitivities of each subfamily, indicated in bold font.

K2P channel gating in response to physical and chemical stimuli integrates this information into the electrical state of the cell. K2P channels are usually highly potassium-selective such that their activity drives the cellular resting membrane potential towards the potassium ion reversal potential [3]. K2P channels expressed in neurons of the peripheral and central nervous system contribute a hyperpolarizing current when activated. Mechanosensitive K2P channels TRAAK and TREK1 shape the action potential waveform in the nodes of Ranvier, axonal structures that enable action potential propagation over long distances by saltatory conduction [4,5]. The alkaline-sensitive K2P channel TASK2 is expressed in neurons of the retrotrapezoid nucleus in the brainstem contributes to the central chemosensory reflex [6–8]. TASK2 channels in kidney proximal tubules provide electrogenic feedback that modulates the rate of salt reuptake [9]. K2P family channels are expressed throughout the body including the peripheral and central nervous systems, heart, eyes, kidneys, and pancreas [1]. Dysregulation of K2P channels has been implicated in pathologies including migraine, depression, pulmonary hypertension, atrial fibrillation, diabetes, Birk-Barel syndrome, congenital central hypoventilation syndrome (CCHS), and FHEIG syndrome [6,10–18]. There is little mechanistic insight as to how mutations in K2P channels affect their gating or how aberrant K2P channel gating results in these pathologies.

1.2 A dearth of specific high affinity K2P channel drugs

There are no approved drugs that selectively target K2P channels. K2P channels are known targets of volatile anesthetics and antidepressants, but these drugs act on multiple targets by incompletely understood mechanisms [19]. Some preliminary pharmacological tools for studying K2P channel gating have been developed from structural and mechanistic studies of K2P gating. An extracellular drug binding pocket may be exploited to develop drugs that are specific to K2P family subtypes [20]. The intracellular cavities of K2P, hERG, and BK channels can also be targeted with micromolar affinity drugs with a defined 'pharmacophore' of shared chemical properties [21]. Two structurally related drugs were recently reported to inhibit TASK subfamily channels with nanomolar affinity, and are undergoing clinical trials [22]. While these developments are promising, most K2P subfamilies cannot be targeted with high-affinity, state-specific pharmacology. The development of specific nanomolar affinity pharmacological tools for K2Ps has lagged for several reasons: i) most K2P channelopathies have been recently discovered, ii) their broad expression in the body may require targeted delivery to avoid side effects iii) their unique structural architecture compared to other potassium ion channel families, and iv) poor mechanistic understanding of the diversity of sensors and gates used by each K2P subfamily. Specific K2P channel activators and inhibitors would be useful tools for studying the function of K2P channels in physiological systems, and for potentially treating the growing list of diseases caused by K2P channelopathies.

1.3 The emerging picture of K2P channel architecture

Crystal structures of the K2P family channels TWIK1 and TRAAK were reported 2012 [23,24]. Since then, crystal structures of TREK1, TREK2, and TASK1 have also been reported [12,20,22]. This work includes the first cryo-EM structures of a K2P channel, TASK2, which was determined at resolution comparable to the crystal structures [25]. The overall architecture of each K2P channel is the same. K2P channels are dimeric and each subunit has two non-identical pore-domains. Each pore domain contains two transmembrane helices, a pore helix, and a selectivity filter motif. The potassium selectivity filter of K2P channels retains the tetrameric architecture of other potassium channel because each subunit contains two pore helices followed by selectivity filter motifs (hence the family name of 'two-pore').

One striking feature of K2P channels is the extracellular cap. The cap extends from the first transmembrane helix and forms another short alpha helix as it loops down towards the membrane. These helices form a domain-swapped dimeric cap via interior facing hydrophobic amino acids that create a complementary hydrophobic surface. In the TWIK, TREK, TALK, and TRESK subfamilies, a conserved cysteine residue forms a disulfide bond, further stabilizing the extracellular cap structure [24]. It is unclear what role, if any, the extracellular cap plays in K2P channel homodimerization or heterodimerization. It is clear that the extracellular cap contributes to the distinct pharmacology of K2P channels by sterically occluding extracellular acting drugs and toxins that target other potassium channels [26–29].

The putative role of the intracellular C-terminus in K2P gating is not well understood. The intracellular C-terminus is not predicted to adopt a stable fold, and has been removed to improve the stability and homogeneity of all K2P channel constructs used for structural studies. Importantly, the constructs used for structural studies recapitulate the stimuli sensing and gating of the full-length channels. K2P channel C-termini may play a role in the trafficking, localization, and regulation of the channels in endogenous tissues, but their function remains unclear [1].

1.4 Gating in K2P family ion channels

Where does gating occur in K2P family ion channels? Obstruction of the ion conduction axis has been observed at three sites in K2P channel structures: the potassium selectivity filter, the intracellular cavity below the filter, and the intracellular cavity mouth (Fig. 2). Functional mutagenesis of these gating sites has been verified by electrophysiological studies.

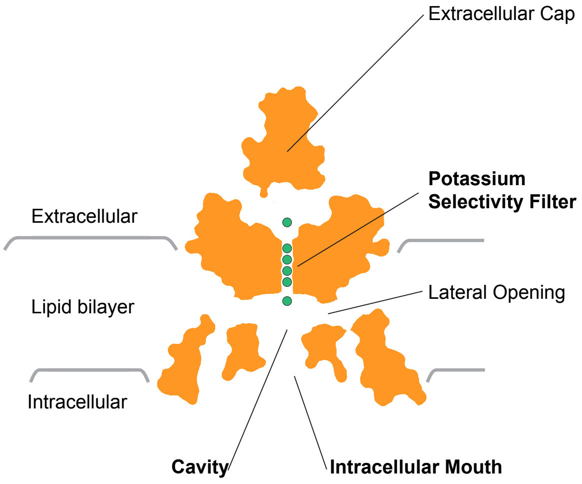

Figure 2 Anatomy and known gating features of K2P family channels.
Generalized cartoon cross-section of a K2P family ion channel annotated with features including the regions where gating occurs: the potassium selectivity filter, cavity, and intracellular mouth. Potassium ions are shown in green, and can be interpreted to flow in either direction.

1.5 The unexplained basal activity of K2P family ion channels

In addition to multifarious stimulus gated currents (Fig 1), a hallmark physiological feature of K2P channels is their 'leak type' current. K2P channels have a low, but non-zero, open probability (P_o) under basal physiological conditions [1,2]. This 'leak type' activity enables K2P channels to contribute to setting the cellular resting membrane potential close to the potassium ion reversal potential. Unstimulated K2P channels in physiological conditions sample flickery openings with low open probabilities (P_o= 0.01 or less) [27,30–38]. Stimulating the channels increases the channel open probability, converting the magnitude and duration of the stimuli into an electrogenic signal to the cell [39–41]. One striking observation from these recordings is that K2P channels have multiple subconductance states. A simple physical explanation of this phenomenon is the existence of multiple distinct conductive channel conformations. However, it's not clear how these basal openings are gated. Determining the structural basis of the basal openings in K2P channels could inform the design of state-specific inhibitors or activators that target the basal, unstimulated open state.

1.6 Basal openings: a conserved gate in a diverse family?

K2P family ion channels have a fascinating breadth of physical and chemical sensitivities. This diversity has made it difficult to extract any generalizable gating mechanisms for the family. In fact, a complete gating mechanism has not been proposed for any K2P channel. Chapter 2 describes and models the physical basis for multiple conductance states in the mechanosensitive K2P channel TRAAK and provides evidence for a gating mechanism that unifies aspects of previously irreconcilable models. Chapter 3 describes the physical basis for pH gating in the alkaline activated K2P channel TASK2 and highlights similarities and differences between the gating of TASK2 and TRAAK. Chapter 4 concludes by exploring the hypothesis that a lateral opening in the closed state of TRAAK, TASK2, and other K2P channel structures is a conserved gate in K2P family channels.

Chapter 2 Physical basis for distinct basal and mechanically-gated activity of the human K+ channel TRAAK

2.1 Introduction

This chapter describes the physical basis of both “leak gated” and “stimulus gated” openings in TRAAK channels. Single channel recordings and crystal structures of gain-of-function point mutants show that the “leak gated” and “stimulus gated” open states pass distinct unitary currents and are structurally distinct. We propose a four state gating model that includes both open states.

2.1.1 TRAAK physiology

TRAAK channels are mechanosensitive K2P channels whose basal activity can be increased ~100 fold by increased membrane tension [42–44]. TRAAK channels are expressed in the nervous systems of jawed vertebrates, and are localized to the nodes of Ranvier in myelinated axons. Nodes of Ranvier are regularly spaced (~1 μm) gaps in the myelin sheath where ion channels localize and pass voltage-gated sodium, voltage-gated potassium, and leak type potassium currents. The regeneration of action potentials at these nodes enables action potential propagation over long distances in a process described as saltatory conduction [45–47]. TRAAK currents generate ~25% of the basal leak-type potassium currents in nodes of Ranvier, contributing to the maintenance of the resting membrane potential and consequent availability of voltage-gated sodium channels needed for high frequency transmission of action potentials [4,5].

Altering TRAAK activity has neurological consequences. TRAAK knock-out mice suffer thermal allodynia and mechanical hyperalgesia, and TRAAK gain of function mutations cause the neurodevelopmental disorder FHEIG (Facial dysmorphism, Hypertrichosis, Epilepsy, Intellectual disability, and Gingival Outgrowth) [18,48]. It is unclear how absent or hyperactive TRAAK currents underlie each phenotype, or whether mechanically activated currents contribute to the high frequency transmission of action potentials.

2.1.2 Model of mechanical activation of TRAAK

A mechanism for TRAAK channel mechanical activation by membrane tension has been developed from structural studies [42,43]. By varying the crystallization conditions, crystal structures of human TRAAK in an open state and a closed state were determined. The principle difference between the open and closed structures is upward movement of the fourth and final transmembrane helix (TM4)(Fig. 3a). In the closed structure, TM4 points downward towards the cytosol, exposing the intracellular cavity to lipid acyl chains from the lipid bilayer. An acyl chain protrudes into the cavity through the lateral opening, blocking the ion conduction path (Fig. 3b). In the open structure, the C-terminal half of TM4 bends upwards to seal the lateral opening (Fig. 3c). The two major conclusions drawn from these structures are that 1) TRAAK is gated closed at the intracellular cavity by a lipid when TM4 is down, and 2) the conductive TM4 up conformation is energetically favored under membrane tension because it has greater channel cross-sectional area and cylindricity [49,50]. Crystal structures of TREK2 in analogous TM4 up and TM4 down conformations and TREK1 in a TM4 up conformation are consistent with the hypothesis that mechanosensitive gating occurs via movement of TM4 in mechanosensitive subfamily K2P channels [12,20].

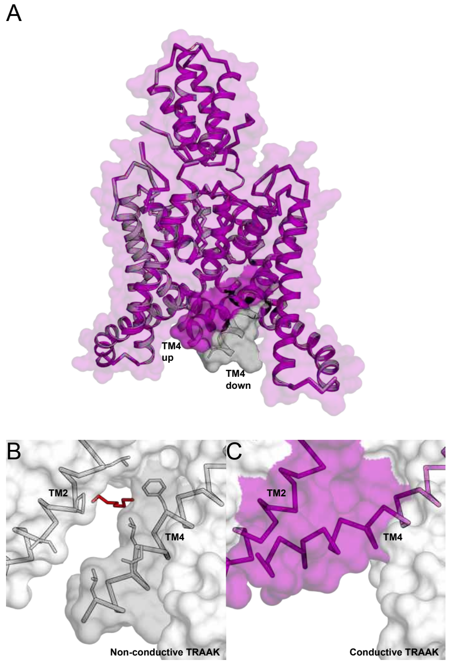

Figure 3 Gating of wild-type TRAAK by movement of transmembrane helix 4 (TM4).
(A) Overlay of conductive wild type TRAAK structure with TM4 in the up position closing the lateral opening (purple) and nonconductive wild type TRAAK structure with TM4 in the down position exposing the lateral opening (gray). TM4 are labeled and accentuated with an opaque surface representation.
(B) Zoom of nonconductive TRAAK TM4 in the down position and exposed lateral opening showing a lipid acyl chain (red) modeled entering the cavity. The acyl chain blocks the conduction axis.
(C) Zoom of conductive TRAAK TM4 in the up position and sealed lateral opening.

2.1.3 Distinct basal and mechanically activated activity in TRAAK channels

Single channel recordings of K2P channels including TRAAK show basal "leak type" currents and "stimuli gated" currents that have characteristic unitary conductances and kinetics [27,30,52,31–37,51]. Channels recorded under basal physiological conditions sample short flickery openings with a very low open probability. When channels are stimulated the open events increase in frequency and duration, which is reflected in the increased open probability. In TRAAK, the basal open probability increases from less than 0.01 to nearly 1 when the membrane is stretched. The observation of short flickery basal currents in K2P family channels motivates the hypothesis that these openings may occur via a conserved gate. However, at present the structural basis of the short flickery open state has not been determined for any K2P channel.

2.1.4 Models of TRAAK gating do not explain basal activity

In most models of TRAAK mechanical activation, TRAAK passes mechanically activated currents when TM4 is up, but the physical basis of the smaller basal currents is not defined. It seems unlikely that the mechanically activated TM4 up conformation also underlies the basal activity because the unitary currents are smaller and the kinetics are shorter [30,38]. The smaller currents might be explained by gates proposed in alternative models of mechanosensitive K2P gating including gating at the selectivity filter [25,53], partial or complete dewetting of the intracellular cavity [54,55], or gating that does not involve upward movement of TM4 [56]. Here, we show basal and mechanically gated TRAAK open states are distinct in their conductance, kinetics, and structure. We present a model for channel gating that assigns channel conformations observed in crystal structures to functional states observed in single channel recordings.

2.2 Results

2.2.1 Quantitation of wild type TRAAK basal and mechanically activated openings

Previous studies have observed subconductance openings with variable kinetics for most K2P family ion channels, including TRAAK, but a detailed kinetic analysis of single channels has not been made [30,38,57]. We recorded wild type TRAAK ($TRAAK_{WT}$) currents from patches of membrane excised from *Xenopus laevis* oocytes injected with hsTRAAK RNA. $TRAAK_{WT}$ activity can be mechanically stimulated 100-fold by applying pressure via suction to the excised patch to increase the membrane tension (Fig. 4a). We classify recordings by their open probability rather than the applied pressure because membrane tension also depends on the membrane configuration [58–61]. Varying the applied pressure allows us to sample a wide range of open probability in $TRAAK_{WT}$ channels ($0.01 \leq P_o \leq 0.98$)(Fig. 4b-e). Single channel recordings are grouped into three bins according to open probability (P_o). The distinct biophysical properties of each P_o bin are immediately obvious (Fig. 4c-e).

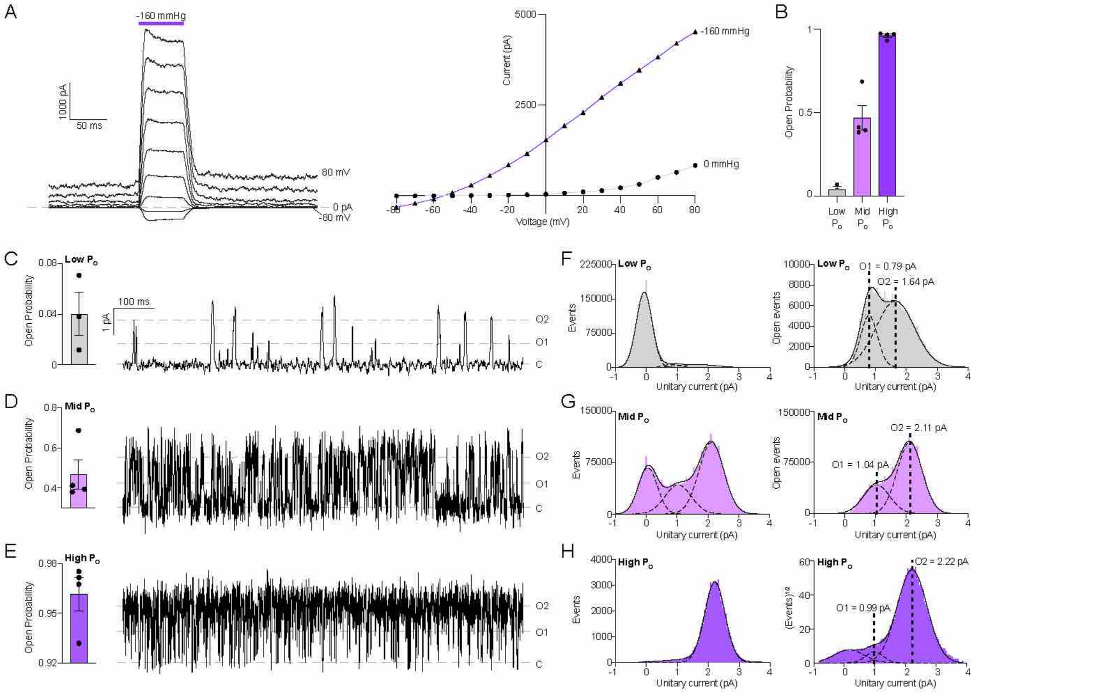

Figure 4 Distinct basal and mechanically activated open states in $TRAAK_{WT}$.
(A) Macroscopic currents recorded across an inside-out patch pulled from a TRAAK-expressing cell in response to a voltage step protocol ($V_{hold} = 0$, $V_{test} = -80$ to 80, $\Delta V = 10$ mV, 20 mV intervals displayed) with a pressure step applied at each voltage (purple bar) (left). Current-voltage relationship of the recording (right).
(B) Open probability calculated from single channel records (0.04 ± 0.02, 0.47 ± 0.07, and 0.96 ± 0.01 for low P_O, mid P_O, and high P_O, respectively (mean ± sem, n = 3, 4, and 4 patches)). All single channel data in the paper were recorded at $V_{hold} = 0$ mV in a ten-fold gradient of [K^+] and are presented in physiological convention.
(C-E) 1 s portion from representative low P_O, mid P_O, and high P_O recordings, respectively.
(F-H) All event (left) and open-only or square root all event (right) current histograms from representative low P_O, mid P_O, and high P_O recordings, respectively.

First, consistent with previous observations, TRAAK$_{WT}$ channel openings have two distinct unitary currents, a lower ~1 pA current and a higher ~2 pA current (Fig. 4b-e, Fig. 5). Mechanical activation increases the frequency of the ~2 pA openings. Channels in unstretched patches with low P_o sample both openings with almost equal frequency (Fig. 4f, Fig. 5a). When mechanically activated to intermediate P_o, the proportion of higher ~ 2 pA events increases, and at high P_o ~2 pA openings are strongly favored (Fig 4g, h, Fig. 5b,c). While the relative proportion of these two open events depends on the membrane tension, the magnitude of the unitary currents does not change significantly as a function of P_o (Fig. 6a).

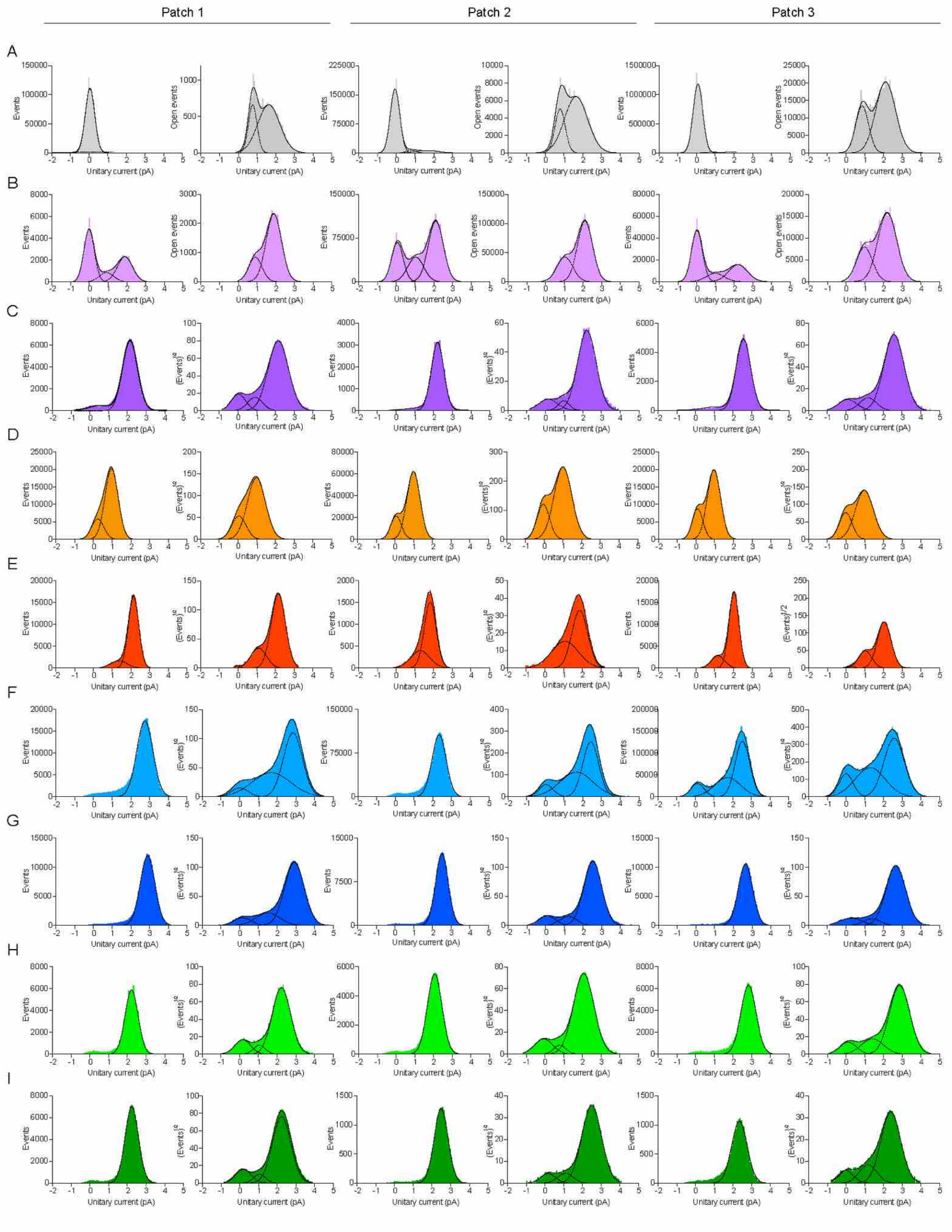

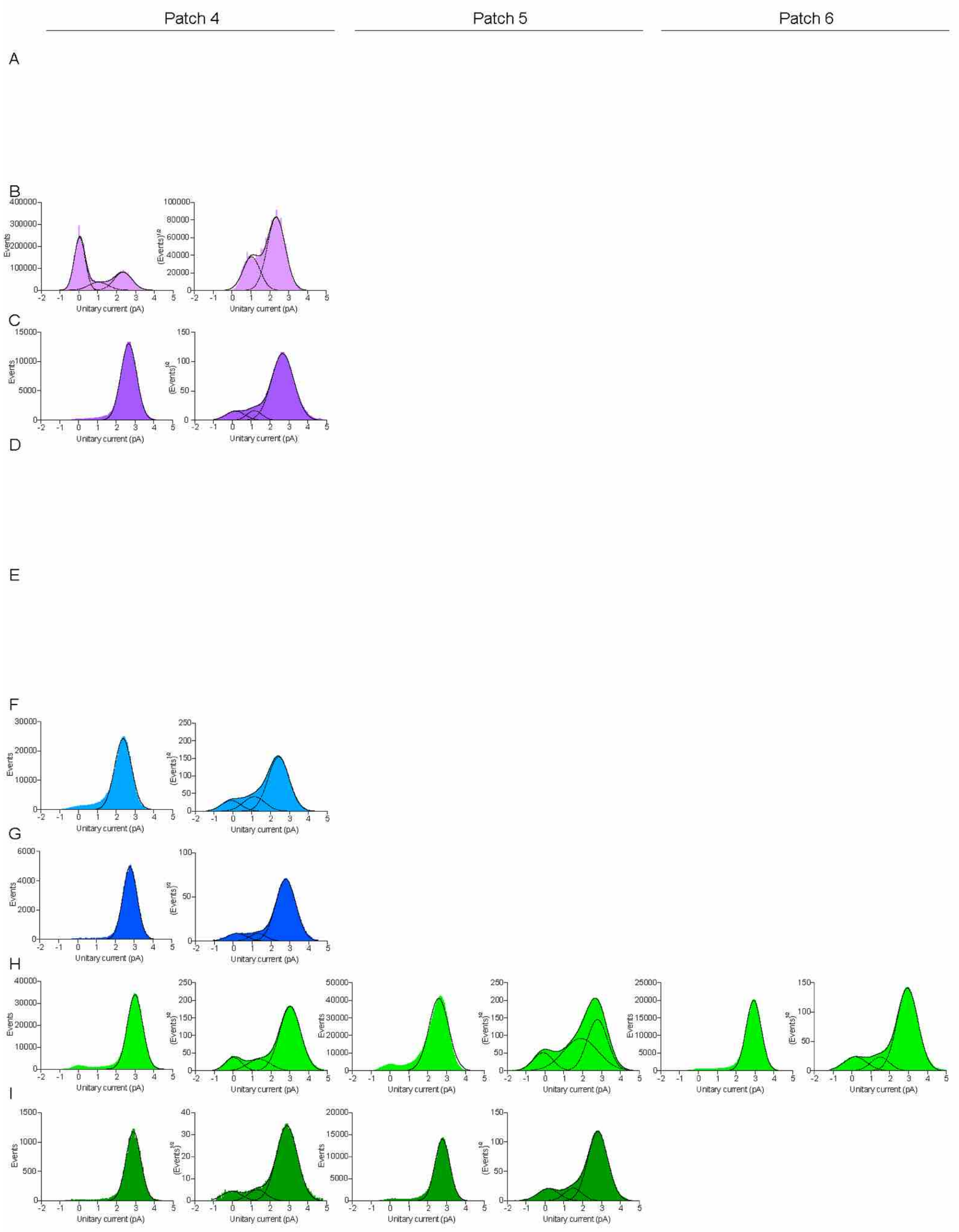

Figure 5 - Unitary current histograms.

Open event histograms with individual Gaussian fits (dashed lines) and summed fits (solid lines) for each record analyzed. (A) TRAAK$_{WT}$ low P$_O$, (B) TRAAK$_{WT}$ mid P$_O$, (C) TRAAK$_{WT}$ high P$_O$, (D) TRAAK$_{G158D}$, (E) TRAAK$_{G158D}$ with pressure, (F) TRAAK$_{A198E}$, (G) TRAAK$_{A198E}$ with pressure, (H) TRAAK$_{A270P}$, and (I) TRAAK$_{A270P}$ with pressure.

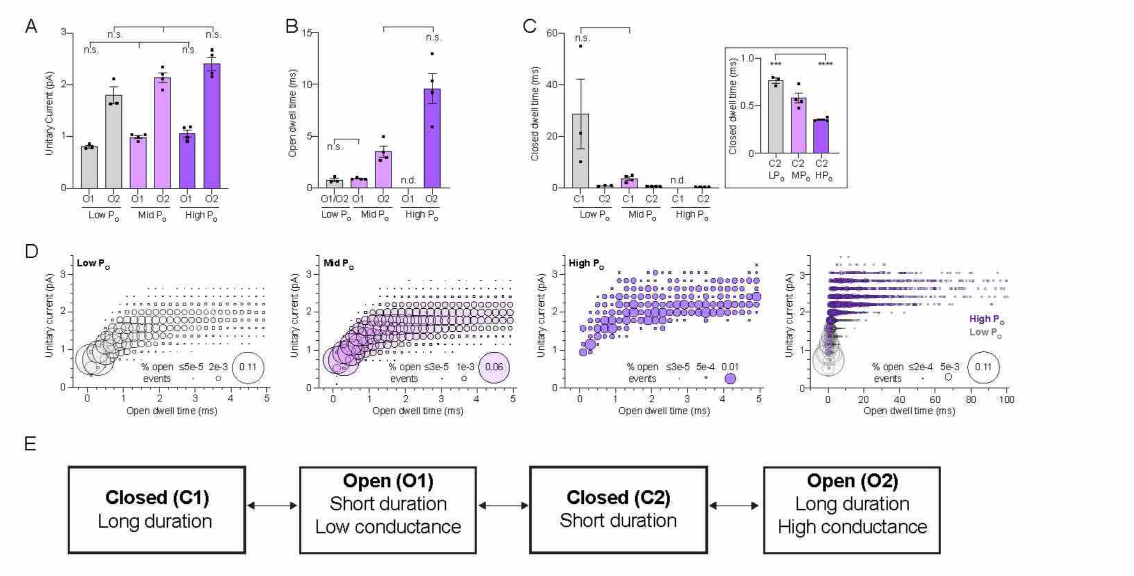

Figure 6 Proposed kinetic gating model of TRAAK$_{WT}$.

(A) Unitary currents of O1 and O2 states (0.81 ± 0.03 pA and 1.80 ± 0.16 pA, 0.99 ± 0.03 pA and 2.14 ± 0.09 pA, and 1.07 ± 0.07 pA and 2.41 ± 0.13 pA for low P_0, mid P_0, and high P_0 recordings, respectively (mean ± sem, n= 3, 4, and 4 patches)).

(B) Open dwell time of O1 and O2 states (0.80 ± 0.15 ms, 0.91 ± 0.05 ms and 3.52 ± 0.51 ms, and 9.60 ± 1.46 ms for low P_0, mid P_0, and high P_0 recordings, respectively (mean ± sem, n= 3, 4, and 4 patches)).

(C) Closed dwell times of C1 and C2 states (28.70 ± 13.50 and 0.77 ± 0.03 ms, 3.59 ± 0.67 and 0.58 ± 0.05 ms, and 0.35 ± 0.01 ms for low P_0, mid P_0, and high P_0 recordings, respectively (mean ± sem, n=3, 4, and 4 patches, n.d. not determined, n.s. not significant, ***p = 0.0006, ****p < 0.0001 (one-way ANOVA with Tukey correction)). C2 events are replotted in the inset on the right.

(D) Unitary current-open dwell time relationships for low P_0, mid P_0, and high P_0 open events and an overlay of low P_0 and high P_0 relationships at expanded time scale. Bubble size is proportional to percentage of open events.

(E) Four state TRAAK linear kinetic gating model.

Second, TRAAK$_{WT}$ openings can be classified into two kinetic types: short duration (~1 ms) and long duration (~3 ms or longer). Mechanical activation increases the duration of the long duration openings. The long and short open events are indistinguishable in recordings of single channels with low P_o in unstretched patches (Fig. 6b, Fig. 7a). At intermediate P_o the short and long duration open states become kinetically distinct (Fig. 7b). Mechanical activation to a high P_o, essentially eliminates short duration openings, and lengthens the duration of long open state (Fig. 6b, Fig. 7c). Mechanical activation increases the duration of the long open state as well as the frequency of the high conductance open state. In fact, open duration and unitary current are positively correlated: lower unitary current openings are distributed around ~1 ms dwell time, whereas higher unitary current openings are distributed around ~ 3 ms with a long shoulder that extends up to 100 ms open dwell time (Fig. 6d).

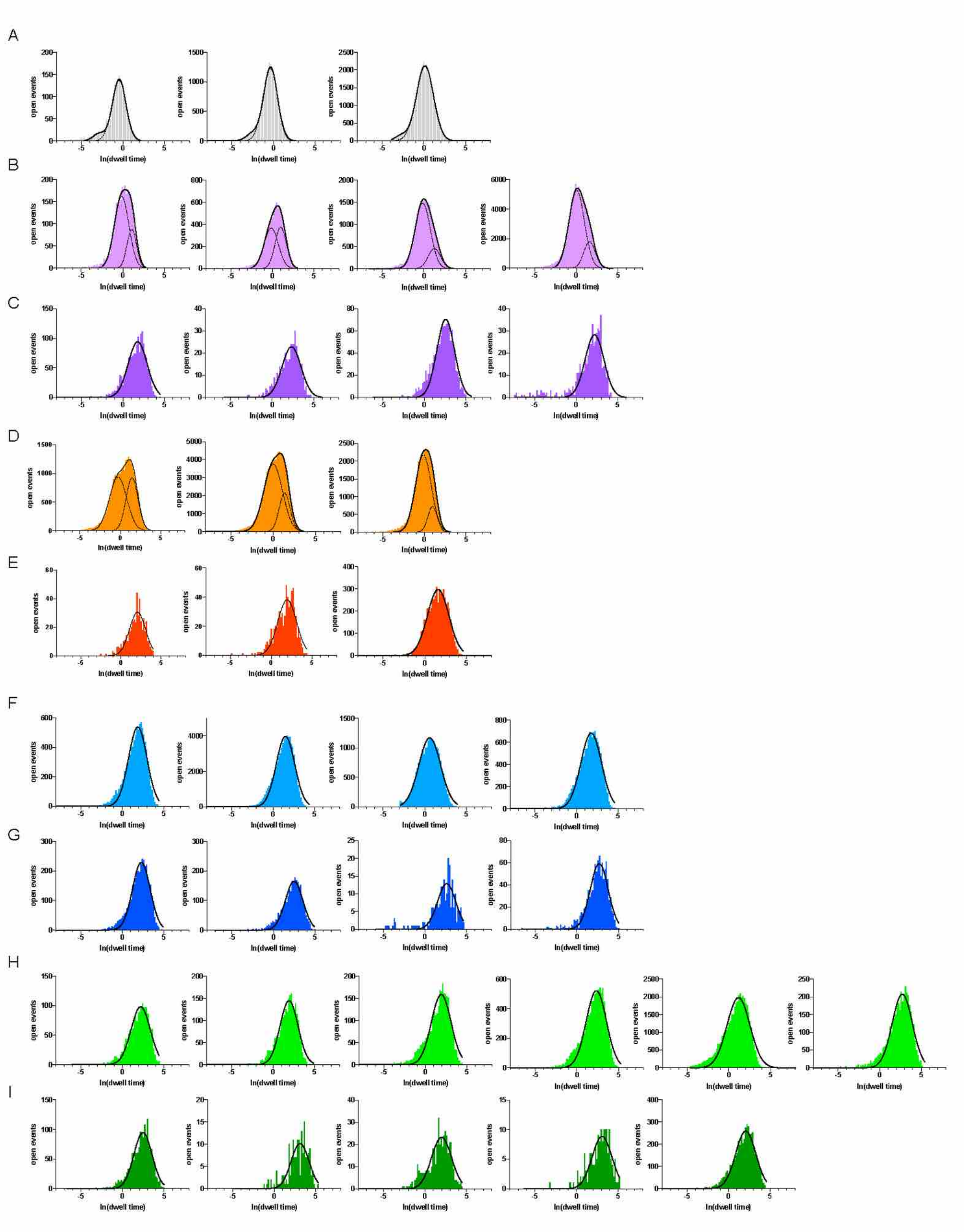

Figure 7 - Open event dwell time histograms.

Open event histograms with individual Gaussian fits (dashed lines) and summed fits (solid lines) for each record analyzed. (A) $TRAAK_{WT}$ low P_O, (B) $TRAAK_{WT}$ mid P_O, (C) $TRAAK_{WT}$ high P_O, (D) $TRAAK_{G158D}$, (E) $TRAAK_{G158D}$ with pressure, (F) $TRAAK_{A198E}$, (G) $TRAAK_{A198E}$ with pressure, (H) $TRAAK_{A270P}$, and (I) $TRAAK_{A270P}$ with pressure.

Third, TRAAK_{WT} closures are also tension dependent and kinetically distinguishable as either: long closures (~3 ms or longer) or short closures (~0.5 ms). At low P_o in unstretched patches, both long closures lasting tens of milliseconds and short closures are observed (Fig. 8a). Mechanically activating the channels to intermediate P_o sharply reduces the average duration of long closures to a few milliseconds (Fig. 6c, 8b). At high P_o, long closures are eliminated (Fig. 6c, Fig. 8c). While the duration of the long closures is strongly tension dependent, the duration of short closures is weakly dependent on membrane tension.

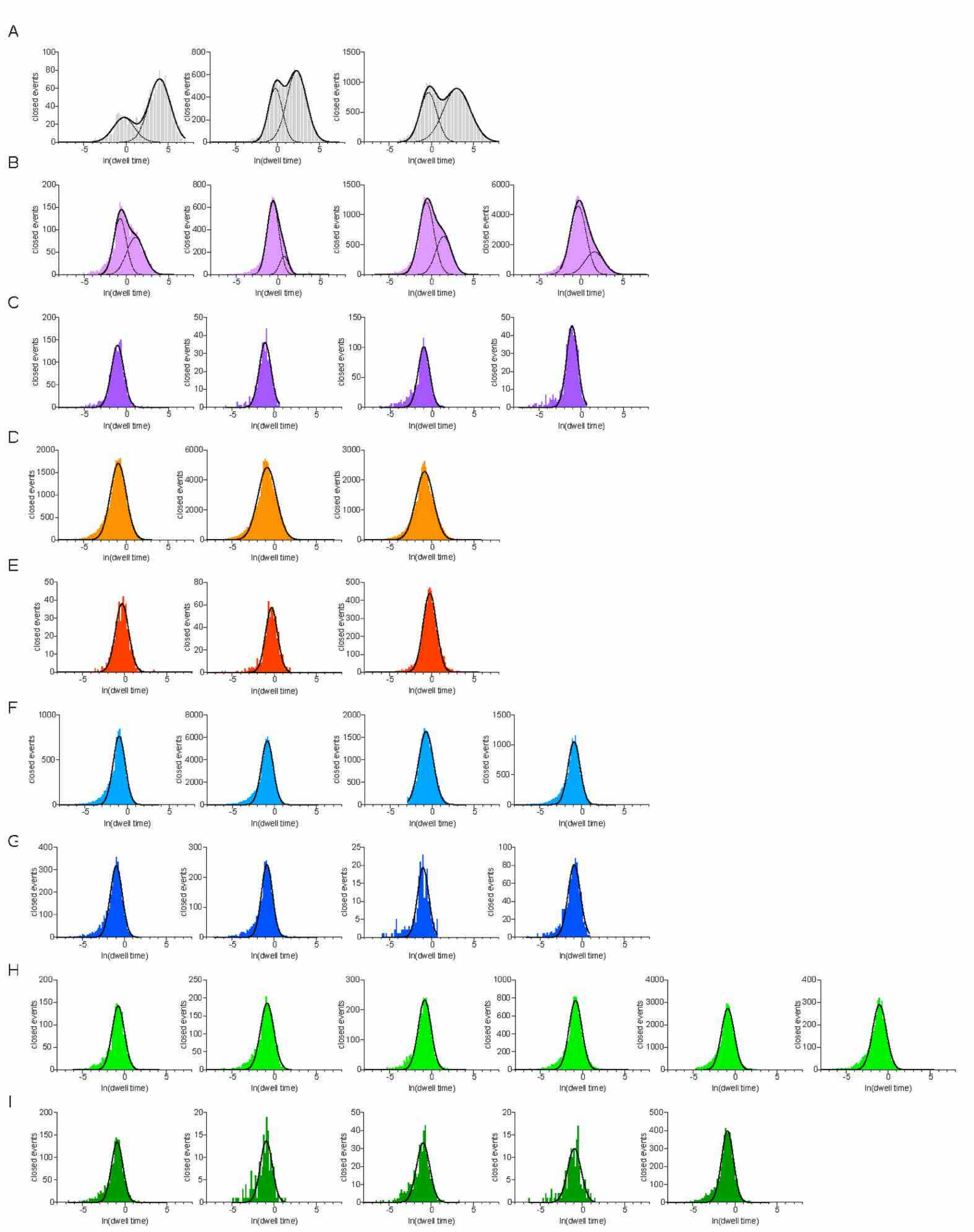

Figure 8 - Closed event dwell time histograms.
Closed event histograms with individual Gaussian fits (dashed lines) and summed fits (solid lines) for each record analyzed. (A) TRAAK_{WT} low P_O, (B) TRAAK_{WT} mid P_O, (C) TRAAK_{WT} high P_O, (D) $\text{TRAAK}_{\text{G158D}}$, (E) $\text{TRAAK}_{\text{G158D}}$ with pressure, (F) $\text{TRAAK}_{\text{A198E}}$, (G) $\text{TRAAK}_{\text{A198E}}$ with pressure, (H) $\text{TRAAK}_{\text{A270P}}$, and (I) $\text{TRAAK}_{\text{A270P}}$ with pressure.

Single channel recordings of TRAAK_{WT} basal openings at low P_o are fit with a linear kinetic model with two open states (O1, short open/low conductance and O2, long open/high conductance) and two closed states (C1, long closed and C2, short closed)(Fig. 6e). The duration of the long closed C1 and long open O2 states are dependent on membrane tension and are seldom observed in recordings of TRAAK_{WT} channels mechanically activated to high P_o. A two state model with the C2 short closed and O2 long open/ high conductance states in equilibrium more accurately describes TRAAK_{WT} gating in high P_o records. At intermediate P_o all four states are observed, but the O2 state is shorter than at high P_o, and the C1 state is shorter than at low P_o. The strong tension dependence of the O2 state suggests that it underlies mechanically activated openings, and the O1 state underlies basal openings at low P_o. Why then are O2 openings and O1 openings observed at equal frequency at low P_o when mechanical activation is weak? Adhesion forces between the membrane and the patch pipette may generate tension that transiently stabilizes the O2 open state [43,60]. The weak nature of the mechanical activation to the O2 state at low P_o is highlighted by the indistinguishable kinetics of the two states (Fig. 7a).

Single channel recordings clearly show that wild type human TRAAK has two distinct open states, but do not provide insight to the structural basis of each state. Previous structures of TRAAK_{WT} suggest that the mechanically activated O2 state underlies a TM4 up conformation with greater cross sectional area to the TM4 down state [42]. To definitively identify the channel conformation that underlies the O2 and O1 states, we solved crystal structures of three recently reported gain-of-function point mutants [18,62]. These mutants exhibit basal high P_o and are only weakly mechanically activated. We wondered if these gain-of-function mutants would preferentially stabilize either the O1 or O2 state to achieve high basal open probabilities.

2.2.2 Mechanical force and FHEIG point mutations promote a TM4 up conductive state

Point mutations $\text{TRAAK}_{\text{A198E}}$ and $\text{TRAAK}_{\text{A270P}}$ greatly increase basal activity and each cause FHEIG (Facial dysmorphism, Hypertrichosis, Epilepsy, Intellectual disability, and Gingival outgrowth) in humans (Fig. 9a, Fig. 10a) [18]. We confirmed that both FHIEG mutants have a high basal activity in excised patches and can only be weakly activated by applied membrane tension (Fig. 9b, c, Fig. 10b, c). Next, we recorded single $\text{TRAAK}_{\text{A198E}}$ and $\text{TRAAK}_{\text{A270P}}$ channels absent mechanical stimulation and observed primarily long duration O2 open events punctuated by short C2 closed events (Fig. 7f-i, Fig. 8f-i, Fig. 9d, f, Fig. 10d, f). The basal activity of the FHIEG mutants is strongly reminiscent of TRAAK_{WT} activated by mechanical force, and is best described by a two state model with long open/ high conductance O2 openings and short C2 closures (Fig. 9g, h, Fig. 10g, h). Mechanical force slightly increases the channel open probability of each mutant (Fig. 9b, c, Fig. 10b, c) but does not significantly change the unitary current or the duration of the open or closed states (Fig. 9f-h, Fig. 10f-h).

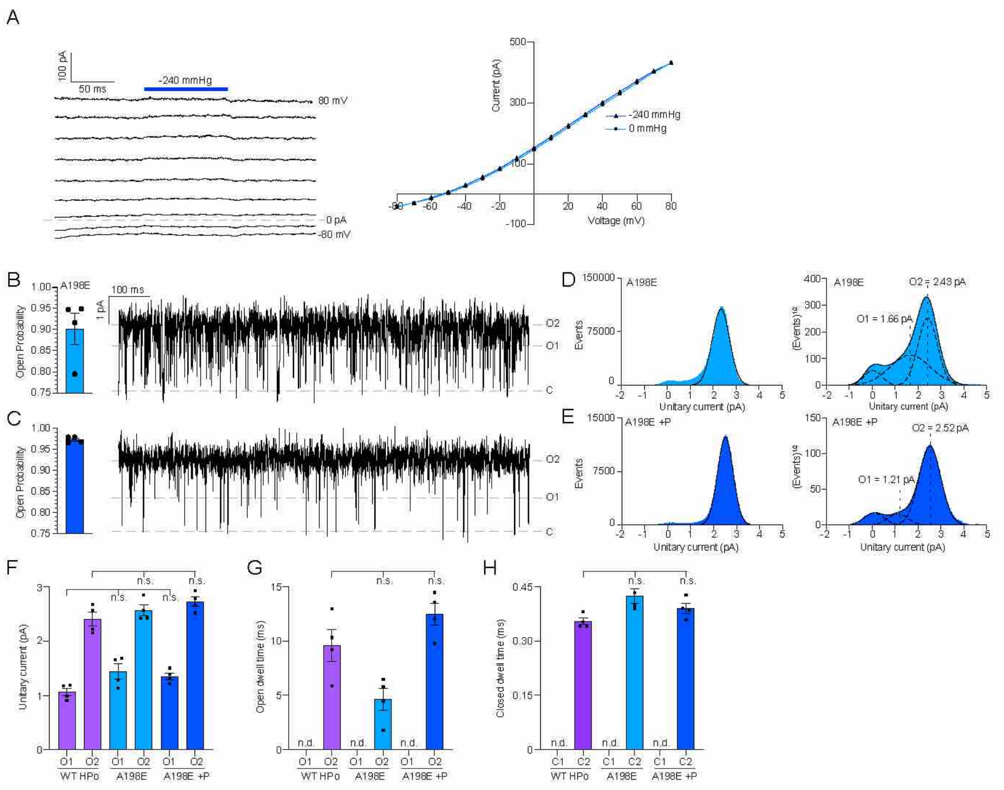

Figure 9 – The FHEIG mutation TRAAK$_{A198E}$ promotes a long duration, high conductance open state.

(A) Macroscopic currents from a TRAAK$_{A198E}$-containing patch in response to a voltage step protocol (V$_{hold}$ = 0, V$_{test}$ = -80 to 80, ΔV = 10 mV, 20 mV intervals displayed) with a pressure step applied at each voltage (dark blue bar)(left). Current-voltage relationship of the recording (right).

(B,C) Open probability calculated from all TRAAK$_{A198E}$ and TRAAK$_{A198E}$ with pressure (+P) records (left, P$_O$ = 0.90 ± 0.04 and P$_O$ = 0.97 ± 0.003 (mean ± sem, n = 4 patches) and 1 s portion from representative recordings.

(D,E) All event (left) and square root all event (right) current histograms from representative recordings.

(F) Unitary currents of TRAAK$_{WT}$ HP$_O$, TRAAK$_{A198E}$, and TRAAK$_{A198E}$+P O1 and O2 states (1.07 ± 0.07 and 2.41 ± 0.13 pA, 1.44 ± 0.14 and 2.57 ± 0.10 pA, and 1.35 ± 0.06 and 2.72 ± 0.09 pA, respectively).

(G) Open dwell times of TRAAK$_{WT}$ HP$_O$, TRAAK$_{A198E}$, and TRAAK$_{A198E}$+P O2 states (9.60 ± 1.46 ms, 4.63 ±1.03 ms, 12.46 ±1.02 ms, respectively).

(H) Closed dwell times of TRAAK$_{WT}$ HP$_O$, TRAAK$_{A198E}$, and TRAAK$_{A198E}$+P C2 (0.35 ± 0.01 ms, 0.42 ± 0.02 ms, and 0.39 ± 0.01 ms, respectively). For H-J, data are mean ± sem, n = 4 patches; n.d., not determined; n.s., not significant (one-way Anova with Dunnett correction).

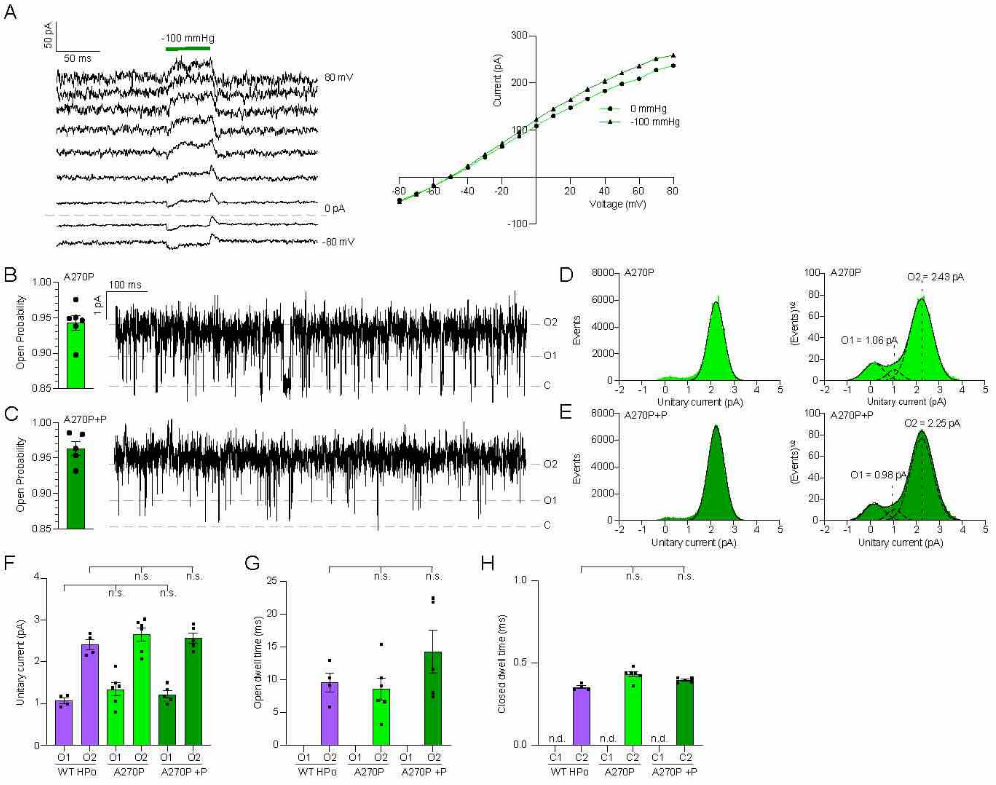

Figure 10 – The FHEIG mutation TRAAK$_{A270P}$ promotes a long duration, high conductance open state.

(A) Macroscopic currents from a TRAAK$_{A270P}$-containing patch in response to a voltage step protocol ($V_{hold} = 0$, $V_{test} = -80$ to 80, $\Delta V = 10$ mV, 20 mV intervals displayed) with a pressure step applied at each voltage (dark green bar) (left). Current-voltage relationship of the recording (right).

(B,C) Open probability calculated from all TRAAK$_{A270P}$ and TRAAK$_{A270P}$ with pressure (+P) records (left, $P_O = 0.94 \pm 0.01$ and $P_O = 0.96 \pm 0.01$ (mean ± sem, n = 6 and 5 patches) and 1 s portion from representative recordings.

(D,E) All event (left) and square root all event (right) current histograms from representative recordings.

(F) Unitary currents of TRAAK$_{WT}$ HP$_O$, TRAAK$_{A270P}$, and TRAAK$_{A270P}$+P O1 and O2 states (1.07 ± 0.07 and 2.41 ± 0.13 pA, 1.34 ± 0.15 and 2.65 ± 0.16 pA, and 1.21 ± 0.09 and 2.57 ± 0.12 pA, respectively).

(G) Open dwell times of TRAAK$_{WT}$ HP$_O$, TRAAK$_{A270P}$, and TRAAK$_{A270P}$+P O2 states (9.60 ± 1.46 ms, 8.56 ± 1.69 ms, and 14.47 ± 3.30 ms, respectively).

(H) Closed dwell times of TRAAK$_{WT}$ HP$_O$, TRAAK$_{A270P}$, and TRAAK$_{A270P}$+P C2 (0.35 ± 0.01 ms, 0.43 ± 0.01 ms, and 0.39 ± 0.01 ms, respectively). For H-J, data are mean ± sem, n = 4, 6, and 5 patches; n.d., not determined; n.s., not significant (one-way Anova with Dunnett correction)

Since the FHIEG mutants strongly stabilize the O2 open state in patches of membrane, we suspected that the O2 state might also be stabilized during nucleation and growth of a protein crystal. We determined the crystal structures of TRAAK$_{A198E}$ and TRAAK$_{A270P}$ in the presence of K$^+$ and in complex with a mouse monoclonal antibody Fab fragment to 2.5 Å and 3.0 Å resolution, respectively (Fig.

11, Fig. 12a, Fig. 13a). As previously reported, the crystal lattice grows via contacts between the Fab fragment and the TM2-TM3 intracellular loop of the A protomer (Fig. 14) [42]. The B protomer does not make any crystal contacts so the subsequent discussion describes the conformation of the B promoter unless otherwise noted. Both FHIEG mutants crystallized in a TM4 up conformation in crystallization conditions that grow crystals of TRAAK$_{WT}$ in the TM4 down conformation (Fig. 12a, c, Fig. 13a, b). The TRAAK$_{WT}$ TM4 down conformation is nonconductive because this position of TM4 exposes lateral openings through which lipid acyl chains enter the cavity and block the conduction of ions (Fig. 12b) [42]. The lateral opening is sealed in the FHEIG mutant structures, and spherical electron density characteristic of an ion is observed in the cavity (Fig, 12d, Fig. 13c). To verify the position of the ion in the cavity, TRAAK$_{A198E}$ crystals were also grown in Tl$^+$, and a structure was determined to 3.0 Å, and the anomalous diffraction of the Tl+ ions was used to unambiguously identify the ion binding sites in the channel. Strong anomalous signal was observed at the four sites in the selectivity filter (S1-S4), above the filter (S0), and in the cavity below the filter (Fig 12e), confirming that this conformation is conductive. Taken together, the crystal structure of each FHIEG mutant closely resembles the conductive conformation of TRAAK$_{WT}$.

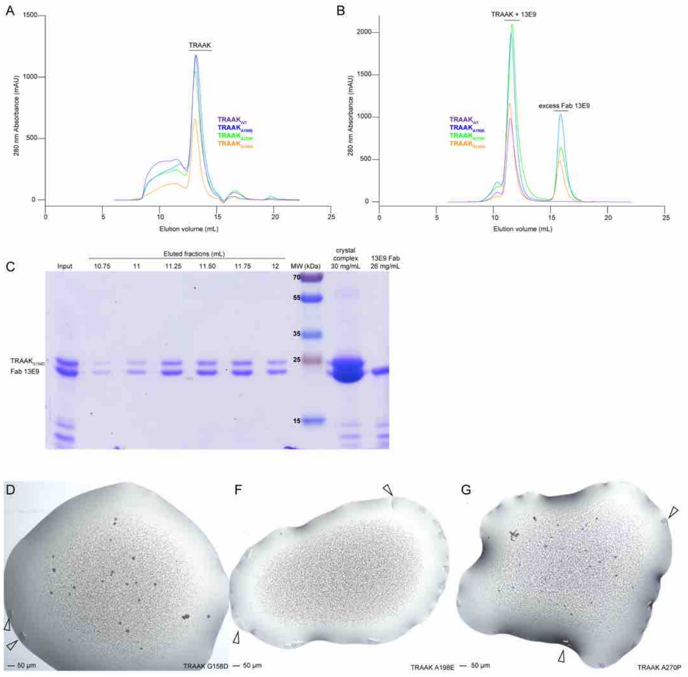

Figure 11 - Purification and crystallization of TRAAK$_{WT}$, TRAAK$_{A198E}$, TRAAK$_{A270P}$, and TRAAK$_{G158D}$.
(A) Chromatograms from purifications of TRAAK constructs over a Superdex 200 column. (B) Chromatograms purifications of 13E9 Fab – TRAAK construct complexes over a Superdex 200 column. (C) Coomassie-stained SDS-PAGE of fractions from TRAAK$_{G158D}$-13E9 Fab complex purification from (B). (D-G) Representative crystals grown of TRAAK$_{G158D}$, TRAAK$_{A198E}$, and TRAAK$_{A270P}$.

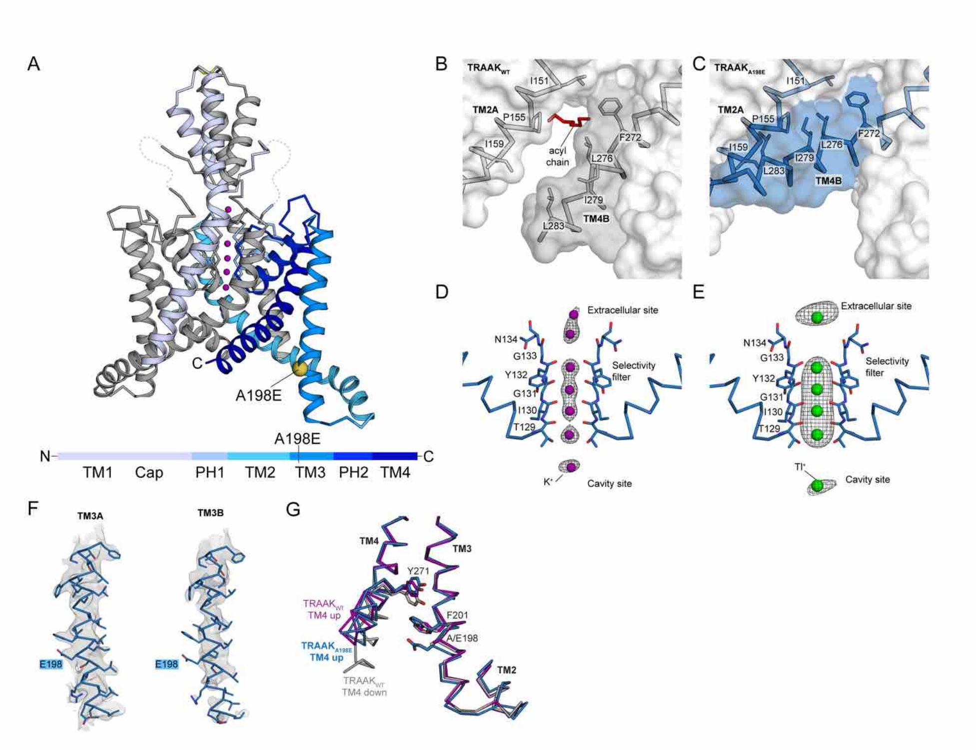

Figure 12 – The FHEIG mutation TRAAK$_{A198E}$ promotes a TM4-up open state.
(A) Crystal structure of TRAAK$_{A198E}$. Side view from the membrane plane with one protomer gray and the second protomer colored according to the key below. A198E is shown as a yellow sphere and K^+ ions are colored purple.
(B) View of the membrane-facing lateral opening in a TRAAK$_{WT}$ TM4-down structure (PDB 4WFF). A cavity-bound lipid acyl chain blocks conduction.
(C) TRAAK$_{A198E}$ in the same view as (B). A TM4-up conformation seals the membrane opening.
(D) Ions in the TRAAK$_{A198E}$-K^+ structure. Polder omit F_o-F_c density (grey) around K^+ ions (purple) displayed at 5 and 5.5 σ for selectivity filter and extracellular and cavity ions, respectively.
(E) Ions in a TRAAK$_{A198E}$-Tl^+ structure. Anomalous density (grey) around Tl^+ ions (green) displayed at 2.5 σ (extracellular / selectivity filter / cavity ions).
(F) TRAAK$_{A198E}$ TM3 and $2F_o$-F_c electron density displayed at 1 σ. Position of the mutation is indicated.
(G) Overlay of the TM2-TM3-TM4 interaction from TRAAK$_{A198E}$ and TRAAK$_{WT}$ structures. A198E sterically promotes a TM4-up open state.

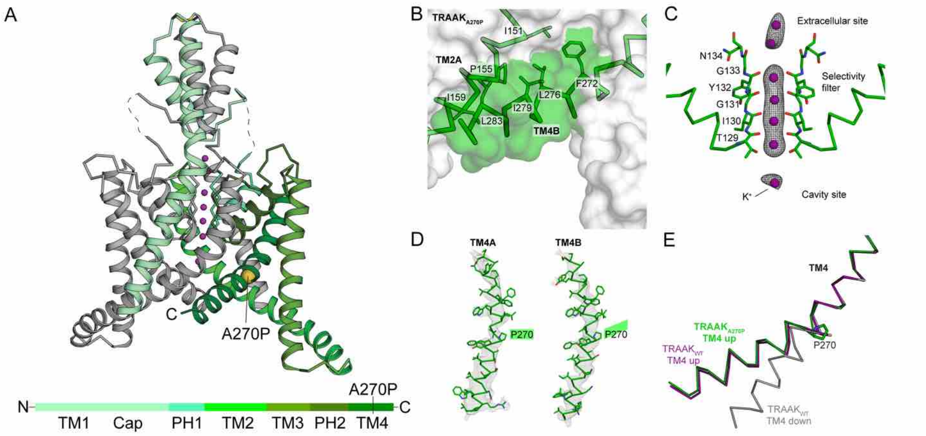

Figure 13 – The FHEIG mutation TRAAK$_{A270P}$ promotes a TM4-up open state.
(A) Crystal structure of TRAAK$_{A270P}$. Side view from the membrane plane with one protomer gray and the second protomer colored according to the key below. A270P is shown as a yellow sphere and K$^+$ ions are colored purple.
(B) View of the membrane-facing cytoplasmic half of TM4 in TRAAK$_{A270P}$. A TM4-up conformation seals the membrane opening.
(C) Ions in the TRAAK$_{A270P}$-K$^+$ structure. Polder omit F$_o$-F$_c$ density (grey) around K$^+$ ions (purple) displayed at 5 and 5.5 σ for extracellular and selectivity filter and cavity ions, respectively.
(D) TRAAK$_{A270P}$ TM4 and 2F$_o$-F$_c$ electron density displayed at 1 σ. Position of the mutation is indicated.
(E) Overlay of TM4 from TRAAK$_{A270P}$ and TRAAK$_{WT}$ structures. A270P kinks TM4 to promote a TM4-up open state.

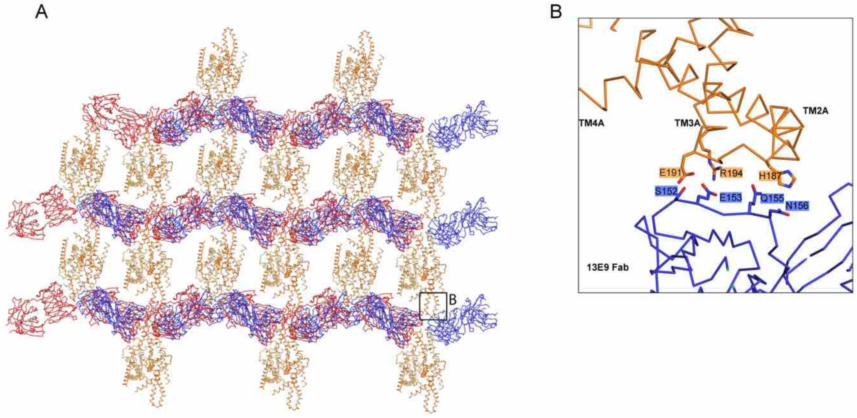

Figure 14 - Crystal packing and contacts between TRAAK and monoclonal Fab 13E9.
(A) Crystal lattice and (B) zoomed in view of contacts with TRAAK$_{G158D}$ colored orange and Fabs blue and red.

How does each FHIEG mutant stabilize the conductive TM4 up conformation? Comparing TRAAK$_{\text{A198E}}$ and TRAAK$_{\text{WT}}$ suggests two mechanisms in this mutant (Fig. 12f, g). The first is a steric relay from A198E through F201 and Y271 that favors TM4 up. In TRAAK$_{\text{WT}}$, the TM4 down conformation involves movement of Y271 1 Å towards the cytoplasm relative to TM4 up. This requires the intracellular TM2-TM3 linkage to rotate 15º away from TM4 to prevent a clash between Y271 on TM4 and F201 on TM3. In TRAAK$_{\text{A198E}}$, TM2-TM3 is similarly rotated out, but A198E pushes F201 closer to TM4 where it would clash with Y271 in a TM4 down conformation. A second possibility is that A198E causes local thinning of the lipid bilayer to favor TM4 up. While A198 is predicted to be embedded in the membrane inner leaflet facing hydrophobic residues on TM4 down, the negatively charged carboxylic acid of A198E likely favors hydration of this pocket, promoting TM4 up to maintain nonpolar interactions between its hydrophobic residues and lipid acyl chains [63,64].

In TRAAK$_{\text{A270P}}$, the introduced proline kinks TM4 to closely approximate the TRAAK$_{\text{WT}}$ TM4 up conformation (Fig. 13d, e). In TRAAK$_{\text{WT}}$, movement of TM4 up depends on a hinge at a conserved glycine G268. The A270P mutation instead disrupts backbone hydrogen bonding in TM4 and creates a ~27º bend and ~9.5 Å upward movement of TM4 relative to TRAAK$_{\text{WT}}$ TM4 down.

We conclude that mechanical force and the FHIEG point mutations promote a TM4 up conformation that underlies the O2 high conductance/long duration openings observed in single channel recordings. Several observations support this assignment: i) TRAAK$_{\text{A198E}}$ and TRAAK$_{\text{A270P}}$ channels have a high basal open probability absent mechanical activation that resembles TRAAK$_{\text{WT}}$ mechanically activated to high P$_{o}$ (Fig. 9b, c, Fig. 10b, c) ii) the gating of TRAAK$_{\text{A198E}}$ and TRAAK$_{\text{A270P}}$ and mechanically activated TRAAK$_{\text{WT}}$ can be best described by a two state short closure (C2) high conductance/long duration (O2) model (Fig. 9g, h, Fig. 10g, h) iii) the unitary current of O2 openings is indistinguishable between TRAAK$_{\text{A198E}}$ and TRAAK$_{\text{A270P}}$ and mechanically activated TRAAK$_{\text{WT}}$ (Fig. 9h, Fig. 10h) iv) the O2 long open durations are also kinetically indistinguishable and v) the crystal structures of TRAAK$_{\text{WT}}$ and TRAAK$_{\text{A198E}}$ and TRAAK$_{\text{A270P}}$ in a TM4 up conformation with sealed lateral openings and are conductive (Fig. 12b, Fig. 13c).

2.2.3 A TM4 down open state promoted by a pan-K2P activating mutation underlies basal activity

A third point mutant, TRAAK$_{\text{G158D}}$, increases the basal activity of TRAAK in upstretched patches, and point mutations in analogous positions increase the basal activity of every other K2P family ion channel [62]. We confirmed the high basal activity of TRAAK$_{\text{G158D}}$, and observed that it can be activated ~1.7-fold by stretching the membrane (Fig. 15a). This increased activity could arise from increased open probability, increased unitary current, or both. To determine the basis of mechanical activation we recorded the single TRAAK$_{\text{G158D}}$ channels with and without applied membrane tension (Fig. 15c, d). The basal open probability of TRAAK$_{\text{G158D}}$ (P$_{o}$ ~0.7) is much higher that TRAAK$_{\text{WT}}$ (P$_{o}$ ~0.04), and mechanical activation increases the P$_{o}$ ~1.25 fold (Fig. 15b). Basal openings of TRAAK$_{\text{G158D}}$ are low conductance with a unitary current ~1 pA, whereas mechanically activated openings are high conductance with a unitary current ~2 pA (Fig. 15e, f). The magnitude of the unitary current of O1 and O2 openings in TRAAK$_{G158D}$ is indistinguishable from TRAAK$_{WT}$ (Fig. 5 a-e, Fig. 15g).

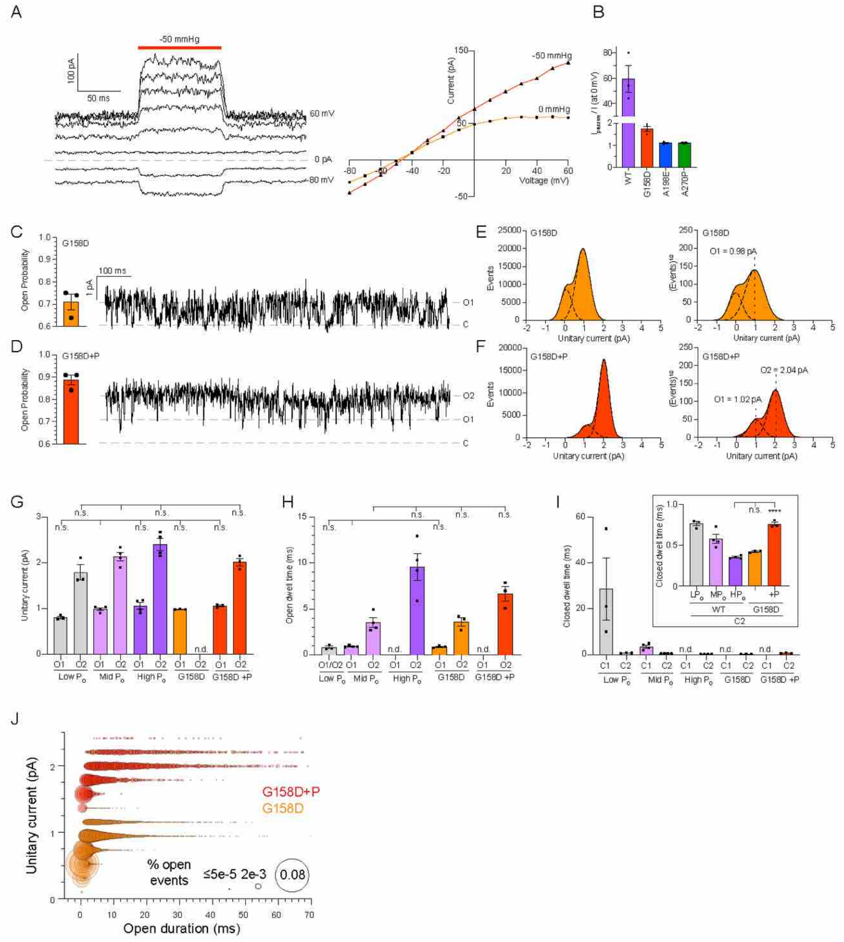

Figure 15 – The gain-of-function mutation TRAAK$_{G158D}$ promotes a short duration, low conductance open state.

(A) Macroscopic currents from a TRAAK$_{G158D}$-containing patch in response to a voltage step protocol (V$_{hold}$ = 0, V$_{test}$ = -80 to 80, ΔV = 10 mV, 20 mV intervals displayed) with a pressure step applied at each voltage (dark orange bar)(left). Current-voltage relationship of the recording (right).

(B) Maximum fold-activation by pressure of macroscopic TRAAK$_{WT}$, TRAAK$_{G158D}$, TRAAK$_{A198E}$, and TRAAK$_{A270P}$ currents with expanded scale in inset (59.33 ± 10.73, 1.75 ± 0.11, 1.11 ± 0.03, and 1.10 ± 0.03, respectively, mean ± sem, n = 3, 4, 3, and 3). (C,D) Open probability calculated from all TRAAK$_{G158D}$ and TRAAK$_{G158D}$ with pressure (+P) records (left, P$_O$ = 0.71 ± 0.04 and P$_O$ = 0.89 ± 0.02 (mean ± sem, n=3 patches) and 1s portion from representative recordings.

(E,F) All event (left) and square root all event (right) current histograms from representative recordings.

(G) Unitary currents of TRAAK$_{WT}$ LP$_O$, MP$_O$, HP$_O$, TRAAK$_{G158D}$, and TRAAK$_{G158D}$+P O1 and O2 states (0.81 ± 0.03 pA and 1.80 ± 0.16 pA, 0.99 ± 0.03 pA and 2.14 ± 0.09 pA, 1.07 ± 0.07 pA and 2.41 ± 0.13 pA, 0.99 ± 0.01, and 1.06 ± 0.02 and 2.02 ± 0.08 pA, respectively).

(H) Open dwell times of TRAAK$_{WT}$ LP$_O$, MP$_O$, HP$_O$, TRAAK$_{G158D}$, and TRAAK$_{G158D}$+P O1and O2 states (0.80 ± 0.15 ms, 0.91 ± 0.05 ms and 3.52 ± 0.51 ms, 9.60 ± 1.46 ms, 0.88 ± 0.07 and 3.58 ± 0.46 ms, and 6.63 ± 0.83 ms, respectively).

Kinetic analysis shows that TRAAK$_{G158D}$ closely resembles TRAAK$_{WT}$ except that the long duration closed state C1 is not observed (Fig. 8d, e, Fig. 15i). TRAAK$_{G158D}$ only samples short closed states (Fig. 15i). Similar to TRAAK$_{WT}$, TRAAK$_{G158D}$ accesses ~1 pA low conductance/short openings and ~2 pA high conductance/long openings (Fig. 7d, e, Fig 15g, h). Also like TRAAK$_{WT}$, high conductance/long openings are favored by mechanical stimulation (Fig. 15j).

Next, we determined the crystal structure of TRAAK$_{G158D}$ to 3.0 Å resolution in the presence of K$^+$ (Fig. 16a). TRAAK$_{G158D}$ crystallizes in the same conditions as TRAAK$_{WT}$ and the FHIEG mutants, but adopts a TM4 down conformation like TRAAK$_{WT}$ (Fig. 16b). Unlike TRAAK$_{WT}$, density in the TRAAK$_{G158D}$ cavity is consistent with a K$^+$ ion rather than the hydrophobic acyl chain present in the TRAAK$_{WT}$ TM4 down structure (Fig. 16c). This suggests that the TRAAK$_{G158D}$ structure represents a TM4 down open state and is consistent with the high basal open probability observed in single channel recordings.

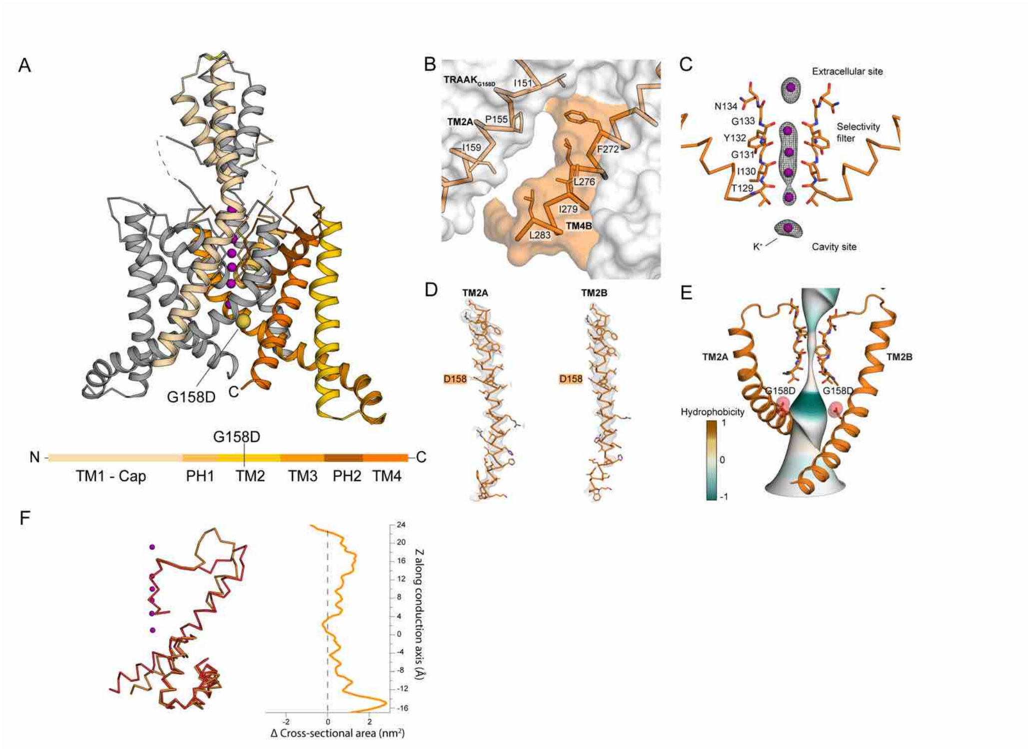

Figure 16 – The gain-of-function mutation TRAAK$_{G158D}$ promotes a TM4-down open state.
(A) Crystal structure of TRAAK$_{G158D}$. Side view from the membrane plane with one protomer gray and the second protomer colored according to the key below. G158D is shown as a yellow sphere and K$^+$ ions are colored purple.
(B) View of the membrane-facing cytoplasmic half of TM4 in TRAAK$_{G158D}$.
(C) Ions in the TRAAK$_{G158D}$-K$^+$ structure. Polder omit F_o-F_c density (grey) around K$^+$ ions (purple) displayed at 6.5 and 6 σ for selectivity filter and extracellular and cavity ions, respectively.
(D) TRAAK$_{G158D}$ TM2 model and $2F_o$-F_c electron density displayed at 1 σ. Position of the mutation is indicated.
(E) The conduction path in TRAAK$_{G158D}$ colored by hydrophobicity. G158D increases cavity electronegativity to promote a TM4-down open state.

(F) Change in cross sectional area between symmetric TRAAK$_{G158D}$ TM4-up and TRAAK$_{G158D}$ TM4-down conformations.

TRAAK$_{G158D}$ likely promotes a TM4 down open state through a simple electrostatic consequence of the mutation (Fig 16d, e). G158D projects into the channel cavity ~5 Å underneath the selectivity filter and increases hydrophilicity of the cavity close to where acyl chains are observed in the nonconductive TM4 down TRAAK$_{WT}$ structure. The electronegative cavity of TRAAK$_{G158D}$ is expected to disfavor acyl chain access and consequent channel block, instead promoting ion occupancy in the cavity and a conductive open state.

We conclude that TRAAK$_{G158D}$ promotes a TM4 down open state. The following lines of evidence support this assignment: i) TRAAK$_{G158D}$ has a high basal open probability (Fig. 15c) ii) the unitary current of the O1 state in TRAAK$_{G158D}$ and TRAAK$_{WT}$ is indistinguishable (Fig. 15g) iii) the mean dwell time of the O1 state is indistinguishable from TRAAK$_{WT}$ (Fig. 15h) iv) TRAAK$_{G158D}$ can be mechanically activated to accesses and strongly favor O2 openings (Fig. 15f, j) v) the conformation of the TRAAK$_{G158D}$ appears mechanosensitive because the TM4A in the A protomer is up, whereas TM4B is down, and TM4 up is expected to be energetically favored under membrane tension because it increases channel cross sectional area (Fig. 16f). The lower conductance of the O1 openings may be due to the reduced cavity polarity when TM4 is down and the lateral openings are exposed to the lipid bilayer, or a longer path length through the channel relative to the TM4 up conformation.

2.2.4 An integrated structural and functional model for TRAAK channel gating

Crystal structures and single channels records of TRAAK$_{198E}$, TRAAK$_{A270P}$, and TRAAK$_{G158D}$ support assignment of the low conductance/short duration O1 state to a TM4 down conformation and the high conductance/long duration O2 state to a TM4 up conformation. We further conclude that the TM4 down lipid-blocked closed state observed in the TRAAK$_{WT}$ structures corresponds to the long duration closed state C1. Analogous long duration closures are not observed in in TRAAK$_{G158D}$, TRAAK$_{A198E,}$ or TRAAK$_{A270P}$ (Fig. 6c, Fig. 9h, Fig. 10h, Fig 15i). In TRAAK$_{A198E}$ and TRAAK$_{A270P}$, this is likely because TM4s are favored in an up conformation that seals lateral membrane openings, preventing lipid access to the cavity (Fig. 12c, Fig. 13b). In TRAAK$_{G158D}$, this is likely because the mutation increases polarity of the channel cavity to disfavor occupancy of hydrophobic acyl chains (Fig. 16e).

Together, these data support a model for TRAAK gating shown in Figure 17 that maps structural conformations to the linear four-state kinetic model derived from single-channel records (Fig. 6e). Long duration closures (C1) correspond to the TM4 down, lipid blocked conformation captured in TRAAK$_{WT}$ structures [42]. Low conductance/short duration basal openings (O1) correspond to the TM4 down, conductive conformation captured in the TRAAK$_{G158D}$ structure. High conductance/long duration mechanically activated openings (O2) correspond to the TM4 up, conductive conformation captured in structures of TRAAK$_{A198E}$, TRAAK$_{A270P}$, and TRAAK$_{WT}$ with the activating small molecule Trichloroethanol. Structures of two other gain-of-function mutations, TRAAK$_{G124I}$ and TRAAK$_{W262S}$, have been previously reported [56], although their open probability, single channel behavior, and cavity ion occupancy is not known. However, both adopt TM4 down-like conformations and may promote O1-like openings similarly to TRAAK$_{G158D}$.

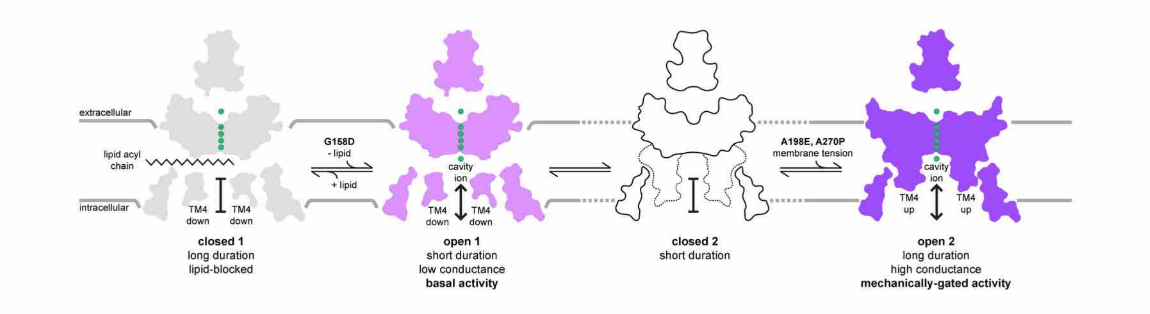

Figure 17 – An integrated model for TRAAK gating with distinct basal and mechanically gated open states. Known structures are mapped to the linear-four state model for TRAAK gating. Basal activity corresponds to a TM4-down, low conductance, short duration open state O1. Mechanically gated activity corresponds to a TM4-up, high conductance, long duration open state O2. Long duration closures correspond to a TM4-down lipid-blocked state C1. The unknown structure of the short duration closed state C2 is drawn without ions and the position of TM4 is indicated with dashed lines.

TRAAK$_{WT}$ under basal conditions transitions primarily between C1, O1, and C2 (Fig. 7a, Fig. 8a). Mechanical force favors the TM4 up open state O2 because it involves shape changes (relative to TM4 down) that are energetically favored in the presence of membrane tension, including an increase in cross-sectional area and cylindricity [42]. Mechanical force disfavors the TM4 down states C1 and O1 because the relatively smaller cross-sectional area and more wedge-shaped structure is disfavored under membrane tension. The gain of function mutations TRAAK$_{A198E}$ and TRAAK$_{A270P}$ mimic mechanically activated TRAAK$_{WT}$ by promoting a TM4 up conductive conformation (Fig. 12c, Fig. 13b). As a consequence, TRAAK$_{A198E}$ and TRAAK$_{A270P}$, like mechanically activated TRAAK$_{WT}$, primarily transition between O2 and C2 states (Fig. 5 f-I, Fig 7f-i, Fig 8f-i). Gain of function mutant TRAAK$_{G158D}$ mimics basally open TRAAK$_{WT}$, promoting a conductive TM4 down conformation by disfavoring lipid entry and channel block at low membrane tension. As a consequence, TRAAK$_{G158D}$ primarily transitions between O1, C2, and O2 states (Fig. 5d, e, Fig 7d, e, Fig 8d, e). Like TRAAK$_{WT}$, mechanical stimulation of TRAAK$_{G158D}$ disfavors O1 to favor transitions between O2 and C2 states (Fig. 5a-e).

The short duration closure (C2) does not yet have a defined structural correlate. We observe C2-like closures of similar duration in all TRAAK variants analyzed (Fig. 6c, Fig. 9h, Fig. 10h, Fig. 15i), suggesting they may occur independently of TM4 position or cavity environment. One possibility is that C2 closures represent gating at the selectivity filter. While gating conformational changes at the selectivity filter have not been observed in TRAAK, they have been hypothesized from functional data and visualized in other K2Ps including the mechanosensitive TREK1 in low K^+ conditions and pH-gated TASK2 in physiological K^+ and low pH conditions [25,53]. Alternatively, C2 closures could correspond to cavity dewetting that has been proposed to occur based on molecular dynamics simulations [54,55] or other, yet to be visualized, conformational rearrangements.

2.3 Materials and Methods

2.3.1 Electrophysiology

Full length hsTRAAK (Uniprot Q9NYG8-2) was codon optimized for eukaryotic expression, synthesized (Genewiz), and cloned into a modified pGEMHE vector using XhoI and EcoRI restriction sites such that the mRNA transcript encodes hsTRAAK 1-419 with an additional "SNS" at the C-terminus. Point mutants G158D, A198E, and A270P were generated by inverse PCR of the parent construct and verified by Sanger sequencing. cRNA was transcribed from linearized plasmids *in vitro* using T7 polymerase, and 0.1–10 ng cRNA was injected into *Xenopus laevis* oocytes extracted from anaesthetized frogs.

Currents were recorded at 25°C from inside-out patches excised from oocytes 1–5 days after mRNA injection. Pipette solution contained (in mM) 15 KCl, 135NaCl, 2$MgCl_2$, 10 HEPES, pH = 7.4 with NaOH. The solution in the bath contained 150 KCl, 2 $MgCl_2$, 10 HEPES, 1 EGTA, pH = 7.1 with KOH. All single channel records were made at a holding voltage of 0 mV and presented in physiological convention.

Currents were recorded using an Axopatch 200B Patch Clamp amplifier at a bandwidth of 1 kHz and digitized with an Axon Digidata 1550B at 50 to 500 kHz. To maintain the integrity of brief TRAAK dwell times, records were not further filtered unless explicitly stated. Baseline correction was performed manually based on the observable closed state for each recording; since there was no solution exchange in our experiments, no associated large drifts in baseline were observed. Portions of $TRAAK_{WT}$ records were assigned as low, mid, or high P_O for analysis. Low P_O was observed prior to pressure application, while mid and high P_O behavior was observed after pressure application. Portions of mutant records during pressure application were analyzed separately from mutant records prior to pressure application. High P_O $TRAAK_{WT}$ and mutant records with pressure were made with the highest achievable pressure prior to patch rupture. Single channel open-close transitions were idealized by half-amplitude threshold crossing and dwell time event lists were generated for each baseline corrected record. Dwell time histograms were generated from the dwell time event lists using custom built software[65] while the fits for these histograms were generated in GraphPad Prism version 9.0 using single, double, or triple Gaussian fits.

For unitary current analysis, event lists for $TRAAK_{WT}$ low P_O, $TRAAK_{WT}$ mid P_O, $TRAAK_{G158D}$, and $TRAAK_{G158D}$ with pressure were first generated in Clampfit 10.7, applying a 0.8 pA event detection cutoff. Currents were filtered to 10 kHz and were analyzed with a custom script in Python 3.7 using the pyABF module [66]. Each point in the filtered record was annotated as closed (C1/C2), open low conductance (O1), or open high conductance (O2) using the events list. To account for the sharp detection cutoff, openings were padded by an additional point on either side of the cutoff (these points corresponded to 100 us of ~0.5-1 pA current during openings and closings). Open only event lists were then generated by removing all closed points. Open event only lists were binned by 0.2 pA in current and 0.2 ms in time to generate bubble plots relating unitary current and mean open duration for $TRAAK_{WT}$ and $TRAAK_{G158D}$. Open only event lists were also used to generate open event current histograms to distinguish relatively rare low conductance openings from prevalent closed events. Mean unitary currents for $TRAAK_{WT}$ low P_0 and $TRAAK_{WT}$ mid P_0 were derived from Gaussian fits to these open event current histograms. Mean unitary currents for $TRAAK_{WT}$ high P_0 and all mutants were derived from Gaussian fits to square root total event current histograms in order to distinguish conductance states when one state is present at higher frequency.

2.3.2 TRAAK expression and purification

Human TRAAK UniProt Q9NYG8-2 was cloned for expression in *Pichia pastoris* cells as previously described [24] with modifications described here. The construct used for purification included an additional 26 amino acid N-terminal sequence compared to Q9NYG8-1 that improved heterologous expression. The final construct is C-terminally truncated by 119 amino acids, incorporates two mutations to remove N-linked glycosylation sites (N104Q/N108Q), and is expressed as a C-terminal PreScission protease-cleavable EGFP-10xHis fusion protein. As a result, there is an additional amino acid sequence of “SNSLEVLFQ” at the C-terminus of the final purified protein after protease cleavage. Recombinant *Pichia* were grown in a 4 liter fermenter and harvested 48-72h after induction with methanol.

30-120g of frozen *Pichia* cells expressing TRAAK were disrupted by milling (Retsch model MM301) 5 times for 3 minutes at 25 Hz. All subsequent purification steps were carried out at 4 ºC. Milled cells were resuspended in buffer A (in mM) 50 Tris pH 8.0, 150 KCl, 1 EDTA 0.1 mg/mL DNase1, 1 mg/mL pepstatin, 1 mg/mL leupeptin, 1 mg/mL aprotinin, 10 mg/mL soy trypsin inhibitor, 1 mM benzamidine, 100 μM AEBSF, 1 μM E-64, and 1 mM phenylmethysulfonyl fluoride (added immediately before use) at a ratio of 1 g cell pellet per 4 mL lysis buffer and sonicated for 16 minutes with a duty cycle of 15 seconds of sonication per minute. The solution was ultracentrifuged at 150,000 xg for 1 hour at 4 ºC. Pellets were transferred to a Dounce homogenizer in buffer B (buffer A + 60 mM DM). Following homogenization, solutions were stirred for 3 hours at 4 ºC followed by centrifugation at 33,000g for 45 minutes. Anti-GFP nanobody resin (1 mg purified anti-GFP nanobody conjugated to 1 mL resin) was washed in Buffer B and added to the supernatant at a ratio of 1 mL resin / 15 g *Pichia* cells. The solution was gently stirred for 3 hours. Resin was collected on a column and washed in 15 column volumes (CV) of Buffer C (buffer A +6 mM DM+ 150 mM KCl), followed by 2 CV Buffer D (buffer A +6 mM DM). The resin was resuspended in ~3 CV of Buffer D with 1 mg purified Precission protease and gently rocked in column overnight. Cleaved TRAAK was eluted in ~4 CV of Buffer D, concentrated (50 kDa MWCO), and applied to a Superdex 200 SEC column (GE Healthcare) equilibrated in Buffer E (20 mM Tris pH 8.0, 150 mM KCl, 1 mM EDTA, 4 mM DM). Peak fractions were pooled and concentrated to 200-300 μL for incubation with Fab 13E9 and subsequently applied to a Superdex 200 column (GE Healthcare) equilibrated in Buffer E. Fab 13E9 was prepared as described previously[42]. TRAAK-Fab complexes were pooled and concentrated to 25-33 mg/mL for hanging drop crystallization.

For crystallization in Tl^+, all purification steps were conduction as with KCl, with two exceptions: KCl is substituted for KNO_3 for all buffers except Buffer E, where KCl is substituted with $TlNO_3$.

2.3.3 Protein Crystallization

Crystals were grown in drops of 0.125–0.250 µL protein added to an equal volume of reservoir, in hanging drops over a 100 µL reservoir at 4 ºC. Reservoir for each mutant in KCl was 50mM Tris pH 8.8, 64-200 mM $CaCl_2$, 27–33%(vol/vol) PEG400. Reservoir for each mutant in $TlNO_3$ was 50 mM Tris pH 8.8, 64-200 mM $Ca(NO3)_2$, 27–33%(vol/vol)PEG400. Lower Calcium concentrations were observed to correspond to increased nucleation and rapid growth of large, well-ordered crystals. Crystals grew to ~100 µm x 100 µm x 200 µm in 1–5 weeks. TRAAK A270P crystals rarely achieved sizes larger than 70 µm x 70 µm x 100 µm after 5 weeks.

For cryoprotection, an approximately equal volume of mother liquor supplemented to be 30%(vol/vol) PEG400 was added to one side of the drop and crystals were moved through this solution with a cryoloop before being plunged into liquid nitrogen.

2.3.4 X-ray Data Collection, Model Building & Refinement

Data were collected at beamline 8.3.1 at the ALS, or 24-IDC & 24-IDE at the APS. Thallium-containing crystals were collected at 12680 eV, and Potassium-containing crystals were collected at 12663 eV. Were rotated 360 degrees, and data were collected in 0.20 degree wedges with a 0.25 second exposure time per wedge. Datasets were processed as individual wedges in XDS [67,68]. Some datasets were truncated to eliminate redundant data displaying beam-induced damage prior to scaling with XSCALE, and merging with XDSCONV [67]. Due to the anisotropy of the data, elliptically truncated resolution cutoffs generated by STARANISO [69] were used to increased overall resolution of the maps. Structures were solved by molecular replacement using Phaser [70] with an input model of nonconductive hsTRAAK for G158D (PDB ID 4WFF) and conductive hsTRAAK for A198E and A270P mutants (PDB ID 4WFE). Structure refinement was carried out in Coot [71] and Refmac5 [72]. Jelly body and automatically generated local NCS constraints were used throughout refinement. For the final round of refinement, three TLS groups per protein chain were incorporated. Molprobity was used to assess model geometry in later stages of refinement [73].

Ion occupancy in the conduction axis was determined by calculating either a model phased anomalous difference map for A198E crystals grown in Thallium, or a Polder map for G158D and A270P crystals grown Potassium. In all maps, density in the filter fits well to ions occupying the S1, 2, 3, and 4 positions. Similarly, densities above the filter (S0) are well fit with one or two ions. Density in the cavity below the filter is also fit with an ion. All ion occupancies are set to 1.

The angle and orientation of transmembrane helix 4 in each model was compared using UCSF Chimera [74]. Cross-sectional area calculations were performed with CHARMM [63,64,75]. The area calculation used a surface calculated with 1.4 Å added to the van der Waals radii of protein atoms, and a probe radius of 3.5 Å to approximate lipid-accessible surface area. A water cylinder with a 6 Å radius was used to fill the cavity of TRAAK channels to exclude its contribution from the calculation. All calculations are made with channels containing symmetric protomers of the B chain, which does not make a contact in the crystal. Symmetric molecules were generated by rotation of the B protomer about the conduction axis, using pore helix and selectivity filter residues 119-133 and 228-242. Pore radii and pore-lining residue hydropathy were calculated with CHAP [76] using a pathway lining residue margin value of 0.55 and a hydrophobicity kernel bandwidth of 0.45.

2.4 Tables

2.4.1 Table 1 – Summary of all single channel recording data

		Record Properties		State Properties						Transition Rates (1/s)					
		Record length (s)	Open Probability	Duration (ms)	Duration (ms)	Unitary Current (pA)	Duration (ms)	Duration (ms)	Unitary Current (pA)						
				C2	O1		C2	O2		C1-O1	O1-C1	O1-C2	C2-O1	C2-O2	O2-C2
TRAAK WT low Po	**1**	134	0.01	54.93	0.62	0.77	0.79	n.d.	1.63	11	995	810	294	81	477
	2	235	0.07	10.02	0.68	0.79	0.80	n.d.	1.64	43	635	402	543	67	395
	3	1627	0.04	21.14	1.11	0.86	0.71	n.d.	2.12	11	427	305	339	144	243
	total/mean	1996	0.04	28.70	0.80	0.81	0.77	n.d.	1.80	22	686	506	392	97	372
	s.e.m.		0.02	13.50	0.15	0.03	0.03	n.d.	0.16	11	166	155	77	24	69
TRAAK WT mid Po	**1**	13	0.41	2.97	0.87	0.91	0.48	2.95	1.90	168	226	914	344	253	282
	2	125	0.40	4.36	0.87	0.98	0.57	3.48	2.21	145	308	743	441	338	249
	3	402	0.69	2.03	0.86	1.04	0.55	2.68	2.11	283	53	348	424	825	478
	4	629	0.38	5.02	1.06	1.04	0.73	4.97	2.34	55	137	523	492	231	192
	total/mean	1170	0.47	3.59	0.91	0.99	0.58	3.52	2.14	163	181	632	425	412	300
	s.e.m.		0.07	0.67	0.05	0.03	0.05	0.51	0.09	47	55	124	31	140	62
TRAAK WT high Po	**1**	6	0.97	*n.d.*	*n.d.*	1.18	0.34	9.22	2.67	*n.d.*	*n.d.*	*n.d.*	*n.d.*	2681	90
	2	20	0.98	*n.d.*	*n.d.*	1.19	0.38	12.96	2.57	*n.d.*	*n.d.*	*n.d.*	*n.d.*	2329	60
	3	6	0.97	*n.d.*	*n.d.*	0.99	0.34	10.31	2.22	*n.d.*	*n.d.*	*n.d.*	*n.d.*	2512	73
	4	14	0.93	*n.d.*	*n.d.*	0.91	0.35	5.88	2.16	*n.d.*	*n.d.*	*n.d.*	*n.d.*	1703	124
	total/mean	46	0.96	*n.d.*	*n.d.*	1.07	0.35	9.59	2.40	*n.d.*	*n.d.*	*n.d.*	*n.d.*	2306	87
	s.e.m.		0.01	*n.d.*	*n.d.*	0.07	0.01	1.47	0.13	*n.d.*	*n.d.*	*n.d.*	*n.d.*	214	14
TRAAK G158D	**1**	90	0.75	*n.d.*	0.75	0.99	0.41	4.18	*n.d.*	420	124	991	893	1168	400
	2	278	0.74	*n.d.*	0.99	1.00	0.43	3.89	*n.d.*	288	206	609	604	1204	307
	3	95	0.64	*n.d.*	0.89	0.98	0.43	2.68	*n.d.*	323	427	471	850	1438	381
	total/mean	463	0.71	*n.d.*	0.88	0.99	0.42	3.58	*n.d.*	344	252	690	782	1270	363
	s.e.m.		0.04	*n.d.*	0.07	0.01	0.01	0.46	*n.d.*	39	90	156	90	85	28
TRAAK G158D + pressure	**1**	5	0.84	*n.d.*	*n.d.*	1.10	0.74	7.87	2.16	*n.d.*	*n.d.*	*n.d.*	*n.d.*	1001	97
	2	7	0.91	*n.d.*	*n.d.*	1.02	0.81	5.05	2.04	*n.d.*	*n.d.*	*n.d.*	*n.d.*	1060	105
	3	56	0.91	*n.d.*	*n.d.*	1.07	0.73	6.97	1.87	*n.d.*	*n.d.*	*n.d.*	*n.d.*	631	119
	total/mean	68	0.89	*n.d.*	*n.d.*	1.06	0.76	6.63	2.02	*n.d.*	*n.d.*	*n.d.*	*n.d.*	897	107
	s.e.m.		0.02	*n.d.*	*n.d.*	0.02	0.03	0.83	0.08	*n.d.*	*n.d.*	*n.d.*	*n.d.*	134	6
TRAAK A198E	**1**	82	0.95	*n.d.*	*n.d.*	1.68	0.39	6.47	2.85	*n.d.*	*n.d.*	*n.d.*	*n.d.*	2693	108
	2	451	0.92	*n.d.*	*n.d.*	1.66	0.43	4.44	2.43	*n.d.*	*n.d.*	*n.d.*	*n.d.*	1782	162
	3	91	0.79	*n.d.*	*n.d.*	1.28	0.48	1.81	2.57	*n.d.*	*n.d.*	*n.d.*	*n.d.*	1476	356
	4	119	0.95	*n.d.*	*n.d.*	1.13	0.40	5.78	2.43	*n.d.*	*n.d.*	*n.d.*	*n.d.*	2006	112
	total/mean	743	0.90	*n.d.*	*n.d.*	1.44	0.42	4.63	2.57	*n.d.*	*n.d.*	*n.d.*	*n.d.*	1989	185
	s.e.m.		0.04	*n.d.*	*n.d.*	0.14	0.02	1.03	0.10	*n.d.*	*n.d.*	*n.d.*	*n.d.*	259	58
TRAAK A198E + pressure	**1**	51	0.97	*n.d.*	*n.d.*	1.50	0.38	9.79	2.93	*n.d.*	*n.d.*	*n.d.*	*n.d.*	2295	76
	2	45	0.97	*n.d.*	*n.d.*	1.21	0.43	12.01	2.52	*n.d.*	*n.d.*	*n.d.*	*n.d.*	1762	62
	3	4	0.98	*n.d.*	*n.d.*	1.39	0.36	13.57	2.66	*n.d.*	*n.d.*	*n.d.*	*n.d.*	2427	55
	4	20	0.98	*n.d.*	*n.d.*	1.31	0.39	14.45	2.79	*n.d.*	*n.d.*	*n.d.*	*n.d.*	2289	52
	total/mean	119	0.97	*n.d.*	*n.d.*	1.35	0.39	12.46	2.72	*n.d.*	*n.d.*	*n.d.*	*n.d.*	2193	61
	s.e.m.		0.00	*n.d.*	*n.d.*	0.06	0.01	1.02	0.09	*n.d.*	*n.d.*	*n.d.*	*n.d.*	147	5
TRAAK A270P	**1**	22	0.95	*n.d.*	*n.d.*	1.06	0.48	9.03	2.24	*n.d.*	*n.d.*	*n.d.*	*n.d.*	1576	81
	2	23	0.95	*n.d.*	*n.d.*	0.80	0.44	6.86	2.07	*n.d.*	*n.d.*	*n.d.*	*n.d.*	1939	110
	3	87	0.98	*n.d.*	*n.d.*	1.49	0.36	15.41	2.95	*n.d.*	*n.d.*	*n.d.*	*n.d.*	1862	45
	4	28	0.94	*n.d.*	*n.d.*	1.41	0.44	6.63	2.86	*n.d.*	*n.d.*	*n.d.*	*n.d.*	1685	111
	5	150	0.95	*n.d.*	*n.d.*	1.38	0.44	10.26	3.02	*n.d.*	*n.d.*	*n.d.*	*n.d.*	1298	70
	6	240	0.90	*n.d.*	*n.d.*	1.90	0.43	3.18	2.78	*n.d.*	*n.d.*	*n.d.*	*n.d.*	1597	197
	total/mean	551	0.94	*n.d.*	*n.d.*	1.34	0.43	8.56	2.65	*n.d.*	*n.d.*	*n.d.*	*n.d.*	1660	102
	s.e.m.		0.01	*n.d.*	*n.d.*	0.15	0.02	1.69	0.16	*n.d.*	*n.d.*	*n.d.*	*n.d.*	93	22
TRAAK A270P + pressure	**1**	27	0.96	*n.d.*	*n.d.*	0.98	0.41	11.65	2.25	*n.d.*	*n.d.*	*n.d.*	*n.d.*	1646	62
	2	5	0.99	*n.d.*	*n.d.*	1.10	0.40	22.44	2.50	*n.d.*	*n.d.*	*n.d.*	*n.d.*	2341	34
	3	5	0.93	*n.d.*	*n.d.*	1.17	0.38	7.39	2.39	*n.d.*	*n.d.*	*n.d.*	*n.d.*	1987	96
	4	5	0.98	*n.d.*	*n.d.*	1.33	0.39	21.85	2.90	*n.d.*	*n.d.*	*n.d.*	*n.d.*	1926	33
	5	59	0.95	*n.d.*	*n.d.*	1.50	0.41	8.02	2.80	*n.d.*	*n.d.*	*n.d.*	*n.d.*	1757	84
	total/mean	101	0.96	*n.d.*	*n.d.*	1.22	0.40	14.27	2.57	*n.d.*	*n.d.*	*n.d.*	*n.d.*	1931	62
	s.e.m.		0.01	*n.d.*	*n.d.*	0.09	0.01	3.30	0.12	*n.d.*	*n.d.*	*n.d.*	*n.d.*	119	13

2.4.2 Table 2 – X-ray crystallographic data collection and model refinement statistics

	TRAAK A198E K+ PDB 7LJ5		**TRAAK A198E Tl+** PDB 7LJA		**TRAAK A270P K+** PDB 7LJ4		**TRAAK G158D K+** PDB 7LJB	
Data Collection								
Beamline	ALS 8.3.1, APS 24-IDC, and APS 24-IDE		APS 24-IDC		APS 24-IDC		APS 24-IDC	
Wavelength (Å)	1.115820, 0.979100, 0.979180		0.9778		0.9791		0.9791	
Number of crystals	4		4		2		2	
Space group	$P2_1$		$P2_1$		$P2_1$		$P2_1$	
Cell dimensions								
a,b,c (Å)	80.16, 136.98, 95.74		80.23, 136.53, 95.28		80.280, 136.880, 95.580		80.144, 137.308, 96.298	
α=γ, β (°)	90, 94.472		90, 94.541		90, 94.243		90, 94.72	
Resolution (Å)	95.50-2.26 (2.50-2.26)*		47.49-2.78 (3.02-2.78)*		47.57-2.78 (3.09-2.78)*		48.03-2.97 (3.23-2.97)*	
Unique reflections	95738		51728		51681		42845	
Wilson B-factor	54.63		65.81		59.83		91.54	
	Anisotropic cutoff	Spherical cutoff	Anisotropic cutoff	Spherical cutoff	Anisotropic cutoff	Spherical cutoff	Anisotropic cutoff	Spherical cutoff
R_{merge}	0.246 (2.827)	0.3263 (12.75)	0.307 (3.288)	0.4317 (10.23)	0.277 (2.167)	0.3906 (8.413)	0.168 (2.023)	0.2065 (5.433)
R_{meas}	0.251 (2.884)	0.3325 (12.99)	0.318 (3.412)	0.4397 (10.41)	0.289 (2.254)	0.4065 (8.744)	0.176 (2.109)	0.2162 (5.693)
R_{pim}	0.049 (0.567)	0.06387 (2.46)	0.085 (0.908)	0.08328 (1.946)	0.079 (0.617)	0.1116 (2.374)	0.052 (0.597)	0.06342 (1.686)
$CC_{1/2}$	0.971 (0.578)	0.999 (0.134)	0.995 (0.581)	0.999 (0.176)	0.985 (0.554)	0.992 (0.131)	0.999 (.567)	0.999 (0.16)
I / σI	10.2 (1.5)	7.43 (0.20)	9.8 (1.3)	7.43 (0.22)	6.9 (1.3)	4.69 (0.18)	8.5 (1.2)	7.13 (0.36)
Completeness (%)	93.8 (75.4)	60.31 (4.26)	93.4 (66.5)	68.62 (7.48)	93.4 (69.0)	63.22 (4.09)	93.6 (64.2)	74.03 (8.25)
Multiplicity	27.2 (25.7)	27.5 (27.7)	27.7 (27.9)	27.8 (28.4)	13.2 (13.2)	13.2 (13.5)	11.6 (12.4)	11.5 (11.3)
Refinement								
No. of reflections used†	54920		33755		31089		30170	
R_{work} (%)	22.00		20.34		21.45		19.58	
R_{free} (%)	25.21		24.34		25.80		24.04	
No. of total atoms	10660		10651		10596		10586	
No. of protein residues	1351		1351		1351		1347	
No. of K+ / Tl+ ions	7		8		7		6	
Average B factor (Å2)	69.5		76.01		70.37		99.55	
Clashscore	6.39		9.63		8.52		6.8	
Molprobity score	1.84		1.89		2.03		1.79	
Ramachandran plot								
favored (%)	96.69		96.92		96.54		96.23	
allowed (%)	3.31		3.08		3.46		3.77	
disallowed (%)	0		0		0		0	
R.m.s. deviations								
Bond lengths (Å)	0.007		0.011		0.0088		0.0092	
Bond angles (°)	1.4061		1.5898		1.528		1.579	

*Values in parentheses are for the highest resolution shell.

5% of reflections were used to calculate Rfree

2.5 Data Availability

The X-ray crystallographic coordinates and structure factors for TRAAK$_{A198E}$ in K$^+$ (7LJ5), TRAAK$_{A198E}$ in Tl$^+$ (7LJA), TRAAK$_{A270P}$ in K$^+$ (7LJ4), and TRAAK$_{G158D}$ (7LJB) are available at the Protein Data Bank.

2.6 Author contributions

S.G.B., R.A.R., and B.S. conceived of the project, analyzed data, and wrote the manuscript. R.A.R. performed all aspects of the biochemistry and structural biology. B.S. performed all aspects of the electrophysiology. R.A.R. and B.S. generated constructs for recording. B.L. cultured the hybridoma for antibody purification. S.G.B. supervised the project and secured funding.

2.7 Acknowledgements

We thank R. MacKinnon for the 13E9 anti-human TRAAK hybridoma line. We thank staff at ALS beamline 8.3.1, especially J. Holton and G. Meigs, at APS beamline 24-IDC/E, especially I. Kourinov, for assistance at the synchrotron. We thank all members of the Brohawn laboratory for discussions. SGB is a New York Stem Cell Foundation-Robertson Neuroscience Investigator. This work was supported by the New York Stem Cell Foundation, NIGMS grant DP2GM123496, a McKnight Foundation Scholar Award, a Klingenstein-Simons Foundation Fellowship Award, a Sloan Research Fellowship, and a Rose Hill Innovator Award to SGB.

Chapter 3 The structural basis of pH gating in TASK2 K2P channels

3.1 Introduction

This chapter describes the first cryo-EM structure of a K2P family channel TASK2. The construct used for structural studies faithfully recapitulates wild-type pH sensitivity, and comparison of structures TASK2 structures solved at low and high pH reveal the structural basis extracellular pH gating at the selectivity filter and intracellular pH gating at the intracellular cavity mouth.

3.1.1 TASK2 physiology

TASK2 (TWIK-related acid sensitive K^+-channel 2) is a pH-gated member of the two-pore domain K^+ (K2P) channel family [1,77]. TASK2 is expressed widely, including in neurons, immune cells, chondrocytes, and epithelial cells of organs including the kidney and has been implicated in chemosensation, volume regulation, and ionic homeostasis [7,9,78–82]. TASK2 upregulation is associated with breast cancer proliferation, while its loss of function underlies Balkan endemic nephropathy [83,84]. Physiological roles of TASK2 have been related to its modulation by changes in intracellular and extracellular pH (pH_{int} and pH_{ext}) [8,78,85]. In neurons of the retrotrapezoid nucleus, TASK2 inhibition by extracellular and/or intracellular protons (as a proxy for blood [CO_2] [86]) depolarizes the cell, increases spike frequency, and leads to increased respiration [6–8]. In the kidney proximal tubule, TASK2 activation by extracellular alkalization that results from electrogenic bicarbonate secretion hyperpolarizes the cell to support further bicarbonate efflux [9,85].

3.1.2 pH gating in TASK2 channels

TASK2 is predominantly closed at pH 6.5 and is activated by intracellular and extracellular alkalization with a midpoint pH of 8.0-8.5 [36,77,78]. Mutational analyses have identified proton sensors on either side of the membrane: the extracellular residue R224 and intracellular residue K245 [86,87]. Gating by pH_{ext}, but not pH_{int}, is voltage- and $[K^+]_{ext}$-dependent, consistent with selectivity filter (or C-type) gating by external, but not internal, stimuli [77,86]. Still, the structural and mechanistic basis for gating of TASK2 is unknown and expected to be distinct from other K2P channels for which structures have been determined in detergent micelles [12,20,22,23,42,53].

3.2 Results

3.2.1 $TASK2_{AA335}$ has a canonical K2P channel architecture

Removing the predicted unstructured C-terminal region of *Mus musculus* TASK2 (resulting in $TASK2_{1-335}$) increased expression and biochemical stability of the purified channel for structural studies (Figs. 18-20). This construct retained the hallmark features of TASK2 when expressed in cells; activation by extracellular alkalization, intracellular alkalization, and intracellular PIP_2 (which requires an intact membrane proximal C-terminal region) was indistinguishable from full length TASK2 and comparable to previous reports (Fig. 21a-c, Fig. 20a-e) [36,77,86–88]. $TASK2_{1-335}$ was therefore used for structural studies.

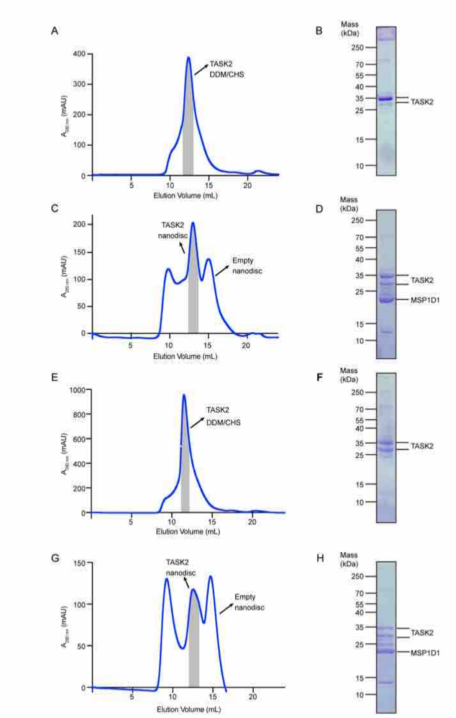

Figure 18 – Purification and reconstitution of TASK2.

(A-D) Data for assembly of TASK2-nanodisc samples at pH 8.5.

(A) Chromatogram from a Superdex 200 gel filtration of TASK2 purified in DDM/CHS.

(B) Coomassie-stained SDS-PAGE of pooled TASK2-containing fractions indicated by gray bar in (A).

(C) Chromatogram from Superdex 200 gel filtration of TASK2 reconstituted in MSP1D1 lipid nanodiscs.

(D) Coomassie-stained SDS-PAGE of final pooled TASK2-MSP1D1 nanodisc sample indicated by gray bar in (C). (E-H) Same as (A-D), but for samples at pH 6.5.

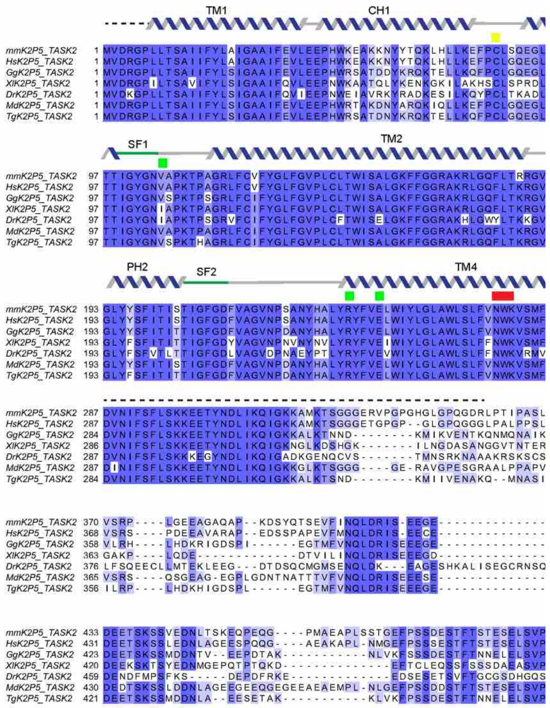

Figure 19 – Sequence alignment of TASK2 channels. Alignment of *M. musculus*, *H. sapiens, G. gallus, X. laevis, D. rerio, M. domestica, and T. guttata* TASK2 colored by conservation. TASK2 secondary structure is drawn above the sequences with gaps and unmodeled residues shown as dashed lines, loops and non-helical secondary structure as gray lines, and selectivity filters as green lines. Residues implicated in the extracellular gate are indicated with green boxes, residues implicated in the intracellular gate with red boxes, and disulfide bond forming C51 with a yellow box.

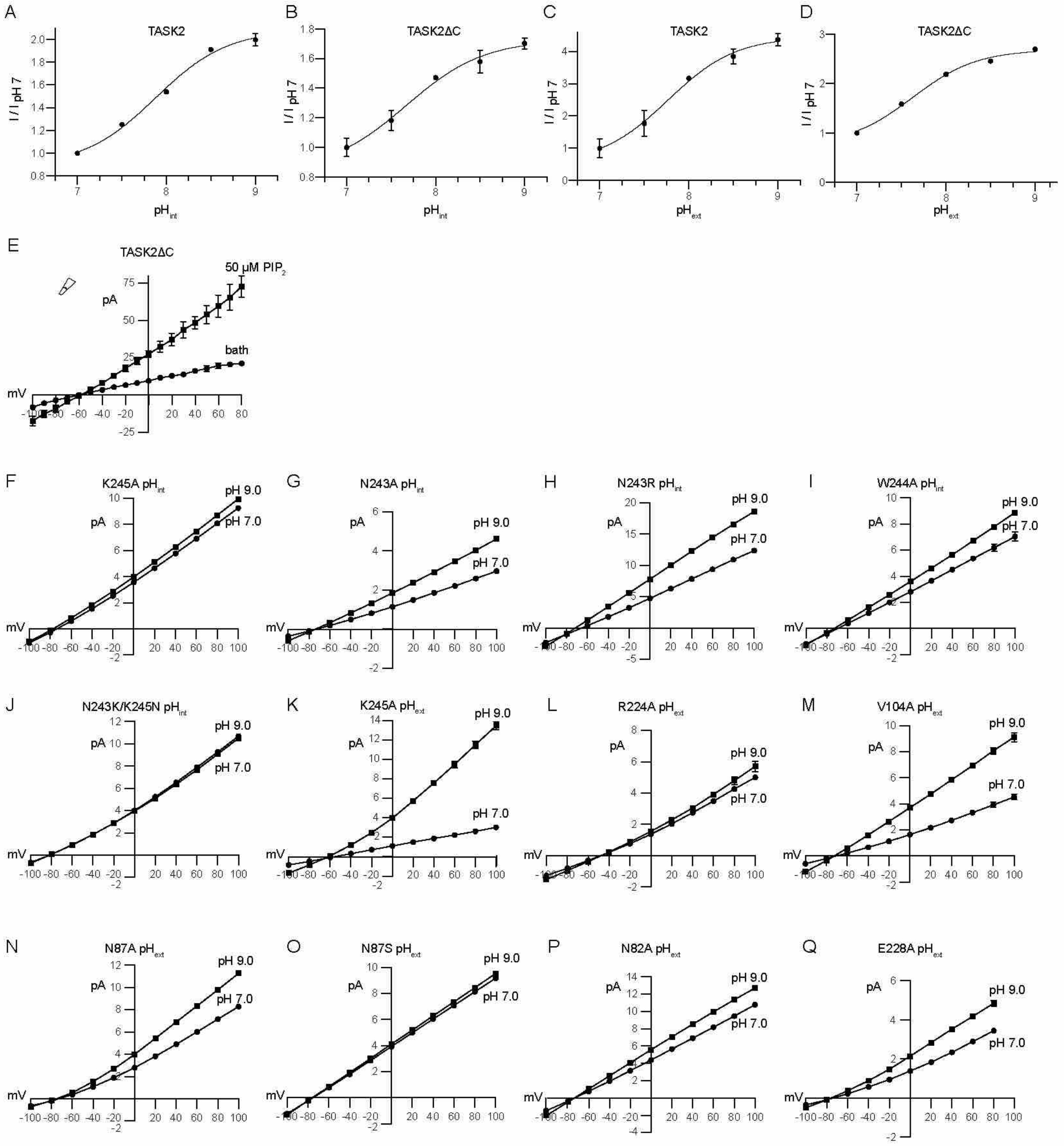

Figure 20 – pH and PIP$_2$ dependence of TASK2 and pH dependence of TASK2 mutant constructs.

(A,B) pH$_{int}$ and (C,D) pH$_{ext}$ dependence from a representative cell expressing (A.C) full length TASK2 and (B,D) the C-terminally truncated TASK2 construct used for structure determination. Normalized fold-activation of current by (A,B) alkaline pH$_{int}$ (pH$_{int}$ =9/pH$_{int}$ =7 at 0 mV) or (C,D) alkaline pH$_{ext}$ versus pH is plotted. Mean ± s.e.m. from three sweeps are plotted. Fits to Hill equations are drawn with $pK_{1/2}$=7.7, 7.9, 7.8, and 7.6 and Hill slope=1.0, 1.1, 1.1, and 1.2 for (A-D), respectively. Plots are shown with different scales.

(E) Current-voltage relationships from a representative inside-out patch from a TASK2-expressing cell before (circles) and after (squares) the addition of 50μM C8-PIP$_2$.

(F-J) Current-voltage relationships recorded from a representative cell expressing TASK2 mutants K245A, N243A, N243R, W244A, and N243K/K245N with pH$_{int}$=7 (circles) and pH$_{int}$=9. (squares). (K-Q) Current-voltage relationships recorded from a representative cell expressing TASK2 mutants K245A, R224A, V104A, N87A, N87S, N82A, and E228A with pH$_{ext}$=7 (circles) and pH$_{ext}$=9. (squares). Data in (E-Q) are mean currents ± s.e.m. from three consecutive sweeps at the indicated voltage.

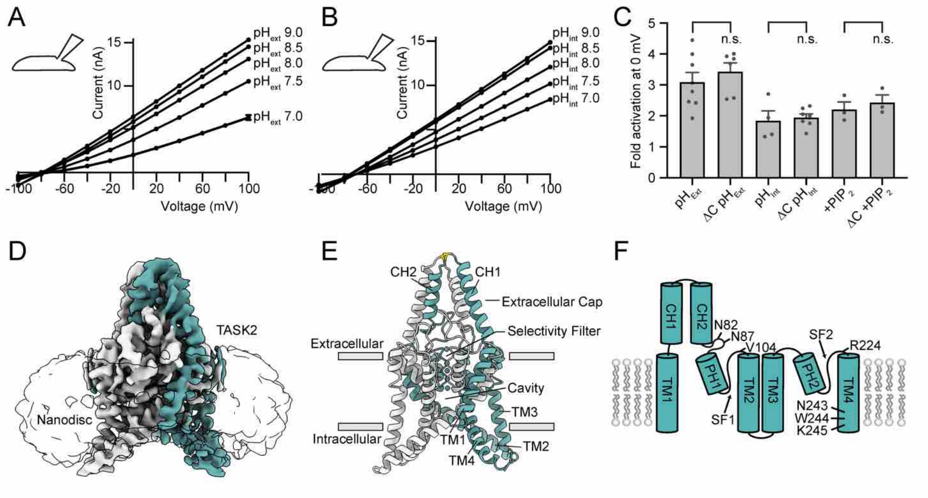

Figure 21 – Structure and function of TASK2.
Current-voltage relationships from a TASK2-expressing whole cell in response to varied (A) pH_{ext} and (B) pH_{int}. Currents in (A,B) are mean ± s.e.m. from three sweeps at each voltage.
(C) Normalized fold-activation of full length TASK2 (3.10±0.31) and TASK2ΔC (3.43±0.28) by $pH_{ext}=9/pH_{ext}=7$, of full length TASK2 (1.85±0.32) and TASK2ΔC (1.95±0.11) by $pH_{int}=9/pH_{int}=7$, and of full length TASK2 (2.21±0.24) and TASK2ΔC (2.43±0.24) by 50 μM di-C8 PIP_2. Mean ± s.e.m. are reported and plotted for n=8, 6, 4, 7, 3, and 3 cells from 2, 3, 2, 4, 2, and 3 independent transfections, respectively. Differences were assessed with unpaired two-tailed Student's t-test. P=0.45, 0.72, and 0.54 (P>0.05 not significant (n.s.)) for pH_{ext}, pH_{int}, and PIP_2, respectively.
(D) Cryo-EM map at pH 8.5 viewed from the membrane plane with density for nanodisc transparent and for TASK protomers teal and white.
(E) TASK2 structure at pH 8.5 colored as in (D) with K^+ ions teal and disulfide yellow.
(F) Cartoon representation of a TASK2 protomer with transmembrane helices (TM1-4), cap helices (CH1,2), pore helices (PH1,2), selectivity filters (SF1,2), and key residues discussed in the text indicated.

To determine the basis for channel gating in a lipid membrane-like environment, we reconstituted TASK2 into nanodiscs made from the scaffold protein MSP1D1 [89] and DOPE, POPC, and POPS lipids (Fig. 18) and determined its structure at pH 8.5 and 6.5. Unmasked reconstructions show well-defined density for TASK2 and the surrounding nanodisc (Fig. 21d). Cryo-EM maps were improved by partial signal subtraction of nanodisc density followed by further classification and refinement (Fig. 22-24). The channel is two-fold symmetric at high pH and asymmetric at low pH. While asymmetric and C2 symmetric reconstructions of TASK2 at pH 8.5 were essentially indistinguishable, enforcing C2 symmetry in reconstructions of TASK2 at pH 6.5 resulted in loss of density features, especially around the intracellular halves of transmembrane helices.

Amino acids 6-260 from each chain (58 kDa total) corresponding to the transmembrane and extracellular regions of the channel were de novo modeled into the final reconstructions at pH 8.5 and pH 6.5 (both at approximately 3.5 Å resolution) (Fig. 21d, e, Fig. 24, Table 3). Like other K2Ps, TASK2 is a domain swapped homodimer with each protomer chain containing four transmembrane spanning helices (TM1-TM4), two reentrant pore helices (PH1, PH2), two selectivity filters (SF1,SF2), and two extracellular cap forming helices (CH1, CH2) (Fig. 21f). The extracellular helical cap extends 35 Å above the mouth of the pore and is stabilized by an interchain disulfide bond at its apex. The distal intracellular C-terminal region was not resolved, suggesting it is conformationally heterogenous or unstructured as observed in previous K2P crystal structures [12,20,23,42].

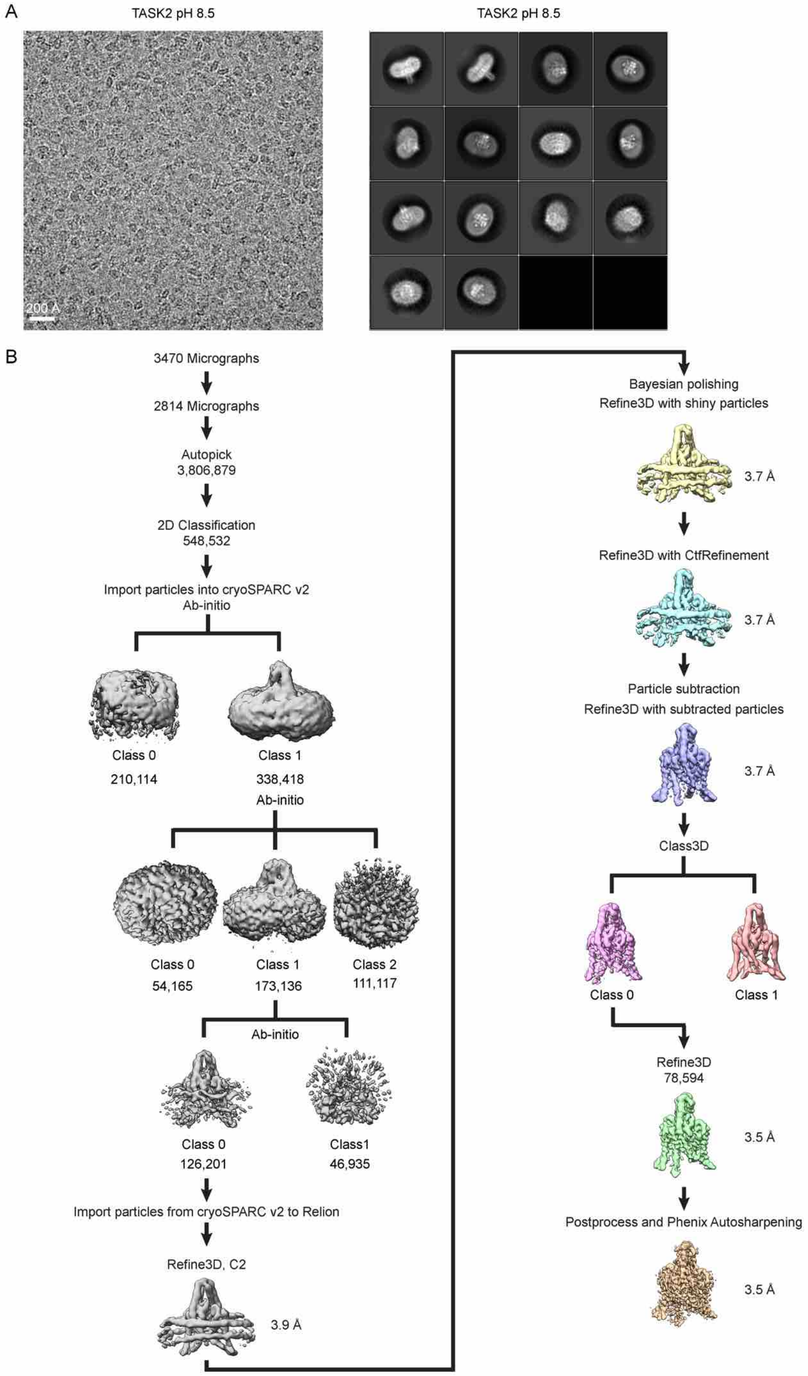

Figure 22 – Cryo-EM processing pipeline for TASK2 at pH 8.5.
(A) Example micrograph (left) and selected 2D class averages (right) of TASK2 in MSP1D1 lipid nanodiscs at pH 8.5. 2D classification was performed with an extracted box size of 200 pixels.
(B) cryo-EM data processing steps in Relion and cryoSPARC2. See Methods for details. Cryo-EM data were collected once. The micrograph in (A) is representative of the 2814 micrographs selected for analysis.

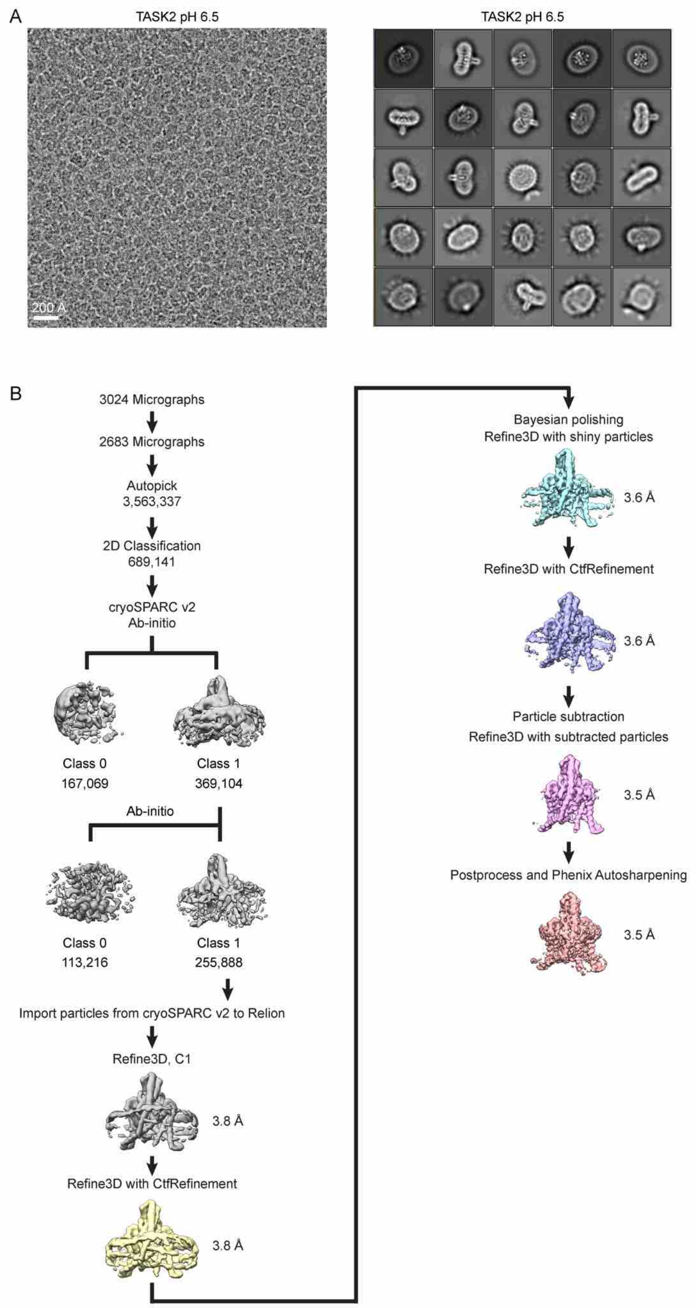

Figure 23 – Cryo-EM processing pipeline for TASK2 at pH 6.5.
(A) Example micrograph (left) and selected 2D class averages (right) of TASK2 in MSP1D1 lipid nanodiscs at pH 6.5. 2D classification was performed with an extracted box size of 160 pixels.
(B) cryo-EM data processing steps in Relion and cryoSPARC2. See Methods for details. Cryo-EM data were collected once. The micrograph in (A) is representative of the 2683 micrographs selected for analysis.

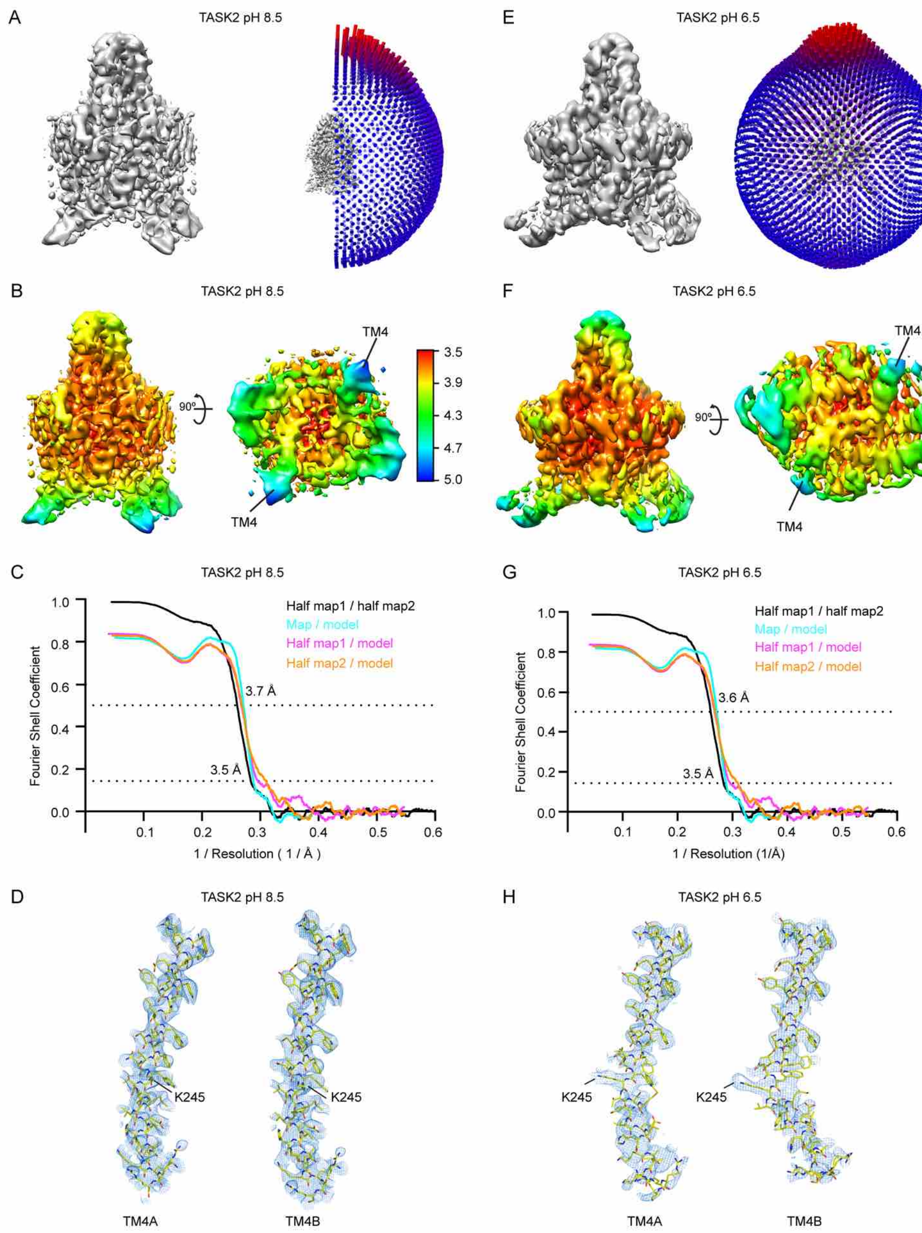

Figure 24 – Cryo-EM validation.

Data for TASK2-nanodisc samples at (A-D) pH 8.5 and (E-H) pH 6.5.
(A,E) Angular distribution of particles used in final refinement with final map for reference.
(B,F) Local resolution estimated in Relion colored as indicated on the final map. TM4s are indicated in a view from the cytoplasm.
(C,G) Fourier Shell Correlation (FSC) relationships between (black) the two unfiltered half-maps from refinement and used for calculating overall resolution at 0.143, (teal) final map versus model, (pink) half-map one versus model, and (orange) half-map two versus model.
(D,H) Cryo-EM density carved around TM4A and TM4B with the position of K245 indicated.

Comparison of the structures determined at different pH values reveals the channel adopts a predominantly nonconductive (closed) conformation at pH 6.5 and a predominantly conductive (open) conformation at pH 8.5 (Fig. 25a-c), consistent with functional data (Fig. 21a, b). Conformational changes in two regions gate TASK2 closed: an intracellular gate at the membrane-cytoplasm interface and an extracellular gate at the top of the selectivity filter. The bifurcated extracellular pathway connecting the top of the selectivity filter underneath the helical cap to the extracellular solution is similarly accessible to K⁺ in both structures (Fig. 26a-c).

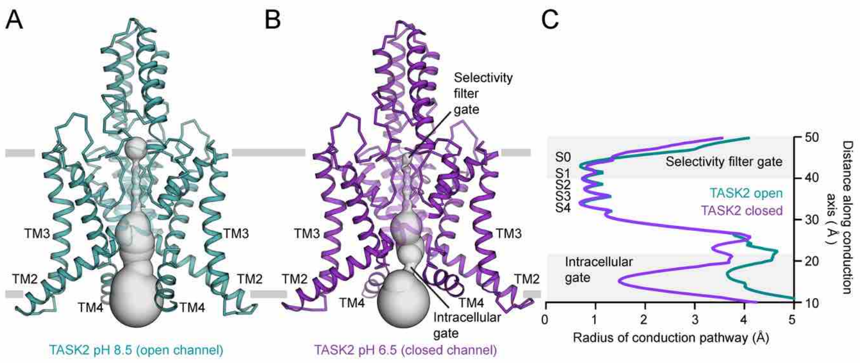

Figure 25 – Comparison of open and closed TASK2 structures captured in high and low pH. Structures of TASK2 determined at (A) pH 8.5 and (B) pH 6.5. The surface of the conduction pathway through the channel is shown in gray.
(C) Radius of the channel interior as a function of distance along the conduction pathway. Plot is drawn at the same scale as surfaces in (A,B). The positions of K⁺ coordination sites S0-S4, the extracellular selectivity filter gate, and the intracellular gate at the membrane-cytoplasm interface are indicated.

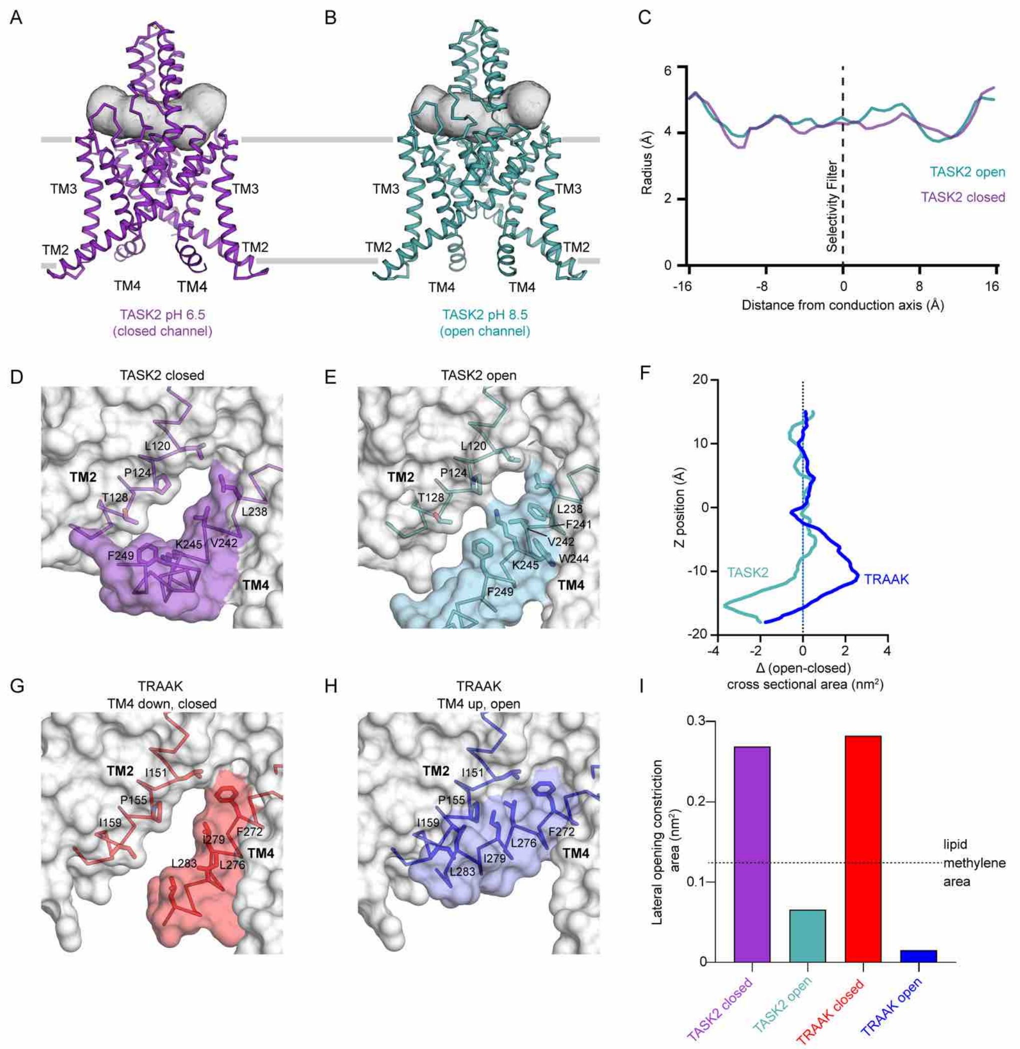

Figure 26 – Extracellular ion pathways and lateral membrane openings in TASK2.
(A,B) Structures of TASK2 determined at (A) pH 8.5 and (B) pH 6.5. The surface of a bifurcated extracellular pathway from the top of the selectivity filter underneath the helical cap to the extracellular solution on either side is shown in gray.
(C) Radius of the extracellular pathway as a function of distance from the conduction axis. The path is similarly accessible to K^+ ions in both structures.
(D,E) View from the membrane plane of the cytoplasmic sides of TASK2 TM4 and TM2 from (D) low pH (closed) (E) high pH (open) structures. Protein surface is shown half transparent.
(F) Change in channel cross sectional area upon opening as a function of membrane depth for TASK2 and TRAAK. TRAAK expands within the membrane upon opening while TASK2 constricts near the membrane-cytoplasm interface.
(G,H) View from the membrane plane of the cytoplasmic sides of TRAAK TM4 and TM2 from (G) nonconductive (closed) and (H) conductive (open) structures.
(I) Minimum cross-sectional areas of membrane-facing lateral openings in TASK2 closed, and TASK2 open, TRAAK closed, and TRAAK open structures. Cross-sectional areas for each structure correspond to the narrowest 1 Å segment of a path connecting the channel cavity and membrane bilayer calculated using a spherical probe. The cross-sectional area of a lipid acyl chain methylene is drawn with a dashed line for comparison. An acyl chain could access the cavity of TASK2 and TRAAK channels in closed, but not open, conformations.

3.2.2 The intracellular pH gate in TASK2 channels

At pH 8.5, a wide channel cavity lined by TM2, TM3, and TM4 from each protomer creates an unobstructed path for ion conduction from the intracellular solution to the base of the K^+ selectivity filter (Fig. 25a, c). Its narrowest constriction has a radius of 3.5 Å, which is wide enough to accommodate hydrated K^+ ions (Fig. 25c). At pH 6.5, rearrangements of TM4 from each subunit creates a tight constriction near the cytoplasm-membrane interface (Fig. 25b, c). The constriction narrows to a radius of 1.2 Å, too small to allow passage of even partially dehydrated K^+ ions, gating the channel closed (Fig. 25c). We note that the local resolution of the cryo-EM map in this region is lower than the map average (Fig. 24b, f). While the model fits well to the density, particularly in the peptide backbone, the positions of side chains are less well determined than in the rest of the channel (Fig. 24d, h). This may be due to modest conformational heterogeneity between particles in this region of TM4, though we were not able to classify discrete conformations.

The conformational changes in TM4 are centered around an internal proton sensor at K245 and primarily involve residues 243-246 (Fig. 27). At pH 8.5, TM4 is helical with K245 positioned on its top face. The rotameric position of K245 is sterically restricted by F241, W244, and F249 and projects upward towards the hydrophobic bottom face of TM2 from the neighboring protomer around P124 (Fig. 27b, d, Fig. 26e). In this position, K245 forms part of the wall of the channel cavity with its methylenes facing the lipid bilayer. The K245 ε-amino group is likely deprotonated in this conformation, indicating a reduced pK_a relative to a fully solvent exposed lysine as a consequence of its hydrophobic environment. Similar pK_a shifts have been measured in model systems containing buried lysine residues [90]. At pH 6.5, the TM4 helix is broken and kinked at W244 such that the side chain of K245 rotates ~90º towards the conduction axis (Fig. 27c-f, Fig. 26d). In this conformation, K245 projects towards N243 of the diagonally opposed subunit to form a cytoplasmic seal (Fig. 27c). In both conformations, K245 is partially exposed to the internal solution and poised to respond to pH changes in the cytoplasm to gate the channel (Fig. 27b,c, Fig. 26d,e).

We evaluated the pH sensitivity of TASK2 mutants to test the structural model for gating by pH_{int} (Fig. 27g). Wild-type TASK2 is activated ~2-fold by a shift in pH_{int} from 7 to 9. Consistent with previous reports and its role as a proton sensor [86], K245A eliminates pH_{int} sensitivity (Fig. 27g). We reasoned that the size of the N243 side chain was most important for sealing the cavity with K245. Indeed, a smaller side chain in N243A impairs pH_{int} activation (by ~70%), while a larger side chain in N243R has no significant effect despite its positive charge (Fig. 27g). W244A results in a more subtle loss of pH_{int} activation (by ~47%), which is likely due to increased flexibility of TM4 upon loss of anchoring interactions between W244 and TM3 (Fig. 27b,c, Fig. 26d,e). While K245 is able to rotate from a hydrophobic pocket at high pH towards the conduction axis at low pH, N243 remains relatively stationary in closed and open structures (Fig. 27f). We reasoned that pH_{int} activation should therefore be sensitive to the unique position of the K245 sensor. Consistently, a simple swap of these two residues in the double mutant N243K/K245N does not rescue pH_{int} activation (Fig. 27g). We conclude movement of opposed K245 residues and proximal helical regions upon protonation forms a protein seal between TM4s to gate the channel closed in response to intracellular acidification.

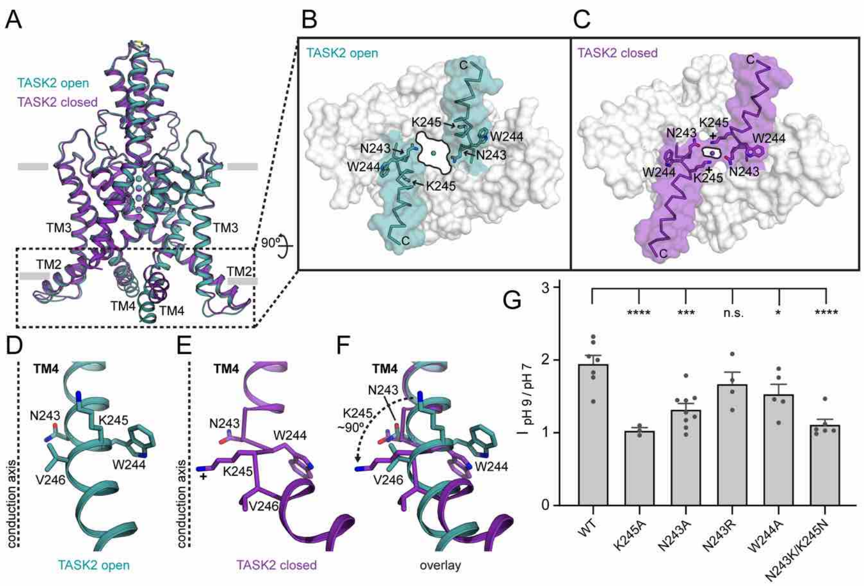

Figure 27 – A TASK2 intracellular gate controlled by pH$_{\text{int}}$.
(A) Overlay of closed and open conformations of TASK2 viewed from the membrane plane highlighting conformational changes in the cytoplasmic end of TM4.
(B,C) Surface representation of the region boxed in (A) viewed from the cytoplasmic side for (B) open and (C) closed channels. Residues involved in gating and the positive charge on K245 at low pH are indicated.
(D-F) View from the membrane plane of one TM4 and intracellular gating residues from (D) open, (E) closed, and (F) and both structures overlaid. In (D) and (E), a dashed line is drawn at the center of the K$^+$ conduction axis for reference.
(G) Normalized fold-activation of current by alkaline pH$_{\text{int}}$ (pH$_{\text{int}}$=9/pH$_{\text{int}}$=7 at 0 mV) for wildtype TASK2 (1.95±0.11) and mutants K245A (1.03±0.04), N243A (1.32±0.08), N243R (1.67±0.16), W244A (1.53±0.13), and N243K/K245N (1.11±0.07). Mean ± s.e.m. are reported and plotted for n=7, 3, 9, 4, 5, 6 cells from 4, 2, 5, 3, 2, and 2 independent transfections, respectively. Differences were assessed with a one-way ANOVA with Dunnett correction for multiple comparisons. P<0.0001(****) for K245A and N243K/K245N. P=0.0002(***), 0.04(*), and 0.34 (n.s., not significant) for N243A, W244A, and N243R, respectively.

3.2.3 The extracellular pH gate in TASK2 channels

A second gate was identified on the extracellular face of the TASK2 selectivity filter. At pH 8.5, the filter adopts a canonical approximate four-fold symmetric conformation with strong density corresponding to four K$^+$ ions in the filter (sites S1-S4) and one above the pore (S0) (Fig. 28a-e). At pH 6.5, the selectivity filter is dramatically rearranged, resulting in a loss of the symmetric K$^+$-coordination environment, expansion of the S1 site by 0.6 Å, and a constriction of the S0 site by 1.9 Å (Fig. 28b-d, Fig. 25c). Such a rearrangement in the chemical and geometrical aspects of the K$^+$ coordination environment would be expected to alter ion dehydration and binding at these sites. Indeed, comparison of the maps shows a clear loss of density for bound K^+ around S0 and S1 at low pH (Fig. 28e, f).

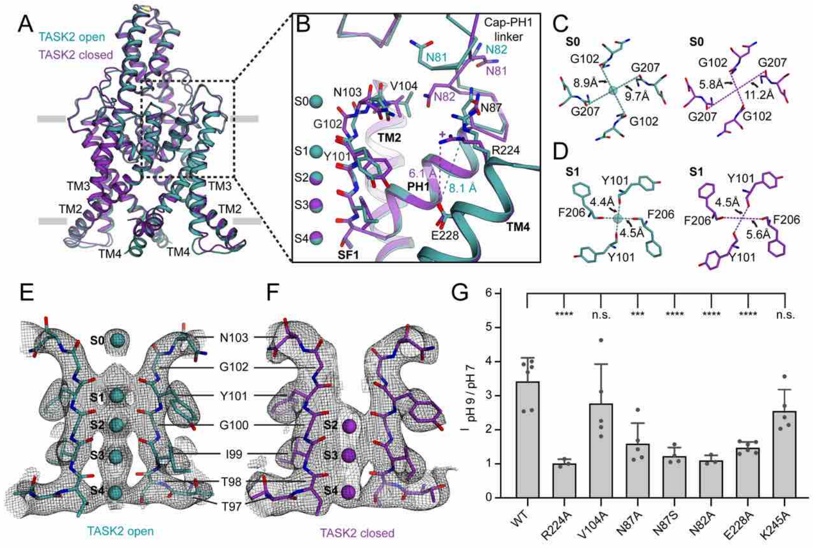

Figure 28 – A TASK2 selectivity filter gate controlled by pH_{ext}.

(A) Overlay of closed and open conformations of TASK2 viewed from the membrane plane highlighting conformational changes in the extracellular side of the selectivity filter.

(B) View of the region boxed in (A). Residues involved in gating and the positive charge on R224 at low pH are indicated.

(C,D) Inter-carbonyl distances at K^+-binding sites (C) S0 and (D) S1 in open and closed structures viewed from the extracellular side.

(E,F) Comparison of ion occupancy in the selectivity filter of cryo-EM maps from (E) open TASK2 and (F) closed TASK2.

(G) Normalized fold-activation of current by alkaline pH_{ext} (pH_{ext}=9/pH_{ext}=7 at 0 mV) for wild-type TASK2 (3.43±0.28 (n=6)) and mutants R224A (1.02±0.07 (n=3)), V104A (2.78±0.51 (n=5)), N87A (1.60±0.27 (n=5)), N87S (1.24±0.12 (n=4)), N82A (1.11±0.08 (n=3)), E228A (1.48±0.07 (n=6)), and K245 (2.56±0.28 (n=5)). Mean ± s.e.m. are reported and plotted for n=6, 3, 5, 5, 4, 3, 6, and 5 cells from 3, 1, 2, 2, 2, 1, 2, and 2 independent transfections, respectively. Differences were assessed with a one-way ANOVA with Dunnett correction for multiple comparisons. $P<0.0001$(****) for N82A, N87S, R224A, and E228A. $P=0.0002$(***), 0.14, and 0.39 (n.s., not significant) for N87A, K245A, and V104A, respectively.

The conformational changes are asymmetric; pseudo four-fold symmetry in the open channel becomes approximate two-fold symmetry in the closed state. At S1, Y101 of SF1 and F206 of SF2 move away from the conduction axis by an average of 1.0 Å and 0.9 Å, respectively (Fig. 28d, Fig. 29a-f). This increases distances between diagonally opposed carbonyls in the filter: from 4.4 Å and 4.5 Å in the open channel to 4.5 Å and 5.6 Å in the closed channel between SF1s and SF2s (Fig. 28d). At S0, G102 of SF1 moves towards the conduction axis by an average of 1.7 Å and G207 of SF2 moves away by an average of 0.9 Å (Fig. 28b, Fig. 29a-f). This markedly decreases the distance between diagonally opposed carbonyls in SF1s, from 8.9 Å in the open channel to 5.8 Å in the closed channel, and increases the distance between diagonally opposed carbonyls at SF2, from 9.7 Å in the open channel to 11.2 Å in the closed channel (Fig. 28c).

How do extracellular protons result in conformational changes at the selectivity filter that render the channel nonconductive? At pH 8.5, the proton sensor R224 rests above TM4 with its side chain directed towards the extracellular solution (Fig. 28b). Protonation of R224 results in its movement down towards the membrane approximately 2 Å closer to the largely buried E228 on TM4. Long-range electrostatic interactions between R224 and E228 in the relatively low dielectric environment may stabilize this movement of R224 (Fig. 28b). The cap-PH1 linker undergoes a series of coordinated rearrangements; the side chain of N87 moves towards the membrane with R224 and rotation of the peptide backbone between F80 and W83 repositions N82 between R224 and V104 at the top of SF1 (Fig. 28b). Wedging N82 into this position displaces SF1 and the subsequent linker to TM2 (from G102 to A105) towards SF2 (Fig. 28b). This results in movement of carbonyls at Y101 and G102 in SF1 and, to accommodate this shift, F206 in SF2. The consequence is disruption of the K^+ coordination environment at S0 and S1 to disfavor ion binding and conduction (Fig. 28b-f).

We evaluated the pH sensitivity of TASK2 mutants to test the structural model for gating by pH_{ext} (Fig. 28g). Wild-type TASK2 is activated ~3.4-fold by a shift in pH_{ext} from 7.0 to 9.0 (Fig. 28g). Consistent with previous reports and its role as a proton sensor [86,87], R224A mutation eliminates pH_{ext} activation (Fig. 28g). As predicted from the structure, mutation of V104A does not significantly reduce activation (Fig. 28g): in spite of a smaller side chain at V104A, N82 movement would still require displacement of SF1. In contrast, mutation of both key asparagines significantly compromises pH_{ext} activation: N87A, N87S, and N82A reduce activation by an average of 75%, 91%, and 95%, respectively (Fig. 28g). Consistent with a role for E228 in stabilizing a protonated R224, elimination of the negative charge in an E228A mutation reduces activation by 80%. We conclude that movement of R224 upon protonation is relayed through N87 and N82 to displace SF1 and disrupt K^+ coordination at S1 and S0 to gate the channel closed in response to extracellular acidification.

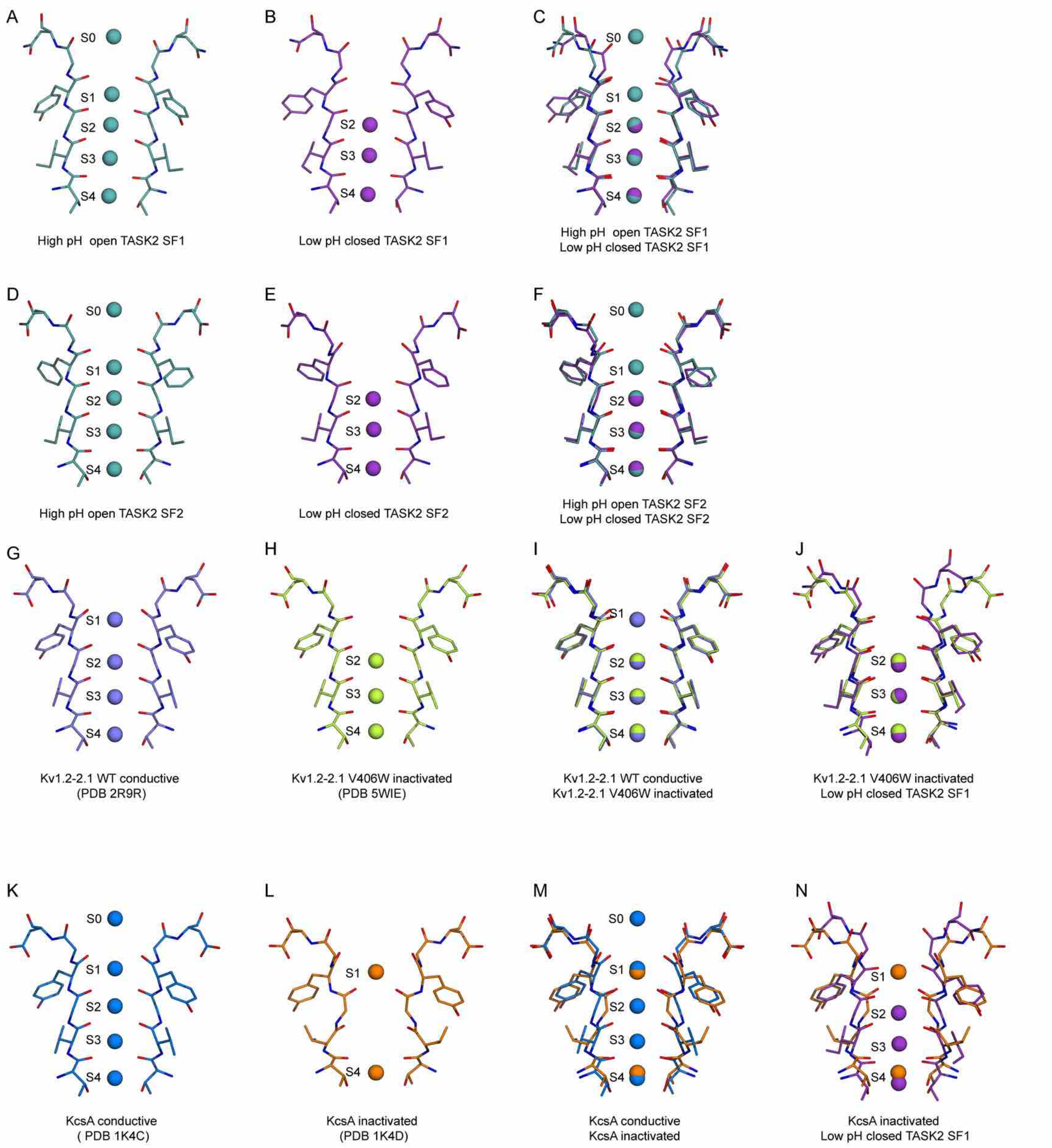

High pH open TASK2 SF1

Low pH closed TASK2 SF1

High pH open TASK2 SF1
Low pH closed TASK2 SF1

High pH open TASK2 SF2

Low pH closed TASK2 SF2

High pH open TASK2 SF2
Low pH closed TASK2 SF2

Kv1.2-2.1 WT conductive
(PDB 2R9R)

Kv1.2-2.1 V406W inactivated
(PDB 5WIE)

Kv1.2-2.1 WT conductive
Kv1.2-2.1 V406W inactivated

Kv1.2-2.1 V406W inactivated
Low pH closed TASK2 SF1

KcsA conductive
(PDB 1K4C)

KcsA inactivated
(PDB 1K4D)

KcsA conductive
KcsA inactivated

KcsA inactivated
Low pH closed TASK2 SF1

Figure 29 – Comparison of selectivity filters and selectivity filter gates in TASK2 and other K⁺ channels.

(A-N) Two opposing selectivity filter regions and positions of bound K⁺ ions from structures of the channels indicated: (A) open TASK2 SF1, (B) closed TASK2 SF1, (C) overlaid open and closed TASK2 SF1s, (D) open TASK2 SF2, (E) closed TASK2 SF2, (F) overlaid open and closed TASK2 SF2s, (G) open Kv1.1-2.1, (H) inactivated Kv1.1-2.1 mutant V406W, (I) overlaid open and inactivated Kv1.1-2.1 mutant V406W, (J) overlaid inactivated Kv1.1-2.1 and closed TASK2 SF1, (K) open KcsA, (L) low K⁺ inactivated KcsA, (N) overlaid open and inactivated KcsA, and (N) overlaid inactivated KcsA and closed TASK2 SF1.

3.2.4 Models of pH_{int} and pH_{ext} gating in TASK2

Our data support a model for TASK2 regulation through two gates controlled by intracellular and extracellular pH (Fig. 30). Mutation of the intracellular proton sensor K245A does not significantly change pH_{ext} activation (Fig. 28g), consistent with previous reports and supporting the notion of independent function of the two gates, though further work is needed to show this definitively [86].

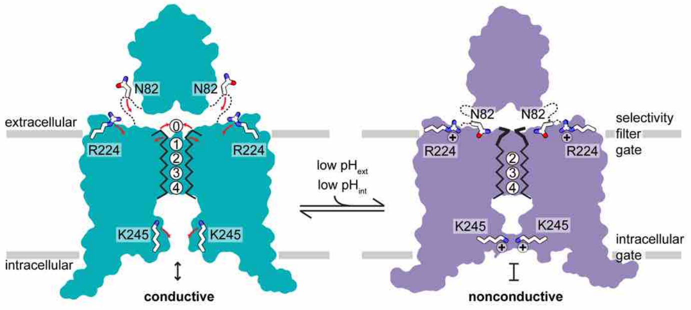

Figure 30 – Structural model for pH gating of the TASK2 channel.
At high pH, TASK2 is conductive. An unobstructed path for K^+ exists from the cytoplasmic to extracellular solution through the channel cavity and selectivity filter with four internal and one extracellular K^+ coordination sites. At low pH, TASK2 is nonconductive. Protonation of K245 and conformational changes in TM4 create a protein seal at the inner gate. Protonation of R224 and conformational changes relayed to the K^+ sites S0 and S1 sites disfavor K^+ coordination at the selectivity filter gate.

Both gates are unique among known channel structures. The intracellular gate is formed at a position similar to the canonical inner-helix bundle crossing in four-fold symmetric K^+ channels like KcsA or K_Vs [91,92], but is formed by different molecular rearrangements. Instead of association of four inner helices, intracellular gating of TASK2 involves juxtaposition of two diagonally opposed TM4s (Figs. 27b,c, Fig. 31a-f). Interestingly, the K2P TASK1 (which belongs to a different K2P clade from TASK2 (Fig. 1)) has an inner gate at the membrane-cytoplasm interface, but it is formed differently through crossover of TM4s and hydrophobic packing (Fig. 31e,g) [22]. This difference in inner gating, and the fact that TASK1 lacks a proton sensor analogous to the conserved K245 in TASK2 provides a mechanistic explanation for the independence of TASK1 on pH_{int}.

While functional evidence of selectivity filter gating in many K^+ channels, including K2Ps, has been long documented, its structural basis is controversial [77,86,93–97]. Structural evidence exists for two modes of filter inactivation: loss of S1 due to constriction of coordinating carbonyls (from an inactivation-enhancing point mutant in K_V1.2-2.1) and loss of S2 and S3 due to filter backbone rotation (from an inactivation-enhancing point mutant in KcsA) (Fig. 29g-n) [98,99]. A recently posted report describing structures of the K2P TREK1 in low [K^+] suggests a third mode involving loss of S1 and S2 [53]. We demonstrate TASK2 utilizes a new mode of filter gating in response to physiological stimuli: asymmetric disruption of S0 by constriction and S1 by dilation of coordinating carbonyls and displacement of the selectivity filter. It is likely still other filter rearrangements have arisen in other K$^+$ channels. TASK1 activation by extracellular alkalization is thought to occur through the selectivity filter [1], but its proton sensor is in a different position (a histidine in SF1 at the position of N103 in TASK2) and it lacks residues for the conformational relay (R224, E228, and N87) that are strictly conserved in TASK2 across species (Fig. 19).

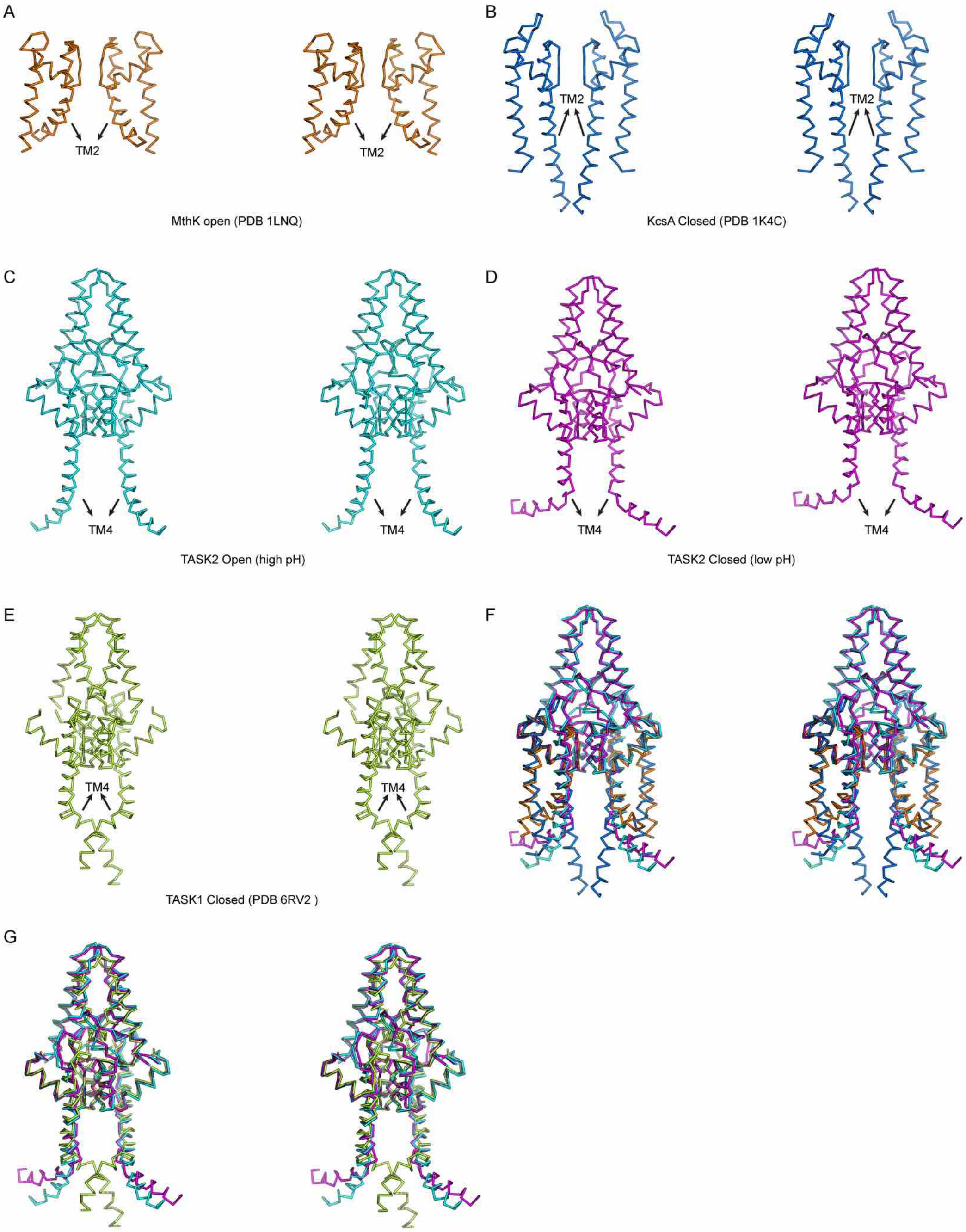

Figure 31 – Comparison of inner gates in TASK2 and other K+ channels.
(A-G) Stereo views from the membrane plane highlighting inner gate regions of selected K+ channels: (A) open MthK, (B) closed KcsA, (C) open TASK2, (D) closed TASK2, and (E) closed TASK1. (F) An overlay of the TASK2 open and closed structures with the canonical "bundle crossing" inner gating channels KcsA and MthK, colored as in (A-D). (G) An overlay of the TASK2 open and closed structures with TASK1, with a distinct inner "X" gate, colored as in (C-E).

3.2.5 Closed TASK2 channels have lateral openings but do not change cross-sectional area upon opening

K2P channels are regulated by a diverse array of chemical and physical cues through correspondingly diverse mechanisms [1,2]. Gating open the mechanosensitive K2Ps TRAAK, TREK1, and TREK2 involves movement of TM4 "up" towards the extracellular side, sealing membrane-facing lateral openings and preventing lipid access to the cavity that can block conduction (Fig. 26g-i) [42,100]. Mechanosensation results because movement of TM4 up expands the cross-sectional area of the channel and increasing membrane tension energetically favors expansion. Notably, TASK2 at low pH also has wide membrane-facing lateral openings between TM2 and TM4 (Fig. 26d, e, i). Lipid-like density is also observed in these openings projecting towards the channel cavity, but it is insufficiently resolved to model. TASK2 opening at high pH seals the lateral membrane openings primarily through repositioning of K245. Unlike movement of TM4 up in TRAAK and TREKs, this does not expand the cross-sectional area of TASK2 (Fig. 26f). This offers a physical explanation for insensitivity of TASK2 to mechanical force: without an area increase upon opening, there is no energetic drive for tension to promote opening. Restriction of TM4 movement might similarly preclude mechanical activation in other K2Ps.

3.3 Materials and Methods

3.3.1 TASK2 Cloning, Expression, and Purification

Cloning, expression, and purification were performed similarly to that described for the K2P channel TRAAK [4]. A gene encoding *Mus musculus* TASK2 (Uniprot Q9JK62) was codon-optimized for expression in *Pichia pastoris*, synthesized (Genewiz, Inc), and cloned into a modified pPICZ-B vector (Life Technologies Inc). The resulting construct encoded a human rhinovirus 3C protease-cleavable C-terminal EGFP-10x histidine fusion protein. A truncation of the C-terminal 167 amino acids, which are predicted to be largely unstructured, was found to improve protein expression and biochemical stability. The resulting construct, $\text{TASK2}_{\text{(aa1-335)-SNS-LEVLFQ/GP-(EGFP)-HHHHHHHHHH}}$ was used for structural studies and is referred to as TASK2 in the text for simplicity.

Pme1 linearized pPICZ-B plasmid was transformed into *Pichia pastoris* strain SMD1163 by electroporation and transformants were selected on YPDS plates with 0.5 mg/mL Zeocin. Expression levels of individual transformants were analyzed by FSEC. Large-scale expression from a suitable transformant was performed in MiniFors 2 3-liter fermenter. Overnight cultures of cells in YPD + 0.5 mg/mL Zeocin were added to minimal media to a starting OD_{600} ~1 and grown at 30°C with glycerol feeding for 48 hours at 40% O_2 saturation and pH 5.0 maintained with variable stir speed, air/O_2 gas mixture, gas flow rate, and NH_4OH addition. Cells were then starved to deplete glycerol, temperature was reduced to 27°C, and protein expression was induced by a gradually increasing methanol feed rate. Expression continued for ~48-60 hours.

Cells were pelleted, flash-frozen in liquid nitrogen, and stored at -80°C. 30 g of cells were broken by milling (Retsch model MM301) for 5 cycles of 3 minutes at 25 Hz. All subsequent purification steps were carried out at 4°C. Cell powder was added to 100 mL lysis buffer containing 50 mM Tris pH 8.5 (unless otherwise noted, pH values for Tris buffers correspond to values at 4°C) , 150 mM KCl, 1 mM phenylmethysulfonyl fluoride, 1 mM EDTA, 10ul Benzonase Nuclease (EMD Milipore), 1 mM E64, 1 mg/ml Pepstatin A, 10 mg/ml Soy Trypsin Inhibitor, 1 mM Benzimidine, 1 mg/ml Aprotinin, 1 mg/ml Leupeptin. The solution was sonicated and centrifuged at 150,000 x g for 45 minutes. The supernatant was discarded and the membrane pellet was transferred into a dounce homogenizer containing extraction Buffer (50 mM Tris pH 8.5, 150 mM KCl, 1mM phenylmethysulfonyl fluoride, 1 mM EDTA, 10 µl Benzonase Nuclease (EMD milipore), 1 µM AEBSF, 1 mM E64, 1mg/ml Pepstatin A, 10 mg/ml Soy Trypsin Inhibitor, 1 mM Benzimidine, 1 mg/ml Aprotinin, 1 mg/ml Leupeptin, 1% n-Dodecyl-b-D-Maltopyranoside (DDM, Anatrace, Maumee, OH), 0.2% Cholesterol Hemisuccinate Tris Salt (CHS, Anatrace)). Membrane pellets were homogenized in 100 mL buffer and then gently stirred at 4°C for 2 hours. The extraction was centrifuged at 33,000 x g for 45 minutes. 5 ml Sepharose resin coupled to anti-GFP nanobody was added to the supernatant and stirred gently for 2 hours at 4°C. The resin was collected in a column and washed with 50 mL Buffer 1 (20 mM Tris, 150 mM KCl, 1 mM EDTA, 1% DDM, 0.2% CHS, pH 8.5), 150 mL Buffer 2 (20 mM Tris, 300 mM KCl, 1 mM EDTA, 1% DDM, 0.2% CHS, pH 8.5), and 20 mL of Buffer 1. PPX (~0.5 mg) was added into the washed resin in 5 mL Buffer 1 and rocked gently overnight. Cleaved TASK2 was eluted and concentrated to ~0.4 mL with an Amicon Ultra spin concentrator (50 kDa cutoff, MilliporeSigma, USA). The concentrated protein was subjected to size exclusion chromatography using a Superdex 200 Increase 10/300 column (GE Healthcare, Chicago, IL) run in Buffer 3 (20 mM Tris pH 8.5, 150 mM KCl, 1 mM EDTA, 1% DDM, 0.01% CHS) on a NGC system (Bio-Rad, Hercules, CA) with ChromLab 6. The peak fractions were collected and spin concentrated for reconstitution.

3.3.2 Nanodisc assembly

Freshly purified TASK2 was reconstituted into MSP1D1 nanodiscs with a 2:1:1 DOPE:POPS:POPC lipid mixture (mol:mol, Avanti, Alabaster, Alabama) at a final molar ratio of TASK2:MSP1D1:lipid of 1:5:250. Lipids in chloroform were mixed, dried under argon, washed with pentane, dried under argon, and dried under vacuum overnight in the dark. Dried lipids were rehydrated in buffer containing 20 mM Tris, 150 mM KCl, 1 mM EDTA, pH 8.5 and clarified by bath sonication. DDM was added to a final concentration of 8 mM. TASK2 was mixed with lipids and incubated at 4°C for 30 minutes before addition MSP1D1 protein. After incubation for 10 minutes at 4°C, 100 mg of Biobeads SM2 (Bio-Rad, USA) (prepared by sequential washing in methanol, water, and Buffer 4 and weighed damp following bulk liquid removal) was added and the mixture was rotated at 4°C overnight. The sample was spun down to facilitate removal of solution from the Biobeads and the reconstituted channel was further purified on a Superdex 200 increase column run in 20 mM Tris pH 8.5, 150 mM KCl, and 1 mM EDTA (high pH) or 20 mM potassium phosphate pH 6.5, 150 mM KCl, and 1 mM EDTA (low pH). The peak fractions were collected and spin concentrated (50 kDa MWCO) to 1.0-1.2 mg/ml for grid preparation

3.3.3 Grid preparation

The TASK2-nanodisc sample was centrifuged at 21,000 x g for 10 min at 4°C. A 3 µL sample was applied to holey carbon, 300 mesh R1.2/1.3 gold grids (Quantifoil, Großlöbichau, Germany) that were freshly glow discharged for 30 seconds. Sample was incubated for 5 seconds at 4°C and 100% humidity prior to blotting with Whatman #1 filter paper for 3-3.5 seconds at blot force 1 and plunge-freezing in liquid ethane cooled by liquid nitrogen using a FEI Mark IV Vitrobot (FEI / Thermo Scientific, USA).

3.3.4 Cryo-EM data acquisition

Grids were clipped and transferred to a FEI Talos Arctica electron microscope operated at 200 kV. Fifty frame movies were recorded on a Gatan K3 Summit direct electron detector in super-resolution counting mode with pixel size of 0.5685 Å. The electron dose was 9.170 e^- $Å^2$ s^{-1} and 8.974 e^- $Å^2$ s^- and total dose was 50.4625 e^- $Å^2$ and 50.325 e^- $Å^2$ in pH 8.5 and pH 6.5 datasets, respectively. Nine movies were collected around a central hole position with image shift and defocus was varied from −0.8 to −2.0 µm through SerialEM 3.6 [101]. See Table 1 for data collection statistics.

3.3.5 Cryo-EM data processing

For TASK2 in nanodiscs at pH 8.5, 3470 micrographs were corrected for beam-induced drift using MotionCor2 [102,103] in Relion 3.0 and Reline 3.1-beta [104] and the data was binned to 1.137 A/pixel. The contrast transfer function (CTF) parameters for each micrograph were determined using CTFFIND-4.1 . For particle picking, 1000 particles were picked manually and subjected to reference-free 2D classification in RELION 3.0 to generate reference for autopicking. After initial cleanup through rounds of 2D classification in Relion 3.0 or Relion 3.1-beta, the remaining particles were extracted and imported into Cryosparc . After additional 2D classification in Cryosparc, the particles that had clearly defined and recognizable features were combined for further analysis. CryoSPARC was used to generate an ab initio model with 2 classes and 0 similarity with or without symmetry. Particles belonging to a class with well-defined features were further refined using Heterogeneous refinement and Non-uniform (NU) refinement.

Particle positions and angles from the final cryoSPARC2 refinement job were input into Relion 3.0 or Relion 3.1 beta (using csparc2relion.py from the UCSF PyEM) and 3D refined to generate a 3.92 Å map with C2 symmetry (6 Å low-pass filter, 0.9 degrees initial sampling, 0.9 degrees local searches). Further 3D refinement following Bayesian particle polishing improved the map to 3.73 Å. The following CTF refinement with beam tilt group estimation and per-particle defocus was performed, although subsequent 3D refinement did not markedly improve the map. To further improve the resolution, we performed the particle subtraction to remove the contribution of the nanodisc density and subsequent 3D refinement yielded a map at 3.5 Å and used for model building.

For TASK2 in nanodiscs at pH 6.5, 3024 micrographs were collected and the data processing procedure used was similar as above except that Relion 3.1 beta was used instead of Relion3.0 and refinement was performed without symmetry imposed. Bayesian particle polishing, CTF refinement, and particle subtraction yielded a final map at 3.5 Å.

3.3.6 Modeling and refinement

Cryo-EM maps were sharpened using Phenix.autosharpen [105] and LocalDeblur [106] and were of sufficient quality for de novo model building in Coot [71]. The real space refinement of the models was carried out using Phenix.real_space_refine with Ramachandran and NCS restraints [105] using LocalDeblur maps. Molprobity [73] was used to evaluate the stereochemistry and geometry of the structure for manual adjustment in Coot and refinement in Phenix. Cavity measurements were made with HOLE implemented in Coot. Figures were prepared using PyMOL, Chimera, and ChimeraX.

3.3.7 Electrophysiology

For electrophysiology, the same construct used for structural work was cloned into a modified pCEH vector for transient transfection. HEK293T cells grown in DMEM-F12 (Gibco) with 10% FBS, 2 mM L-glutamine, 100 units/mL penicillin and 100 µg/mL streptomycin were transfected with FugeneHD according to manufacturer's instructions. Cells were not authenticated or tested for mycoplasma contamination. Whole-cell recordings were performed at room temperature ~24-48 hours after transfection. Borosilicate glass pipettes were pulled to a resistance of 2-5 MΩ. An Axopatch 200B amplifier connected to a Digidata 1440B digitizer (Molecular Devices) was used for data acquisition with pClamp10. Analog signals were filtered at 1 kHz and sampled at 10 kHz. The following voltage protocol was applied once every 2.7 seconds: V_{hold}= -80 mV; V_{test}= -100 to +100 mV, Δ20 mV, 300 ms. Currents from each patch correspond to mean values during the voltage step to the indicated voltage averaged over three sequential families. We note cells displayed variable rundown in current magnitude over time. For pH titrations, comparisons between conditions were made when current rundown was complete. Fold changes were also assessed between recordings made sequentially in time to mitigate these effects.

For experiments testing the effect of intracellular pH changes on TASK2 current, pipette solution was 82 mM potassium gluconate, 50 mM potassium acetate, 8 mM KCl, 1 mM MgCl2, 10 mM HEPES, 10 mM BAPTA, pH 7.4 adjusted with Tris (at room temperature) and bath solution was sodium gluconate X, sodium acetate Y (where X +Y =135), 4 mM KCl, 2 mM CaCl2, 1 mM MgCl2, 20 mM HEPES, and titrated to pH 7.4 with 1 M Tris base. pH_{int} was changed by varying acetate concentrations according to[86]:

$$pH_{int} = pH_{ext} - log\frac{[acetate^{-}]_{ext}}{[acetate^{-}]_{int}}$$

The extracellular concentration of acetate was varied from 125.59, 39.71, 12.56, 3.97 and 1.26 mM to achieve intracellular pH values 7.0, 7.5, 8.0, 8.5 and 9.0.

For experiments testing the effect of extracellular pH changes on TASK2 current, pipette solution was 8 mM KCl, 132 mM potassium gluconate, 1 mM MgCl2, 10 mM EGTA, 10 mM HEPES, 1 mM Na3ATP, 0.1 mM GTP, pH 7.4 adjusted with 1M KOH and bath solution was 67.5 mM Na2SO4, 4 mM KCl, 1 mM potassium gluconate, 2 mM CaCl2, 1 mM MgCl2, 105 mM sucrose, 10 mM HEPES/Tris, pH 7.5. In order to measure the extracellular pH dependence of the currents, HEPES, was used for pH 7.0, 7.5, and 8.0 and Tris base was used for pH 8.5 and 9.0 (values at room temperature); all experiments keep both intracellular and extracellular chloride at 10 mM.

For experiments testing the effect of PIP_2, pipette solution contained 150 mM KCl, 10 mM HEPES, 3 mM $MgCl_2$, 5 mM EGTA, adjusted to pH 7.2 with 1M KOH, and the bath solution contained 15 mM KCl, 135 mM NaCl, 10 mM HEPES, 3 mM $MgCl_2$, 1 mM $CaCl_2$, adjusted to pH 7.3 with 1M NaOH. To test for PIP_2 activation, inside out excised patches were perfused with bath solution containing 50 µM diC8 PIP_2 (Avanti Polar Lipids, 850185). diC8 PIP_2-containing solution was made fresh before each experiment from 1 mM frozen aliquots dissolved in H_2O.

3.4 Tables

3.4.1 – Table 1 Cryo-EM data collection, refinement and validation statistics

	TASK2 pH 6.5 EMDB 21843 PDB 6WLV EMPIAR 10423	**TASK2 pH 8.5** EMDB 21846 PDB 6WM0 EMPIAR 10422
Data collection and processing		
Magnification	36,000	36,000
Voltage (kV)	200	200
Electron exposure (e–/Å^2)	50.325	50.4625
Defocus range (μm)	-0.8 to -2.0	-0.8 to -2.0
Pixel size (Å)	1.137	1.137
Symmetry imposed		
Initial particle images (no.)	3,563,337	3,806,879
Final particle images (no.)	255,808	78,594
Map resolution (Å)	3.5	3.5
FSC threshold	0.143	0.143
Refinement		
Model resolution (Å)	3.2	3.5
FSC threshold	0.143	0.143
Map sharpening *B* factor (Å^2)	-151.61	-86.73
Model composition		
Non-hydrogen atoms	4111	4105
Protein residues	512	510
Ligands	3	5
B factors (Å^2)		
Protein	73.91	55.33
Ligand	36.25	22.18
R.m.s. deviations		
Bond lengths (Å)	0.004	0.003
Bond angles (°)	0.549	0.577
Validation		
MolProbity score	1.82	1.48
Clashscore	9.21	6.67
Poor rotamers (%)	0	0
Ramachandran plot		
Favored (%)	95.28	97.43
Allowed (%)	4.72	2.57
Disallowed (%)	0	0

3.5 Data availability

TASK2 protein sequence is available from Uniprot accession Q9JK62. The final maps of TASK2 in MSP1D1 nanodiscs at pH 8.5 and 6.5 have been deposited to the Electron Microscopy Data Bank under accession codes 21846 and 21843. Atomic coordinates have been deposited in the PDB under IDs 6WM0 and 6WLV. Original micrograph movies have been deposited to EMPIAR under accession codes EMPIAR-10422 and EMPIAR-10423.

3.6 Author contributions

BL, RAR, and SGB conceived of the project. RAR generated and screened constructs. RAR optimized protein expression and purification. BL performed protein purification and nanodisc reconstitution for cryo-EM. BL prepared samples for cryo-EM, collected cryo-EM data, and processed cryo-EM data. BL built and refined atomic models. BL, RAR, and SGB performed electrophysiology. BL, RAR, and SGB wrote the manuscript. SGB supervised the project and secured funding.

3.7 Acknowledgements

We thank Dr. Jonathan Remis, Dr. Dan Toso, and Paul Tobias at UC Berkeley for assistance with microscope setup and data collection, Dr. Zhu Fu and Nora Kostow for help with initial cloning and screening, and members of the Brohawn lab for feedback on the manuscript. SGB is a New York Stem Cell Foundation-Robertson Neuroscience Investigator. This work was supported by the New York Stem Cell Foundation, NIGMS grant DP2GM123496, a McKnight Foundation Scholar Award, a Klingenstein-Simons Foundation Fellowship Award, and a Sloan Research Fellowship to SGB.

Chapter 4 Concluding Remarks

4.1 A diversity of gates and sensors

Ion channels in the K2P family possess an unmatched diversity of physical and chemical sensors. Biophysical investigations of sensors and their respective gates have benefitted from continued innovations in membrane protein crystallography and detergent chemistry [22,42], and reconstitution into native-like lipid environments and visualization by cryo-EM, as presented in chapter 3 [25]. Nearly every new structure reveals a new sensor and gate, and engenders new models of K2P channel gating [22,23,25,42,53].

4.1.1 Gating at the potassium selectivity filter

Gating at the selectivity filter was previously observed in TREK1 channel structures (Fig 2). Crystal structures of TREK1 in 100 and 200 mM concentrations of potassium show potassium ions occupying the canonical S1, S2, S3, and S4 sites created by the selectivity filter motif. However, the S1 and S2 positions are empty in structures of TREK1 in 0, 1, 10, 30 and 50 mM concentrations of potassium. In fact, the electron density corresponding to the fourth and fifth residues of the second selectivity filter motif and subsequent extracellular loop is not resolved despite comparable overall resolution to the structures solved in 100 and 200 mM potassium. This suggests the second selectivity filter motif and the loop connecting to the fourth transmembrane helix are conformationally flexible at low potassium concentrations. It is not clear if this potassium sensitivity in TREK1 is physiologically relevant, but it is possible that this selectivity filter gate is also be coupled to an extracellular pH sensing histidine that precedes the first pore helix [53,107]. We showed that the extracellular pH sensor of TASK2 is also coupled to selectivity filter to create a gate. In acidic extracellular conditions, protonation of a lysine residue on transmembrane helix four triggers a conformational relay that slackens the loop connecting transmembrane helix 4 (TM4) and the second selectivity filter motif. The S1 position of the selectivity is empty in acidic conditions, despite a 150 mM concentration of potassium ions. Similar to TREK1 in < 50 mM potassium, additional flexibility of the TASK2 selectivity filter motif and subsequent loop gates the channel closed by disrupting the S1 ion binding site [25]. Both of these studies show structural evidence of gating by conformational changes in the selectivity filter, or C-type gating, in K2P family ion channels.

4.1.2 Gating at the intracellular mouth

The intracellular mouth of the cavity can be sealed by the fourth and final transmembrane helix (TM4) (Fig 2). The crystal structure of TASK1 is assigned a nonconductive state because each TM4 bends inward to lie across the mouth of the cavity and block ions from traversing the channel [22]. The intracellular pH gate in TASK2 channels also gate at the intracellular mouth of the cavity. Protonation of a lysine side chain on TM4 stabilizes a conformation that pinches together at the mouth of the cavity and blocks the passage of ions. When this lysine is deprotonated by alkaline pH, it is stabilized in a conformation that rotates the side chain 90 degrees towards the cavity walls, expanding the constriction at the cavity mouth to permit the flow of ions. The gate at the intracellular mouth of TASK1 and TASK2 channels is conceptually similar to the canonical 'bundle crossing' in tetrameric potassium channels, but it is structurally distinct due the dimeric architecture of K2P family channels [108].

4.1.3 Gating at the intracellular cavity

Lipid or detergent acyl chains are observed to occupy the intracellular cavity below the selectivity filter in crystal structures of the mechanosensitive K2P family TREK2 and TRAAK channels (Fig 2) [12,42]. TREK2 and TRAAK channel structures have each been determined in two conformations that show the same conformational change. In one conformation the fourth and final transmembrane helix (TM4) is in a down conformational that exposes a lateral opening through which an acyl chain accesses the cavity (Fig 3). This acyl chain obstructs the conduction axis, effectively gating the channel closed. If this lipid were absent, the TM4 down conformation would also be conductive. TM4 moves upward to adopt the second conformation, which appears to be conductive because upward movement of TM4 seals the lateral opening. Instead of a lipid, electron density corresponding to a potassium ion is observed in the cavity of TREK2 and TRAAK structures in the TM4 up conformation.

4.1.4 Sensors assigned to gates

How are the gates coupled to the stimuli sensors in K2P family ion channels? In many cases, coupling between the gate and the sensor can be interpreted from channel structures. The TREK1 selectivity filter gates closed at low potassium concentration, and this conformational change may also explain its inhibition by acidic extracellular pH [107]. We show the extracellular pH sensor of TASK2 is part of a conformational relay that connects it to the selectivity filter [25]. Linking extracellular sensors to the selectivity filter makes some intuitive sense because it is the only known extracellular-facing gate.

Structures of TREK2 and TRAAK engender the hypothesis that TM4 movement is the physical basis for the mechanosensitivity of these two channels[12,42,43]. The cross sectional area of the channel in a TM4 up conformation is greater than the TM4 down conformation. In a membrane experiencing tension, the conformation that occupies a larger area in the membrane is favored[49,50]. The TM4 up conformation also appears to induce less membrane curvature, which is also energetically favorable in stretched membranes

In TASK2 channels, we show the conformational change of an intracellular pH sensing lysine positioned on TM4 near the intracellular mouth of the cavity gates the channel closed [25]. Some gating features observed in structures have not been connected to sensor, like the closed X-gate observed at the intracellular mouth of TASK1 channels.

4.1.5 Sensors with unknown gates

Many sensors identified by electrophysiology and mutagenesis do not have mechanistic gating models. Gates have not been assigned to: a pH sensing histidine in the extracellular loop between the cap and first pore helix in mechanosensitive channels [107], a conserved pH sensing histidine directly adjacent to the first selectivity filter motif in TASK1 and TASK3 channels [109], TRESK sensitivity to intracellular calcium via phosphorylation by Calmodulin and Calcineurin [110,111], temperature sensitivity in mechanosensitive K2P channels [38], and sensitivity to distinct lipids and fatty acids in several K2P subfamilies [2,26,33,88,112,113].

4.2 Common physiological modes of K2P channel gating

While the sensors and gates of each K2P member appear quite unique, the modes of channel gating are more stereotyped. Single channel recordings of K2P channels in native and recombinantly expressing cells exhibit two modes of activity: short flickery openings and longer bursts of activity [30-41]. The short flickery openings are observed when the channels are absent their respective stimuli. Under basal conditions, the channels maintain low open probabilities under these basal conditions ($P_o < 0.01$) [1,2]. The longer bursts of activity are rarely spontaneous, and are evoked by stimulation. We describe each respective activity as basal "leak type" and "stimulus gated." In TRAAK channels, we observe that the structural basis of the "stimulus gated" activity is the mechanically activated TM4 up conformation. The TM4 down conformation is stabilized at low, basal, membrane tension and the channel is gated closed by a lipid acyl chain that enters the cavity through exposed lateral opening. This lipid gated closed state can persist for tens of milliseconds between flickery "leak type" openings. The "leak type" activity occurs when a lipid acyl chain spontaneously exits the lateral opening. Does the "leak type" activity observed in other K2P family channels have the same structural basis?

4.3 Lateral gates in other K2P channels suggest a common gating mechanism in a diverse ion channel family

Some evidence suggests that the physical basis for distinct modes of TRAAK activity shown here could be shared among K2P channels. Differences between basal and stimulus-activated openings, including their kinetics and voltage dependence [94], have been reported for other K2Ps, suggesting that physically distinct open states could similarly underlie different modes of channel activity [30,38,41,44,52]. Mutations analogous to $\text{TRAAK}_{\text{G158D}}$ were found to activate all K2P channels, with the extent of activation correlated with the polarity of the introduced amino acid change [62]. Membrane-facing openings have been observed in TM4-down-like structures of TREK2 [12], TWIK1 [23], TASK1 [22], and TASK2 [25] in addition to TRAAK[24] (Fig. 32). Acyl chains that could block conduction were modeled in TWIK1 and TRAAK structures [23,24]. Tubular electron density that could be modeled as an acyl chain is observed in all closed state K2P structures to date (Fig. 33). This raises the possibility that lipid-mediated block could be more common among K2Ps than currently appreciated. Our lipid dependent model of basal "leak gated" openings in TRAAK channels may be generalizable to other K2P family channels. Basal "leak-gated" activity of other K2Ps could result from transient obstruction of the conduction path via lipid acyl chains entering through lateral openings, whereas "stimulus gated" activity involves conformational changes that prevent lipid entry into the channel conduction path [12,22–25,42].

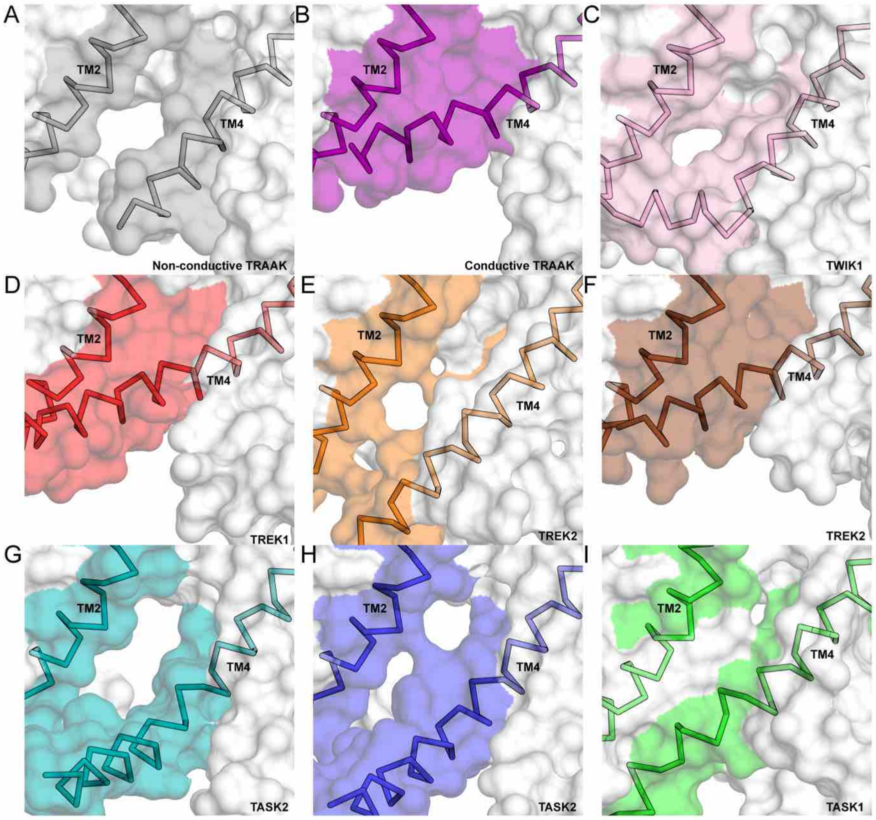

Figure 32 - Lateral openings in K2P family ion channels.
(A-I) View of the membrane-facing cytoplasmic half of TM4 from indicated K2P channels.

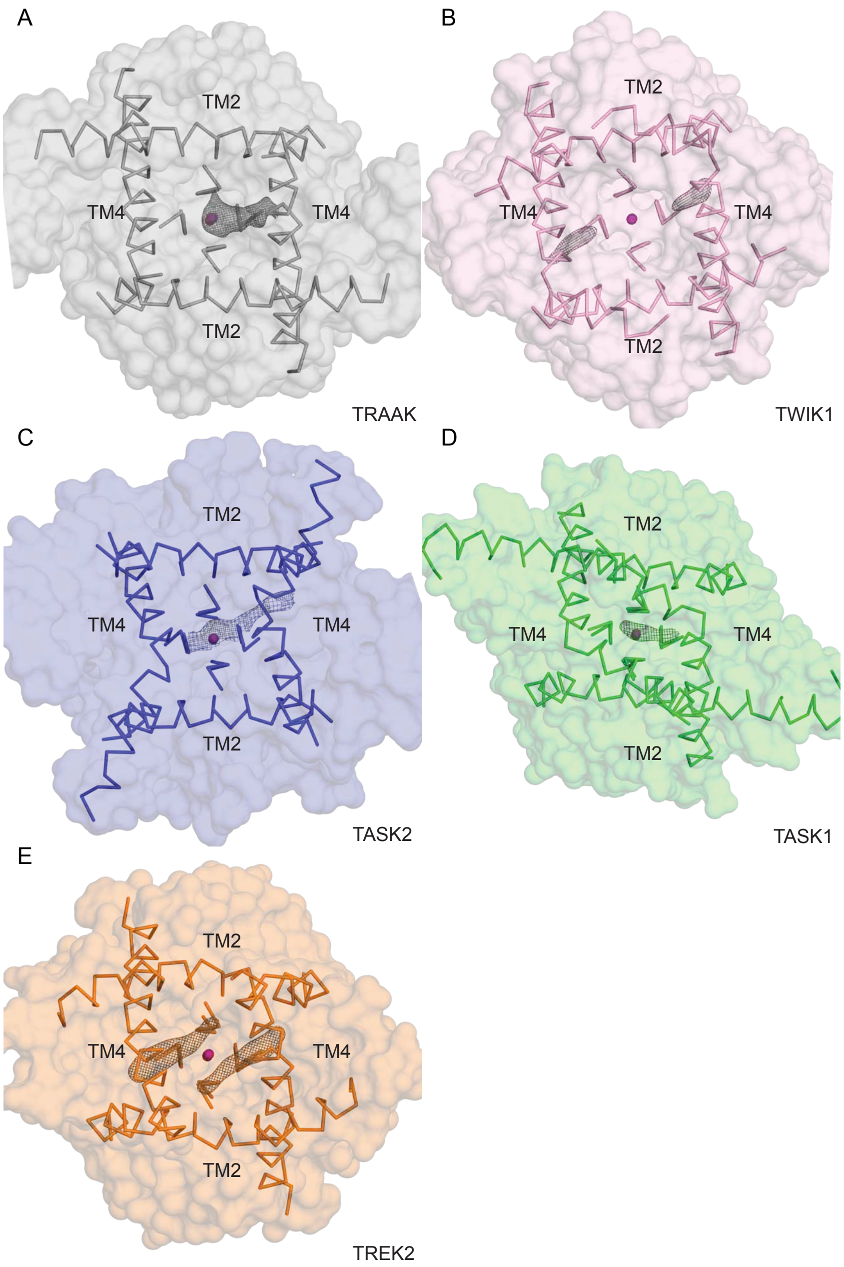

Figure 33 – Lipid-like densities in K2P structures with exposed lateral openings.
(A-E) View from the cytoplasmic side of the cavity the indicated K2P channel structures in the closed state. All density maps are contoured at 1 sigma, except for TASK2 which is contoured at 4 sigma.

References

1. Enyedi, P. & Czirják, G. Molecular background of leak K+ currents: two-pore domain potassium channels. *Physiol. Rev.* **90**, 559–605 (2010).
2. Renigunta, V., Schlichthörl, G. & Daut, J. Much more than a leak: Structure and function of K2P-channels. *Pflugers Arch. Eur. J. Physiol.* 867–894 (2015). doi:10.1007/s00424-015-1703-7
3. Chatelain, F. C. *et al.* TWIK1, a unique background channel with variable ion selectivity. *Proc. Natl. Acad. Sci. U. S. A.* (2012). doi:10.1073/pnas.1201132109
4. Brohawn, S. G. *et al.* The mechanosensitive ion channel traak is localized to the mammalian node of ranvier. *Elife* (2019). doi:10.7554/eLife.50403
5. Kanda, H. *et al.* TREK-1 and TRAAK Are Principal K+ Channels at the Nodes of Ranvier for Rapid Action Potential Conduction on Mammalian Myelinated Afferent Nerves. *Neuron* (2019). doi:10.1016/j.neuron.2019.08.042
6. Gestreau, C. *et al.* Task2 potassium channels set central respiratory CO2 and O 2 sensitivity. *Proc. Natl. Acad. Sci. U. S. A.* (2010). doi:10.1073/pnas.0910059107
7. Wang, S. *et al.* TASK-2 channels contribute to pH sensitivity of retrotrapezoid nucleus chemoreceptor neurons. *J. Neurosci.* (2013). doi:10.1523/JNEUROSCI.2451-13.2013
8. Guyenet, P. G. *et al.* The Retrotrapezoid Nucleus: Central Chemoreceptor and Regulator of Breathing Automaticity. *Trends in Neurosciences* (2019). doi:10.1016/j.tins.2019.09.002
9. Warth, R. *et al.* Proximal renal tubular acidosis in TASK2 K+ channel-deficient mice reveals a mechanism for stabilizing bicarbonate transport. *Proc. Natl. Acad. Sci. U. S. A.* (2004). doi:10.1073/pnas.0400081101
10. Lafrenière, R. G. *et al.* A dominant-negative mutation in the TRESK potassium channel is linked to familial migraine with aura. *Nat. Med.* (2010). doi:10.1038/nm.2216
11. Honoré, E. The neuronal background K2P channels: focus on TREK1. *Nat. Rev. Neurosci.* **8**, 251–261 (2007).
12. Dong, Y. Y. *et al.* K2P channel gating mechanisms revealed by structures of TREK-2 and a complex with Prozac. *Science (80-.).* **347**, 1256–9 (2015).
13. Ma, L. *et al.* A novel channelopathy in pulmonary arterial hypertension. *N. Engl. J. Med.* (2013). doi:10.1056/NEJMoa1211097
14. Schmidt, C. *et al.* Upregulation of K2P 3.1 K + Current Causes Action Potential Shortening in Patients with Chronic Atrial Fibrillation. *Circulation* (2015). doi:10.1161/CIRCULATIONAHA.114.012657
15. Vierra, N. C. *et al.* Type 2 diabetes-associated K+ channel TALK-1 modulates β-cell electrical excitability, second-phase insulin secretion, and glucose homeostasis. *Diabetes* (2015). doi:10.2337/db15-0280
16. Barel, O. *et al.* Maternally Inherited Birk Barel Mental Retardation Dysmorphism Syndrome Caused by a Mutation in the Genomically Imprinted Potassium Channel KCNK9. *Am. J. Hum. Genet.* (2008). doi:10.1016/j.ajhg.2008.07.010
17. Veale, E. L., Hassan, M., Walsh, Y., Al-Moubarak, E. & Mathie, A. Recovery of

current through mutated TASK3 potassium channels underlying birk barel syndrome. *Mol. Pharmacol.* (2014). doi:10.1124/mol.113.090530

18. Bauer, C. K. *et al.* Mutations in KCNK4 that Affect Gating Cause a Recognizable Neurodevelopmental Syndrome. *Am. J. Hum. Genet.* (2018). doi:10.1016/j.ajhg.2018.09.001
19. Gada, K. & Plant, L. D. Two-pore domain potassium channels: emerging targets for novel analgesic drugs: IUPHAR Review 26. *British Journal of Pharmacology* (2019). doi:10.1111/bph.14518
20. Lolicato, M. *et al.* K2P2.1 (TREK-1)-activator complexes reveal a cryptic selectivity filter binding site. *Nature* (2017). doi:10.1038/nature22988
21. Schewe, M. *et al.* A pharmacological master key mechanism that unlocks the selectivity filter gate in K channels. *Science (80-.).* (2019). doi:10.1126/science.aav0569
22. Rödström, K. E. J. *et al.* A lower X-gate in TASK channels traps inhibitors within the vestibule. *Nature* (2020). doi:10.1038/s41586-020-2250-8
23. Miller, A. N. & Long, S. B. Crystal structure of the human two-pore domain potassium channel K2P1. *Science* **335**, 432–6 (2012).
24. Brohawn, S. G., del Marmol, J. & MacKinnon, R. Crystal Structure of the Human K2P TRAAK, a Lipid- and Mechano-Sensitive K+ Ion Channel. *Science (80-.).* **335**, 436–441 (2012).
25. Li, B., Rietmeijer, R. A. & Brohawn, S. G. Structural basis for pH gating of the two-pore domain K+ channel TASK2. *Nature* (2020). doi:10.1038/s41586-020-2770-2
26. Fink, M. *et al.* A neuronal two P domain K+ channel stimulated by arachidonic acid and polyunsaturated fatty acids. *EMBO J.* **17**, 3297–3308 (1998).
27. Lesage, F. *et al.* TWIK-1, a ubiquitous human weakly inward rectifying K+ channel with a novel structure. *EMBO J.* **15**, 1004–11 (1996).
28. Niemeyer, M. I., Cid, L. P., González, W. & Sepúlveda, F. V. Gating, Regulation, and structure in K2P K+ Channels: In varietate concordia? *Molecular Pharmacology* (2016). doi:10.1124/mol.116.103895
29. Pope, L., Lolicato, M. & Minor, D. L. Polynuclear Ruthenium Amines Inhibit K2P Channels via a “Finger in the Dam” Mechanism. *Cell Chem. Biol.* (2020). doi:10.1016/j.chembiol.2020.01.011
30. Maingret, F., Fosset, M., Lesage, F., Lazdunski, M. & Honoré, E. TRAAK is a mammalian neuronal mechano-gated K+ channel. *J. Biol. Chem.* **274**, 1381–1387 (1999).
31. Kim, Y., Bang, H., Gnatenco, C. & Kim, D. Synergistic interaction and the role of C-terminus in the activation of TRAAK K+ channels by pressure, free fatty acids and alkali. *Pflugers Arch. Eur. J. Physiol.* **442**, 64–72 (2001).
32. Rajan, S., Plant, L. D., Rabin, M. L., Butler, M. H. & Goldstein, S. A. N. Sumoylation silences the plasma membrane leak K+ channel K2P1. *Cell* (2005). doi:10.1016/j.cell.2005.01.019
33. Kim, D. Fatty acid-sensitive two-pore domain K+ channels. *Trends in Pharmacological Sciences* (2003). doi:10.1016/j.tips.2003.10.008
34. Leonoudakis, D. *et al.* An open rectifier potassium channel with two pore domains in tandem cloned from rat cerebellum. *J. Neurosci.* (1998).

doi:10.1523/JNEUROSCI.18-03-00868.1998

35. Kang, D., Hogan, J. O. & Kim, D. THIK-1 (K2P13.1) is a small-conductance background K+ channel in rat trigeminal ganglion neurons. *Pflugers Arch. Eur. J. Physiol.* (2014). doi:10.1007/s00424-013-1358-1
36. Kang, D. & Kim, D. Single-channel properties and pH sensitivity of two-pore domain K + channels of the TALK family. *Biochem. Biophys. Res. Commun.* (2004). doi:10.1016/j.bbrc.2004.01.137
37. Kang, D., Mariash, E. & Kim, D. Functional expression of TRESK-2, a new member of the tandem-pore K + channel family. *J. Biol. Chem.* (2004). doi:10.1074/jbc.M402940200
38. Kang, D., Choe, C. & Kim, D. Thermosensitivity of the two-pore domain K + channels TREK-2 and TRAAK. *J Physiol* **5641**, 103–116 (2005).
39. Kim, D. & Clapham, D. E. Potassium channels in cardiac cells activated by arachidonic acid and phospholipids. *Science (80-.).* (1989). doi:10.1126/science.2727703
40. Kim, D. A mechanosensitive K+ channel in heart cells: Activation by arachidonic acid. *J. Gen. Physiol.* (1992). doi:10.1085/jgp.100.6.1021
41. Gnatenco, C., Han, J., Snyder, A. K. & Kim, D. Functional expression of TREK-2 K+ channel in cultured rat brain astrocytes. *Brain Res.* (2002). doi:10.1016/S0006-8993(02)02261-8
42. Brohawn, S. G., Campbell, E. B. & MacKinnon, R. Physical mechanism for gating and mechanosensitivity of the human TRAAK K+ channel. *Nature* **516**, 126–130 (2014).
43. Brohawn, S. G., Su, Z. & MacKinnon, R. Mechanosensitivity is mediated directly by the lipid membrane in TRAAK and TREK1 K+ channels. *Proc. Natl. Acad. Sci. U. S. A.* **111**, 3614–3619 (2014).
44. Sorum, B., Rietmeijer, R. A., Gopakumar, K., Adesnik, H. & Brohawn, S. G. Ultrasound activates mechanosensitive TRAAK K+ channels directly through the lipid membrane. *bioRxiv* (2020).
45. Rasband, M. N. & Shrager, P. Ion channel sequestration in central nervous system axons. *Journal of Physiology* (2000). doi:10.1111/j.1469-7793.2000.00063.x
46. Rasband, M. N. & Peles, E. The nodes of Ranvier: Molecular assembly and maintenance. *Cold Spring Harb. Perspect. Biol.* (2016). doi:10.1101/cshperspect.a020495
47. Waxman, S. G., Kocsis, J. D. & Stys, P. K. *The Axon: Structure, Function and Pathophysiology*. *The Axon: Structure, Function and Pathophysiology* (2009). doi:10.1093/acprof:oso/9780195082937.001.0001
48. Noël, J. *et al.* The mechano-activated K± channels TRAAK and TREK-1 control both warm and cold perception. *EMBO J.* (2009). doi:10.1038/emboj.2009.57
49. Ursell, T., Phillips, R., Kondev, J., Reeves, D. & Wiggins, P. a. The Role of Lipid Bilayer Mechanics in Mechanosensation. *Mechanosensitive Ion Channels* **1**, 37–80 (2008).
50. Wiggins, P. & Phillips, R. Membrane-protein interactions in mechanosensitive channels. *Biophys. J.* **88**, 880–902 (2005).
51. Xian Tao Li *et al.* The stretch-activated potassium channel TREK-1 in rat

cardiac ventricular muscle. *Cardiovasc. Res.* (2006). doi:10.1016/j.cardiores.2005.08.018

52. Bang, H., Kim, Y. & Kim, D. TREK-2, a new member of the mechanosensitive tandem-pore K+ channel family. *J. Biol. Chem.* (2000). doi:10.1074/jbc.M000445200
53. Lolicato, M. *et al.* K2P channel C-type gating involves asymmetric selectivity filter order-disorder transitions. *Sci. Adv.* (2020). doi:10.1126/sciadv.abc9174
54. Aryal, P., Abd-Wahab, F., Bucci, G., Sansom, M. S. P. & Tucker, S. J. A hydrophobic barrier deep within the inner pore of the TWIK-1 K2P potassium channel. *Nat. Commun.* (2014). doi:10.1038/ncomms5377
55. Aryal, P., Sansom, M. S. P. & Tucker, S. J. Hydrophobic gating in ion channels. *Journal of Molecular Biology* (2015). doi:10.1016/j.jmb.2014.07.030
56. Lolicato, M., Riegelhaupt, P. M., Arrigoni, C., Clark, K. A. & Minor, D. L. Transmembrane helix straightening and buckling underlies activation of mechanosensitive and thermosensitive K2P channels. *Neuron* **84**, 1198–1212 (2014).
57. Honoré, E., Patel, A. J., Chemin, J., Suchyna, T. & Sachs, F. Desensitization of mechano-gated K2P channels. *Proc. Natl. Acad. Sci. U. S. A.* (2006). doi:10.1073/pnas.0600463103
58. Nomura, T. *et al.* Differential effects of lipids and lyso-lipids on the mechanosensitivity of the mechanosensitive channels MscL and MscS. *Proc. Natl. Acad. Sci. U. S. A.* **109**, 8770–5 (2012).
59. Lewis, A. H. & Grandl, J. Mechanical sensitivity of Piezo1 ion channels can be tuned by cellular membrane tension. *Elife* **4**, (2015).
60. Opsahl, L. R. & Webb, W. W. Lipid-glass adhesion in giga-sealed patch-clamped membranes. *Biophys J* **66**, 75–79 (1994).
61. Moe, P. & Blount, P. Assessment of potential stimuli for mechano-dependent gating of MscL: Effects of pressure, tension, and lipid headgroups. *Biochemistry* **44**, 12239–12244 (2005).
62. Ben Soussia, I. *et al.* Mutation of a single residue promotes gating of vertebrate and invertebrate two-pore domain potassium channels. *Nat. Commun.* (2019). doi:10.1038/s41467-019-08710-3
63. Brooks, B. R. and Brooks, III, C. L. and Mackerell, Jr., A. D. and *et al.* CHARMM: The Biomolecular Simulation Program. *J. Comput. Chem.* (2009).
64. Jo, S., Kim, T., Iyer, V. G. & Im, W. CHARMM-GUI: A web-based graphical user interface for CHARMM. *J. Comput. Chem.* (2008). doi:10.1002/jcc.20945
65. Sorum, B., Czégé, D. & Csanády, L. Timing of CFTR Pore Opening and Structure of Its Transition State. *Cell* (2015). doi:10.1016/j.cell.2015.09.052
66. Harden, S. Analysis of electrophysiological recordings was performed with custom software written for this project using Python 3.7 and the pyABF module. (2019).
67. Kabsch, W. *et al. XDS*. *Acta Crystallogr. Sect. D Biol. Crystallogr.* (2010). doi:10.1107/S0907444909047337
68. Kabsch, W. Integration, scaling, space-group assignment and post-refinement. *Acta Crystallogr. Sect. D Biol. Crystallogr.* (2010). doi:10.1107/S0907444909047374

69. Tickle, I. J. *et al.* STARANISO. *Cambridge, United Kingdom: Global Phasing Ltd.* (2018).
70. McCoy, A. J. *et al.* Phaser crystallographic software. *J. Appl. Crystallogr.* (2007). doi:10.1107/S0021889807021206
71. Emsley, P. & Cowtan, K. Coot: Model-building tools for molecular graphics. *Acta Crystallogr. Sect. D Biol. Crystallogr.* (2004). doi:10.1107/S0907444904019158
72. Murshudov, G. N. *et al.* REFMAC5 for the refinement of macromolecular crystal structures. *Acta Crystallogr. Sect. D Biol. Crystallogr.* (2011). doi:10.1107/S0907444911001314
73. Chen, V. B. *et al.* MolProbity: All-atom structure validation for macromolecular crystallography. *Acta Crystallogr. Sect. D Biol. Crystallogr.* (2010). doi:10.1107/S0907444909042073
74. Pettersen, E. F. *et al.* UCSF Chimera - A visualization system for exploratory research and analysis. *J. Comput. Chem.* (2004). doi:10.1002/jcc.20084
75. Jo, S., Kim, T. & Im, W. Automated builder and database of protein/membrane complexes for molecular dynamics simulations. *PLoS One* (2007). doi:10.1371/journal.pone.0000880
76. Klesse, G., Rao, S., Sansom, M. S. P. & Tucker, S. J. CHAP: A Versatile Tool for the Structural and Functional Annotation of Ion Channel Pores. *J. Mol. Biol.* (2019). doi:10.1016/j.jmb.2019.06.003
77. Reyes, R. *et al.* Cloning and expression of a novel pH-sensitive two pore domain K+ channel from human kidney. *J. Biol. Chem.* (1998). doi:10.1074/jbc.273.47.30863
78. Cid, L. P. *et al.* TASK-2: A K2P K+ channel with complex regulation and diverse physiological functions. *Frontiers in Physiology* (2013). doi:10.3389/fphys.2013.00198
79. Niemeyer, M. I., Cid, L. P., Barros, L. F. & Sepúlveda, F. V. Modulation of the Two-pore Domain Acid-sensitive K+ Channel TASK-2 (KCNK5) by Changes in Cell Volume. *J. Biol. Chem.* (2001). doi:10.1074/jbc.M107192200
80. Bayliss, D. A., Barhanin, J., Gestreau, C. & Guyenet, P. G. The role of pH-sensitive TASK channels in central respiratory chemoreception. *Pflugers Archiv European Journal of Physiology* (2015). doi:10.1007/s00424-014-1633-9
81. Julio-Kalajzić, F. *et al.* K 2P TASK-2 and KCNQ1–KCNE3 K + channels are major players contributing to intestinal anion and fluid secretion. *J. Physiol.* (2018). doi:10.1113/JP275178
82. Clark, R. B., Kondo, C., Belke, D. D. & Giles, W. R. Two-pore domain K + channels regulate membrane potential of isolated human articular chondrocytes. *J. Physiol.* (2011). doi:10.1113/jphysiol.2011.210757
83. Alvarez-Baron, C. P., Jonsson, P., Thomas, C., Dryer, S. E. & Williams, C. The two-pore domain potassium channel KCNK5: Induction by estrogen receptor α and role in proliferation of breast cancer cells. *Mol. Endocrinol.* (2011). doi:10.1210/me.2011-0045
84. Reed, A. P., Bucci, G., Abd-Wahab, F. & Tucker, S. J. Dominant-negative effect of a missense variant in the TASK-2 (KCNK5) K+ channel associated with Balkan

Endemic Nephropathy. *PLoS One* (2016). doi:10.1371/journal.pone.0156456

85. López-Cayuqueo, K. I., Peña-Münzenmayer, G., Niemeyer, M. I., Sepúlveda, F. V. & Cid, L. P. TASK-2 K2P K+ channel: Thoughts about gating and its fitness to physiological function. *Pflugers Archiv European Journal of Physiology* (2015). doi:10.1007/s00424-014-1627-7
86. Niemeyer, M. I., Cid, L. P., Peña-Münzenmayer, G. & Sepúlveda, F. V. Separate gating mechanisms mediate the regulation of K2P potassium channel TASK-2 by intra- and extracellular pH. *J. Biol. Chem.* (2010). doi:10.1074/jbc.M110.107060
87. Niemeyer, M. I. *et al.* Neutralization of a single arginine residue gates open a two-pore domain, alkali-activated K+ channel. *Proc. Natl. Acad. Sci. U. S. A.* (2007). doi:10.1073/pnas.0606173104
88. Niemeyer, M. I., Cid, L. P., Paulais, M., Teulon, J. & Sepúlveda, F. V. Phosphatidylinositol (4,5)-bisphosphate dynamically regulates the K2P background K+ channel TASK-2. *Sci. Rep.* (2017). doi:10.1038/srep45407
89. Ritchie, T. K. *et al.* Chapter 11 Reconstitution of Membrane Proteins in Phospholipid Bilayer Nanodiscs. *Methods in Enzymology* (2009). doi:10.1016/S0076-6879(09)64011-8
90. Isom, D. G., Castañed, C. A., Cannon, B. R. & García-Moreno, B. E. Large shifts in pKa values of lysine residues buried inside a protein. *Proc. Natl. Acad. Sci. U. S. A.* (2011). doi:10.1073/pnas.1010750108
91. Del Camino, D. & Yellen, G. Tight steric closure at the intracellular activation gate of a voltage-gated K+ channel. *Neuron* (2001). doi:10.1016/S0896-6273(01)00487-1
92. Jiang, Y. *et al.* The open pore conformation of potassium channels. *Nature* (2002). doi:10.1038/417523a
93. Piechotta, P. L. *et al.* The pore structure and gating mechanism of K2P channels. *EMBO J.* (2011). doi:10.1038/emboj.2011.268
94. Schewe, M. *et al.* A Non-canonical Voltage-Sensing Mechanism Controls Gating in K2P K+ Channels. *Cell* **164**, 937–949 (2016).
95. Bagriantsev, S. N., Peyronnet, R., Clark, K. A., Honoré, E. & Minor, D. L. Multiple modalities converge on a common gate to control K2P channel function. *EMBO J.* (2011). doi:10.1038/emboj.2011.230
96. Hoshi, T., Zagotta, W. N. & Aldrich, R. W. Two types of inactivation in Shaker K+ channels: Effects of alterations in the carboxy-terminal region. *Neuron* (1991). doi:10.1016/0896-6273(91)90367-9
97. Cohen, A., Ben-Abu, Y., Hen, S. & Zilberberg, N. A novel mechanism for human K2P2.1 channel gating: Facilitation of C-type gating by protonation of extracellular histidine residues. *J. Biol. Chem.* (2008). doi:10.1074/jbc.M801273200
98. Cuello, L. G., Cortes, D. M. & Perozo, E. The gating cycle of a K+ channel at atomic resolution. *Elife* (2017). doi:10.7554/eLife.28032
99. Pau, V., Zhou, Y., Ramu, Y., Xu, Y. & Lu, Z. Crystal structure of an inactivated mutant mammalian voltage-gated K+ channel. *Nat. Struct. Mol. Biol.* (2017). doi:10.1038/nsmb.3457
100. Brohawn, S. G. How ion channels sense mechanical force: Insights from

mechanosensitive K2P channels TRAAK, TREK1, and TREK2. *Ann. N. Y. Acad. Sci.* (2015). doi:10.1111/nyas.12874

101. Mastronarde, D. N. Automated electron microscope tomography using robust prediction of specimen movements. *J. Struct. Biol.* (2005). doi:10.1016/j.jsb.2005.07.007
102. Zivanov, J., Nakane, T. & Scheres, S. H. W. A Bayesian approach to beam-induced motion correction in cryo-EM single-particle analysis. *IUCrJ* (2019). doi:10.1107/S205225251801463X
103. Zheng, S. Q. *et al.* MotionCor2: Anisotropic correction of beam-induced motion for improved cryo-electron microscopy. *Nature Methods* (2017). doi:10.1038/nmeth.4193
104. Zivanov, J. *et al.* New tools for automated high-resolution cryo-EM structure determination in RELION-3. *Elife* (2018). doi:10.7554/eLife.42166
105. Afonine, P. V. *et al.* Real-space refinement in PHENIX for cryo-EM and crystallography. *Acta Crystallogr. Sect. D Struct. Biol.* (2018). doi:10.1107/S2059798318006551
106. Ramírez-Aportela, E. *et al.* Automatic local resolution-based sharpening of cryo-EM maps. *Bioinformatics* (2020). doi:10.1093/bioinformatics/btz671
107. Sandoz, G., Douguet, D., Chatelain, F., Lazdunski, M. & Lesage, F. Extracellular acidification exerts opposite actions on TREK1 and TREK2 potassium channels via a single conserved histidine residue. *Proc. Natl. Acad. Sci. U. S. A.* (2009). doi:10.1073/pnas.0906267106
108. Doyle, D. A. *et al.* The structure of the potassium channel: Molecular basis of K^+ conduction and selectivity. *Science (80-.).* **280**, 69–77 (1998).
109. Morton, M. J., O'Connell, A. D., Sivaprasadarao, A. & Hunter, M. Determinants of pH sensing in the two-pore domain K+ channels TASK-1 and -2. *Pflugers Arch. Eur. J. Physiol.* (2003). doi:10.1007/s00424-002-0901-2
110. Czirják, G., Tóth, Z. E. & Enyedi, P. The Two-pore Domain K+ Channel, TRESK, Is Activated by the Cytoplasmic Calcium Signal through Calcineurin. *J. Biol. Chem.* (2004). doi:10.1074/jbc.M312229200
111. Enyedi, P. & Czirják, G. Properties, regulation, pharmacology, and functions of the K2P channel, TRESK. *Pflugers Arch. Eur. J. Physiol.* 945–958 (2014). doi:10.1007/s00424-014-1634-8
112. Lopes, C. M. B. *et al.* PIP2 hydrolysis underlies agonist-induced inhibition and regulates voltage gating of two-pore domain K+ channels. *J. Physiol.* (2005). doi:10.1113/jphysiol.2004.081935
113. Chemin, J. *et al.* Lysophosphatidic acid-operated K+ channels. *J. Biol. Chem.* (2005). doi:10.1074/jbc.M408246200